

A COMBINED EXPERIMENTAL AND ANALYTICAL APPROACH FOR
INTERFACE FRACTURE PARAMETERS BETWEEN
DISSIMILAR MATERIALS IN ELECTRONIC PACKAGES

by

Norman R. Kay

Copyright © Norman R. Kay 2003

A Dissertation Submitted to the Faculty of the
AEROSPACE AND MECHANICAL ENGINEERING DEPARTMENT

In Partial Fulfillment of the Requirements
For the Degree of

DOCTOR OF PHILOSOPHY
WITH A MAJOR IN MECHANICAL ENGINEERING

In the Graduate College

THE UNIVERSITY OF ARIZONA

2003

UMI Number: 3089957

Copyright 2003 by
Kay, Norman R.

All rights reserved.

UMI[®]

UMI Microform 3089957

Copyright 2003 by ProQuest Information and Learning Company.
All rights reserved. This microform edition is protected against
unauthorized copying under Title 17, United States Code.

ProQuest Information and Learning Company
300 North Zeeb Road
P.O. Box 1346
Ann Arbor, MI 48106-1346

THE UNIVERSITY OF ARIZONA®
GRADUATE COLLEGE

- 2 -

As members of the Final Examination Committee, we certify that we have read the dissertation prepared by Norman R. Kay entitled A Combined Experimental and Analytical Approach for Interface Fracture Parameters between Dissimilar Materials in Electronic Packages and recommend that it be accepted as fulfilling the dissertation requirement for the Degree of Doctor Of Philosophy

Erdogan Madenci
Erdogan Madenci

4-16-03
Date

Eniko Enikov
Eniko Enikov

4-16-03
Date

Tribikram Kundu
Tribikram Kundu

4-16-03
Date

Final approval and acceptance of this dissertation is contingent upon the candidate's submission of the final copy of the dissertation to the Graduate College.

I hereby certify that I have read this dissertation prepared under my direction and recommend that it be accepted as fulfilling the dissertation requirement.

Erdogan Madenci
Dissertation Director - Erdogan Madenci

4-16-03
Date

STATEMENT BY THE AUTHOR

This dissertation has been submitted in partial fulfillment of requirements for an advanced degree at The University of Arizona and is deposited in the University Library to be made available to borrowers under rules of the Library.

Brief quotations from this dissertation are allowable without special permission, provided that accurate acknowledgement of source is made. Requests for permission for extended quotation from or reproduction of this manuscript in whole or in part may be granted by the copyright holder.

SIGNED:

A handwritten signature in black ink, appearing to be 'M. K. O. S.', written over a horizontal line.

ACKNOWLEDGEMENTS

I wish to express my sincere thanks to Dr. Erdogan Madenci for all the help and support he has given me during my studies at the university. I also want to thank my pseudo-advisors Dr. Atila Barut, Dr. Ibrahim Guven, and (when he was here) Dr. Todd Anderson for all the times they helped me clarify items that weren't always relevant to my research, but especially for the times they helped me gain a deeper understanding of the topics I needed to know. I want to also thank Damian Athey and Santaneel Ghosh for the assistance they gave with my experimental work and John Hanauska for running to the library to get papers that I should have been copying myself.

Thanks are also in order for the Semiconductor Research Corporation (SRC) whose financial support paid for minor items secondary to my research – food, clothing, housing, et cetera – as well as their direct funding of items vital for my project's success.

Of course, none of this would be possible without the continued support of my wife, Renae. I'll be forever thankful that she had the patience to be a grad school widow more often than she should – but now that time is (thankfully) over.

For my wife, parents, and family – and my newborn son, Nathan.

TABLE OF CONTENTS

LIST OF FIGURES	7
LIST OF TABLES.....	11
ABSTRACT	12
1. INTRODUCTION	14
1.1. Experimental Background.....	15
1.2. Analytical Background.....	22
1.3. Summation and Roadmap	26
2. EXPERIMENTAL INVESTIGATION	28
2.1. Specimen Preparation.....	28
2.2. Testing Procedure	52
2.3. Summation.....	61
3. ANALYTICAL STRESS ANALYSIS.....	63
3.1. Problem Statement	64
3.2. Solution Method.....	66
3.3. Validation.....	84
3.4. Summation.....	91
4. EXTRACTION OF FRACTURE PARAMETERS.....	93
4.1. Experimental Measurements and Extraction of Fracture Parameters.....	93
4.2. Summary of Critical Stress Intensity Factors	112
4.3. Summary of Critical Energy Release Rates.....	113
4.4. Summation.....	116
5. CLOSING REMARKS.....	118
APPENDICES.....	122
Appendix A.....	123
Appendix B.....	126
REFERENCES	130

LIST OF FIGURES

Figure 2-1: *Post-production electronic package sample*28

Figure 2-2a: *Cross-section specimen of electronic package*29

Figure 2-2b: *Schematic of highlighted portion of Figure 2-2a*.....29

Figure 2-3: *Package covered with thermoformed Con-Tact paper prior to encapsulation*.....33

Figure 2-4: *Sample with stand-off clips in a disposable encapsulation cup*.....37

Figure 2-5a: *Custom-built encapsulation mold with faces plates closed*.....38

Figure 2-5b: *Encapsulation mold with face plates opened*.....38

Figure 2-6: *Modified sectioning saw fixture*39

Figure 2-7: *Package section before removal from support matrix*40

Figure 2-8: *Crack precursor scribed in the underfill fillet*43

Figure 2-9a: *Schematic of scribe method specimen crack introduction*45

Figure 2-9b: *Detail of crack propagation schematic from Figure 2-9a*45

Figure 2-10: *Bend fixture under optical microscope*46

Figure 2-11a: *Standard four-point bend specimen for interfacial strength determination*47

Figure 2-11b: *Schematic of notch method specimen*.....47

Figure 2-12: *SEM image of notch*.....48

Figure 2-13a: *Final specimen cross-section with BGA solder balls*.....49

Figure 2-13b: *Final specimen with BGA solder balls removed and fillets scribed*49

Figure 2-14: *TEM support grid used to create reference marks*51

Figure 2-15: *SEM image of underfill crack in a region marked with reference points*51

LIST OF FIGURES - CONTINUED

Figure 2-16a: *Custom SEM stage with bending fixture and thermal control*54

Figure 2-16b: *Stage with three-point bend fixture installed*55

Figure 2-16c: *Specimen marked with reference points in three-point bend fixture*.....55

Figure 2-17: *Displacement control and load readout for SEM loading stage*57

Figure 2-18: *Displacement determination using digital image correlation*59

Figure 2-19: *Sample reference image for digital image correlation*59

Figure 2-20: *Undeformed and deformed meshes from digital image correlation*60

Figure 2-21: *Vector field representation of displacements from digital image correlation (displacement vectors not to scale)*.....61

Figure 3-1: *Geometry of a finite domain of two dissimilar viscoelastic materials*63

Figure 3-2: *Boundary segments and their unit normals*65

Figure 3-3: *Collocation (integration) points along the boundary of the finite region*79

Figure 3-4: *Bonded dissimilar viscoelastic regions*.....85

Figure 3-5: *Strength of the singularity as the second material loses its relaxation*86

Figure 3-6: *Relaxation of peeling stress near the junction point along the interface for a combination of viscoelastic and elastic materials*87

Figure 3-7: *Relaxation of shear stress near the junction point along the interface for a combination of viscoelastic and elastic materials*87

Figure 3-8: *Variation of the peeling stress along the interface away from the junction point at various times for a combination of viscoelastic and elastic materials*.....88

Figure 3-9: *Variation of the shear stress along the interface away from the junction point at various times for a combination of viscoelastic and elastic materials*.....88

Figure 3-10: *An interface crack between two bonded dissimilar viscoelastic materials*...90

LIST OF FIGURES - CONTINUED

Figure 3-11: *Time dependence of the imaginary (oscillatory) part of the singularity for an interface crack between two viscoelastic materials*90

Figure 3-12: *Relaxation of the stress intensity factor for an interface crack between two viscoelastic materials*91

Figure 4-1: *An image pair from test number 1*.....95

Figure 4-2: *Correlation boundary, interface and crack tip locations from test number 1*95

Figure 4-3: *Interfacial stresses from analytical model for test number 1*.....96

Figure 4-4: *An image pair from test number 2*.....98

Figure 4-5: *Correlation boundary, interface and crack tip location from test number 2*98

Figure 4-6: *Interfacial stresses from analytical model for test number 2*.....99

Figure 4-7: *An image pair from test number 3*.....101

Figure 4-8: *Correlation boundary, interface and crack tip location from test number 3*102

Figure 4-9: *Interfacial stresses from analytical model for test number 3*.....103

Figure 4-10: *An image pair from test number 4*.....104

Figure 4-11: *Correlation boundary, interface and crack tip location from test number 4*105

Figure 4-12: *Interfacial stresses from analytical model for test number 4*.....106

Figure 4-13: *An image pair from test number 5*.....107

Figure 4-14: *Correlation boundary, interface and crack tip location from test number 5*107

Figure 4-15: *Interfacial stresses from analytical model for test number 5*.....108

LIST OF FIGURES - CONTINUED

Figure 4-16: *An image pair from test number 6*.....110

Figure 4-17: *Correlation boundary, interface and crack tip location
from test number 6*110

Figure 4-18: *Interfacial stresses from analytical model for test number 6*.....111

Figure 4-19: *Summary of stress intensity factors*.....113

Figure 4-20: *Summary of critical energy release rates*.....114

Figure 4-21: *Comparison of current study results to Yan (1998)*115

Figure A-1: *Description of a boundary segment*124

LIST OF TABLES

Table 4-1: *Numeric values of boundary displacements from test number 1 used to perform analytical stress analysis*.....96

Table 4-2: *Numeric values of boundary displacements from test number 2 used to perform analytical stress analysis*.....99

Table 4-3: *Numeric values of boundary displacements from test number 3 used to perform analytical stress analysis*.....102

Table 4-4: *Numeric values of boundary displacements from test number 4 used to perform analytical stress analysis*.....105

Table 4-5: *Numeric values of boundary displacements from test number 5 used to perform analytical stress analysis*.....108

Table 4-6: *Numeric values of boundary displacements from test number 6 used to perform analytical stress analysis*.....111

Table 4-7: *Numeric values of stress intensity factors*112

Table 4-8: *Numeric values of critical energy release rate*114

Table B-1: *Sample of output data from digital image correlation program*127

Table B-2: *Definition of DIC result parameters*.....127

Table B-3: *Sample of output data converted to units of microns*128

Table B-4: *Sample of output data relative to the crack tip*.....129

ABSTRACT

This dissertation concerns the development of a combined experimental and analytical technique to determine the critical values of fracture parameters for interfaces between dissimilar materials in electronic packages. Failure of materials and interfaces are commonly linked to the fracture parameters such as the stress intensity factors and the energy release rate. However, there exists no experimental procedure for the direct measurement of these fracture parameters. This dissertation reports on the development of a new technique to obtain these parameters by testing specimens created from post-production electronic packages. The results from the experimental testing are then used as the input for an analytical model which computes the desired parameters.

The experimental aspect of the research involves the bend testing of specimens inside the chamber of a scanning electron microscope (SEM) in conjunction with the digital image analysis. The specimens are thin strips of post production electronic packages. A crack is introduced along the interface in the specimen. Loading is applied to the specimen using the bend fixture and images are captured following each load step. Image analysis on these images provides the displacement field around the crack tip to be used as boundary conditions in the analytical model.

An analytical model is created because traditional finite element analyses of the stress state in regions with dissimilar elastic or viscoelastic materials are incapable of correctly resolving the stress state due to the unbounded nature of the stresses. A hybrid

formulation is developed utilizing the exact solution for the stress and displacement fields based on the eigenfunction expansion method under general loading. The region has two dissimilar viscoelastic material wedges with perfect bonding, and is not limited to a particular geometric configuration. The solution method is based on the principle of virtual work in conjunction with the use of Laplace transformation to eliminate time dependency. The strength of the singularity is obtained in the time space without resorting to approximate Laplace inversion techniques. However, the intensification of the stress components is obtained by employing an approximate inversion technique. The analytical model returns the stress intensity factors which are used in the calculation of the critical energy release rate.

One of the main contributions of this dissertation is the development of multiple techniques for the creation of test specimens from electronic packages. These methods involve different procedures of encapsulation for sectioning and techniques for the introduction of the crack to the interface. A second development is the technique of testing using image capture in conjunction with digital image correlation to find localized displacements. The third contribution from this work is the development of an analytical model to accurately model the region near the junction of two dissimilar viscoelastic materials. Six results were obtained for the critical energy release rate for the die/underfill interface. The mean value of the interfacial strength is 87.2 J/m^2 with a variation less than 25%. Comparison to published results for these values is favorable.

**A COMBINED EXPERIMENTAL AND ANALYTICAL APPROACH FOR
INTERFACE FRACTURE PARAMETERS BETWEEN
DISSIMILAR MATERIALS IN ELECTRONIC PACKAGES**

1. INTRODUCTION

Adhesive bonding is a primary means for connecting different layers of material in a microelectronic package. The main components of a package are the die, the die-attach (adhesive), and the substrate. It is unavoidable to form junctions of different materials while bonding these components. The bonding is achieved by using an adhesive whose shear modulus may relax over time exhibiting viscoelastic behavior. The junctions of the chip and die-attach (underfill) or the substrate and underfill are potential failure sites because of the presence of singular stress fields. The strength of the singularity and the intensification of the stress field depend on the geometry and difference in moduli. The strength of these interfacial bonds is a major concern in the electronics industry. Under operational temperature excursions, the mismatch in coefficients of thermal expansion between the silicon chip and underfill, and between the underfill and organic substrate, induces high stresses along the interfaces of electronic components. The occurrence of such a failure initiation can compromise the mechanical strength of the package as well as the integrity of the interface, which is critical to conduct heat away from the chip. Fundamental issues associated with dissimilar material interfaces arise primarily from a lack of information regarding critical interface fracture parameters.

Reliable strength predictions for regions involving an interface cannot be made unless the critical values of fracture parameters are available. As pointed out by Mahajan et al. (1999), measurement of the interface strength or critical interface fracture parameters is still an open issue. Hence, it is essential to understand the effect of geometry and material parameters on the singular behavior of the stress field near the junction of dissimilar elastic and viscoelastic materials under general loading conditions. Of particular interest in this dissertation is the determination of the interfacial bond strength between the underfill and other dissimilar materials in electronic packages because the cracking at this interface is one of the most common failure modes. As the size of electronic components decreases, the strength of the underfill becomes both process and length-scale dependent. For the aforementioned reasons it is essential that post-production end-user packages are used in the preparation of the interface strength test specimens. Special test specimens fabricated in the laboratory to simulate the package are incapable of fully capturing the process history that “real world” packages experience.

1.1 Experimental Background

The techniques for direct measurement of the interfacial strength on large components cannot be applied on electronic packages. The small length scale makes it impossible to attach direct measurement devices such as strain gages and extensometers. Other methods used to test interfacial strength (e.g. – peel tests, shear tests) cannot be used due to the materials used in package fabrication. Babu (1996) suggested the use of fracture

mechanics concepts to determine the adhesion strength of sprayed metallic coatings, but the procedure is easily extended to all types of interfacial strength investigations. This study used pre-defined cracks to determine the critical stress intensity factor and strain energy release rate. In order to use these methods indirect or non-contact measurement techniques must be employed.

Testing of pre-cracked specimens is most commonly performed in four-point bend fixtures. The conditions created by this test setup are inherently mixed mode [Howard (1991)] but the ratio between the modes is dependent on the specimen itself. End notched specimens, such as those used by Martin (1999), create conditions near the crack tip which are predominantly in shearing mode. This has the tendency to drive the crack away from the interface unless the material mismatch along the interface is such that the substrate is much stiffer than the overlaying material [Howard (1993)]. For specimens where the mismatch is less pronounced, the methods developed by Charalambides (1989 and 1990) are more commonly used. This test specimen uses a center notch in the upper material and the crack propagates downward to the interface. At the interface, the crack splits and follows the interface in both directions, creating two potential test sites.

Rice (1968) developed a path independent integral (known as the J-Integral) around a crack tip that gives the energy release rate. The integral requires knowledge of displacements and tractions along a closed path, quantities that cannot always be determined during experimental testing. Modifications to the J-Integral equation allows

for the experimental evaluation based on load-displacement curve data [Hornet (1995)]. For experimental J-Integral results to be valid, it is crucial for the measured quantities to be highly accurate. Work done by Howard (1993) revealed that displacement measurements can be affected by asymmetry in the specimen cracks, leading to erroneous results for displacement measurements during bend tests. Similarly, Charalambides (1990) found that the entire load applied during a bend test does not contribute to an energy increase at the crack tip. Thus, the method of experimental J-Integral evaluation based on load and displacement data from bend tests is inadequate for accurate determination of energy release rate.

Other indirect measurement methods applicable to small scale specimens with a pre-existing crack are those based on optical techniques. To accurately measure the effects of the crack tip itself, it is desirable to monitor the test region near the crack tip while the loading is applied [Wiklund (1997), Voevodin (2001), Bernard (2002)]. With a pre-existing crack in a small specimen, a high level of magnification is essential to capture changes in the specimen during testing. Systems using visible light (optical microscopes) are limited to magnification levels less than 1000X while suffering from a marked loss of depth of field as the magnification increases. The scanning electron microscope (SEM) provides an alternate method of achieving high magnification of up to 300,000X, and also with a much larger depth of field. Performing the test inside the SEM chamber using a four-point bending fixture permits the monitoring of the crack tip deformation by capturing images near the crack tip.

The most commonly used optical techniques are variations of Moiré interferometry and image correlation. While other methods are available, they are usually limited to special applications. Moiré methods rely on the generation of interference patterns arising from the deformation of a grating on the specimen when illuminated by a reference light source. A camera is then positioned to record the fringe patterns which, after further analysis, give the displacement fields. The major shortcoming of this technique is the necessity to create a reference grating on the specimen, which must then be illuminated by a reference light that passes through an identical grating. However, no light source is used with the SEM. The image is formed only by the return of electrons incident on the surface. Although it is possible to perform Moiré analysis in an SEM chamber [Read (1996)], the specimen preparation requires a clean room. Therefore, many investigators resort to image correlation, a simpler, cheaper, yet highly effective technique [Vogel (2001)]. Image correlation is a comparison of an image taken before a load step with one taken afterwards. Features on the reference (before) image are located in the target (after) image and then the displacement and rotation components are calculated. The actual correlation is usually automated with dedicated application software. For this study, the digital image correlation technique was deemed to be the best method for displacement measurement.

To improve the chances of finding landmarks (points) during image correlation, the creation of reference marks (points) on the specimen surface has been found to be highly

effective. The techniques employed to apply the reference points can be divided into two groups: lines and points. Lines have been applied to the specimen in one direction (for example, vertically, as done by Takeda (1999)) and used to measure the displacements of samples loaded in the SEM chamber. Creating a grid pattern using reference lines has been used for macroscopic evaluation of out-of-plane impact deformations [Rae (1999)] but has not been extensively used for in-plane displacement measurements.

In-plane displacements have been determined more often by reference points placed on the specimen surface. These reference points can be created by application of a material randomly, like a powder [Theocaris (1990)], or by the creation of points in a serial manner by ablation of the sputter material with the electron beam [Theocaris (1988)]. The drawbacks of these methods are that the random material application may not create enough, or may create too many, reference points near the region of interest. Thus, there is most likely a few iterations required before the ideal “random” distribution is found. The major shortcoming of the ablation method is the significant amount of time needed for the removal of the sputter material. Also, the sputter material cannot always be removed. For example, gold has a much higher atomic weight than aluminum; therefore, a gold layer would take a considerably long period of time to ablate even if enough energy could be generated by the electron beam (which usually cannot be done).

Correlation techniques using speckle coated specimens also exist [Sun (1997), Luo (2000)]. The speckle method usually requires a stereo pair of images at each load point

to obtain an acceptable correlation between image points. These points are then tracked between images in the same manner as with other images. The major obstacle is the creation of a speckle pattern on an SEM specimen. Since the SEM is sensitive to topographic and atomic weight differences in the sample, the speckle pattern must be created using sputter material of very different atomic weights; since the sputter coat would be essentially flat, the topographic differences would be effectively zero. The only option is then to create one layer of a high weight material such as gold or palladium and then apply a second coat of carbon or aluminum for a short time to create the pattern. Because these materials require separate equipment this involves additional investment and the technique might not be feasible even with the equipment available. Therefore, the speckle technique of image correlation becomes less desirable when used in conjunction with an SEM.

Some specimens used in conjunction with the digital image correlation method do not require any special surface preparation. If the appearance of the specimen is unique enough at most of the points, the software is able to accurately determine displacements between images. This also has the added benefit of removing any materials that may mask the true behavior of the underlying specimen. Thus, whenever possible, it is preferable to use the specimen itself as the reference points.

Work has been recently done by Yan (1998) to determine the interfacial fracture toughness of flip-chip assemblies using a four-point bend test. Yan fabricated a three-

layer test specimen consisting of a die, underfill, and circuit board, while reproducing the major components of an electronic package, it fails to account for the effects of processing on the materials. The results of Yan's work were determined by experimental J-Integrals based on load-displacement curves, the validity of which was discussed earlier in this chapter. Furthermore, Yan used end notched specimens which have the tendency to crack away from the interface. Thus, Yan's work is a good attempt towards measuring the energy release rate; however, it is by no means the ideal approach.

Klingbeil (1997) and Howard (1991) discussed the effects of residual stresses in the determination of interfacial fracture parameters. Both studies involved metal layers deposited at very high temperatures. While they concede that residual stresses exist and can be large enough to affect the results, they also state that the magnitude of the stresses is dependent on the steps used in processing. For electronic packages, where the underfill is applied in one step at a relatively low temperature, the residual stresses can be assumed to be low. If the residual stresses are ignored, the measured energy release rate becomes slightly lower than the actual value if no stresses were present [Klingbeil (1997)]. Thus, the experimentally determined values are conservative and good for failure prediction. A final aspect to consider is that all post-production electronic packages contain some residual stress, so the creation of a specimen without these stresses would not accurately model real-world conditions and would give a higher energy for failure than would actually be seen.

1.2 Analytical Background

Failure of the interface is linked to the critical stress intensity factors and the energy release rate. There exists extensive literature on mathematical modeling of the failure phenomena utilizing these parameters. As reported by Williams (1952), the stress state near the junction often has a singular behavior and the nature of the singularity is a function of the junction geometry and the elastic constants of the materials. The previous analytical studies concerning the junctions of elastic materials by Bogy (1968), Hein and Erdogan (1971), and Theocaris (1974) were limited to asymptotic solutions with the leading order term only; thus, the stress field was accurate at a distance very close to the junction point. These asymptotic solutions suffer from accuracy at distances slightly away from the junction point, as reported by Qian and Akisanya (1999). Furthermore, the asymptotic solutions only provide information on the strength of the singular behavior, not on the intensity of the singularity essential for predicting failure initiation. In an effort to determine the stress intensification at the free edges, Akisanya and Fleck (1997) developed a method that utilizes a traditional finite element combined with Betti's reciprocal theorem involving a path-independent contour integral. As an extension of this approach, Qian and Akisanya (1999) showed that the asymptotic solution with a leading-order term is not sufficient to capture the accurate behavior of the singular stress field near the junction. Solutions obtained by this method are also dependent on the finite element mesh density influencing the numerical evaluation of the path-independent integral.

Although the extension of these previous techniques to consider time dependent material properties is not difficult in the Laplace domain, the construction of the solution in the time space through the Laplace inversion integral is rather complex without resorting to numerical integration. However, disregarding the history dependence of stress in viscoelastic materials permits the direct use of previous asymptotic solutions. In this approach referred to as the quasi-elastic method, the material properties are evaluated for a specified value of time and subsequently used in the elastic solution to find the strength of the singularity and the corresponding stresses. Although this approach seems to lead to relatively acceptable values for the strength of the singularity and the stresses, the error invoked is fundamental in nature and that the hereditary integrals are disregarded from the stress-strain relations of viscoelastic materials.

In order to account for the history dependence of the stresses, the Laplace transformation is utilized. In the Laplace domain, the governing equation associated with the viscoelastic material is analogous to that of an elastic material. This analogy, known as the correspondence principle, permits the construction of the solution in the Laplace domain by using the solutions available for elastic materials after appropriate substitutions. However, it requires the inversion of the expressions for the stress and displacement components from the Laplace domain to time space. The inversion is usually achieved by employing numerical methods especially for algebraically complex expressions.

Concerning the singular stress field near the apex of a viscoelastic wedge, Atkinson and Bourne (1989) studied the time dependent singular stress field at the tip of a semi-infinite crack perpendicular to the interface between two dissimilar viscoelastic materials for anti-plane strain deformation. Under plane strain conditions, Bourne and Atkinson (1990) studied the time dependency of the stress field near the corner of a homogeneous and viscoelastic wedge with a re-entrant corner under prescribed displacements. In these studies, the solution methods were based on integral transforms in both space and time while representing the viscoelastic material as a standard linear solid. The general asymptotic expressions were derived in the transformed space. The expressions for stress and displacement fields were computed at specific distances from the apex by performing numerical integration for the inversion process.

Blanchard and Ghoniem (1989) considered the singular thermal stress relaxation near the edge of an interface between two dissimilar viscoelastic quarter planes. Their solution method also utilized integral transforms in space and time while applying the elastic-viscoelastic correspondence principle. The numerical procedure for the inversion of the Laplace transform was based on the Gaussian quadrature method to perform an approximate mapping between time space and Laplace domain, which is only valid for real valued solutions in the Laplace domain. This limits the application of this numerical inversion method.

Employing the integral transform techniques, Lee (1997, 1998) derived the analytical expression for the strength of the singularity at the intersection of free edges and the interface between an elastic quarter plane and a viscoelastic quarter plane. However, the stress components were calculated by invoking this solution form into the time-domain boundary element method that eliminates the Laplace inversion process and accounts for the presence of finite geometry. In this study, the viscoelastic material was represented by a shear relaxation modulus with a time exponent and a time-independent Poisson's ratio.

The solutions given by Lee (1997, 1998) and Blanchard and Ghoniem (1989) are restricted to the geometry of two bonded quarter planes. In addition, this particular geometric configuration results in the numerical inversion that is performed in the domain of real valued Laplace transform variable. These integration methods rely on approximating the complex Laplace inversion integral. These methods require a priori knowledge of the singularities in the domain of integration. In order to avoid these numerical integrations of the Laplace inversion integral, approximate methods were introduced for a one-to-one mapping from Laplace domain to time space based on the evaluation of the solution in Laplace domain. Approximate inversion methods introduced by ter Haar (1951) and Schapery (1961, 1965) employ simple mapping functions with known constants.

1.3 Summation and Roadmap

This dissertation extracts the critical fracture parameters for the underfill in an electronic package based on displacement measurements around an interfacial crack tip. The samples created from production line packages are subjected to four-point bending test in the SEM chamber. During testing, as the loading is increased, the images near the crack tip are captured for digital image correlation. The measured displacements around the crack tip serve as boundary constraints for the stress and strain analysis using a finite region model.

A solution for the finite region model is developed based on the principle of virtual work in conjunction with the use of Laplace transformation to eliminate time dependency. The strength of the singularity is obtained analytically in the time space without resorting to the approximate Laplace inversion techniques. However, the intensification of the stress components is obtained by employing an approximate inversion technique. In the Laplace domain, the solution method satisfies the equilibrium equations exactly, and that the applied loading conditions are satisfied approximately in the sense of energy minimization.

The solution method presented here is an extension of the study by Lee (1997) and Barut et al. (2001) in conjunction with the approximate inversion method by Schapery (1961) to obtain the strength of the singular stress field exactly and their intensification approximately in a finite region of dissimilar viscoelastic materials with traction free

edges and arbitrary geometry. The energy release rate, based on the results of the finite region model, is calculated using Hutchinson's (1991) extension of the work by Malyshev (1965) for a bimaterial interfacial crack. The energy release rate is used as the parameter for interfacial strength since as reported by Charalambides (1990) the stress intensity factor is scale dependent while the energy release rate is scale insensitive.

The experimental investigation focuses on the procedure for creating test specimens from post-production packages, the equipment and fixtures used during testing, and the digital image acquisition process. The analytical portion of the study includes the statement of the finite region model problem and the development of the solution. The experimental work is presented in Chapter 2 and the analytical work is given in Chapter 3. Chapter 4 reports the numerical results from the experimental testing, the validation of the analytical model, and the final results when the model is applied to the experimental data. The conclusions are given in Chapter 5.

2. EXPERIMENTAL INVESTIGATION

Chapter 2 details the experimental investigation conducted during this study. This investigation begins with a post-production package and concludes with the determination of the displacements used as input for the analytical model described in Chapter 3. To achieve this goal the sample package is cut into thin cross-sections using different techniques developed during this study. The cross-sections are then cracked to create sites along the interface where the tests can be performed. Testing involves placing the specimens in a bend fixture within a scanning electron microscope (SEM) and capturing images as the load is applied. When the crack propagates, the test run is complete. The captured images are then processed by digital image correlation to determine the displacements around the crack tip during the testing. These displacements are used as the boundary conditions for the analytical model.

2.1. Specimen Preparation

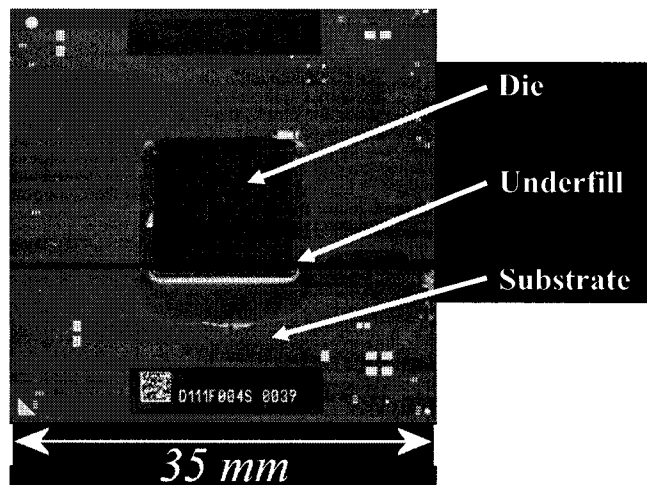


Figure 2-1: *Post-production electronic package sample.*

The most important aspect of the specimen preparation is to create test specimens that are representative of the sample packages. The final desired product is a thin cross-section of the original package that has not been subjected to excessive damage during the specimen preparation phase. To accomplish this, the post-production package, an example of which is shown in Figure 2-1, is encapsulated in a support matrix. The encapsulated sample is then sectioned using a diamond wafering saw into thin strips (see Figure 2-2a) that maintain the integrity of all the package components shown in Figure 2-2b. These specimens are removed from the support matrix and a crack is introduced into the interface using one of two techniques. Finally, the cracked specimen is cleaned and sputtered for imaging in the SEM.

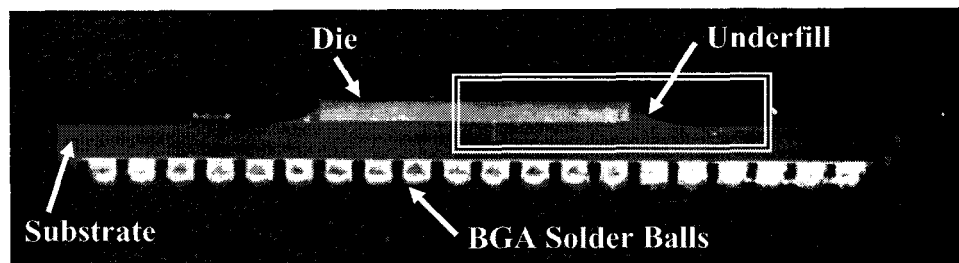


Figure 2-2a: *Cross-section specimen of electronic package.*

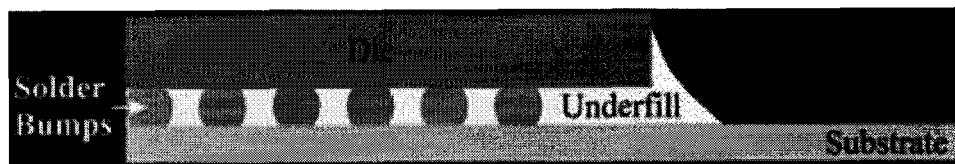


Figure 2-2b: *Schematic of highlighted portion of Figure 2-2a.*

2.1.1. ENCAPSULATION

Sectioning an electronic package introduces severe damage to the die owing to shattering when the package is not properly encapsulated with a support matrix. Necessary reinforcement for the die is provided by this support matrix, which must be removed

prior to the bending test. The support matrix (encapsulant) must be stiff enough to prevent the die from deflecting during the sectioning process but must also conform to the shape of the package to eliminate any gaps between the encapsulant and the package. These requirements are satisfied by covering the package with an initially liquid matrix material which later solidifies to form a stiff encapsulation.

In order for the support matrix to be removed following the sectioned procedure, one technique is to place a barrier to be placed between the package and the support matrix material prior to encapsulation. The barrier can be either a spray-on coating or a solid material formed around the package that does not bond to the package. Both of these methods of introducing a barrier were investigated during the study using epoxy as the encapsulation material. An alternative technique for the removal of the support matrix is to use a material that can be dissolved from the specimens following sectioning. Two methods that involve dissolving were developed in this study.

2.1.1.1. Spray-On Barrier Materials

The first method to prevent the electronic package from bonding with the encapsulant was to spray a coating over the sample before encapsulation. Spray coatings tested were Teflon, composite mold release, and graphite. During all tests, multiple coats were applied allowing for sufficient time between applications so that the previous coat completely dried out. Samples were then placed in an encapsulation mold and covered with epoxy.

The results of the tests showed that none of the samples could be removed from the epoxy support matrix. Visual examination of the samples revealed that spray coating flakes were suspended in the epoxy, leading to the conclusion that the epoxy was removing the spray coating as it was poured into the mold. Subsequent tests performed by pouring epoxy around the package instead of directly onto the package did not alleviate the problem. The most likely cause is that the viscosity of the epoxy is high enough that as it flows over the package it scrubs portions of the coating off allowing the matrix material to bond to the package in some locations. Even though the epoxy is not bonded to the entire package surface, the partial bonding is strong enough to prevent removal of the encapsulant. Based on the outcome of these tests, use of spray coating to protect the package from bonding with the support matrix material was deemed to be not feasible.

2.1.1.2. Solid Barrier Materials

Results of the spray coating investigation showed that even if a small percentage of the surface area of the package bonds to the encapsulant, it is not possible to separate the package from the epoxy. Therefore, the solid barrier materials must satisfy three main requirements: barrier materials must (i) be completely impermeable to the matrix material, (ii) conform perfectly to the surface topography of the package avoiding air pockets around the die which may lead to lack of support, and (iii) be transparent allowing for visual alignment of the package during sectioning.

The materials selected for testing were Aclar and Con-Tact paper as they met all the requirements dictated for the barrier materials. Moreover, they did not bond to epoxy, making them better candidates to protect the package. Aclar is a fluorine-based material available in sheets; it is very similar in appearance to overhead transparencies. Aclar is used for specimen preparation of biological samples and packaging of medicinal products. Con-Tact paper is sold in retail stores for the lining of drawers and home-craft projects. Con-Tact paper comes on rolls and is much more pliable than Aclar.

Covering the package with the barrier material was accomplished by placing the material around the package at room temperature and then thermoforming it so that it conformed completely to the package geometry. For Aclar, two squares were cut to allow an extra quarter-inch of material on all sides of the package; for the Con-Tact paper, a rectangular strip was cut and wrapped around the package to achieve the same amount of excess material on all sides. The Con-Tact paper was then pressed into the package edges using a blunt edged tool, resulting in the package self-sealing at room temperature prior to thermoforming.

Thermoforming of the materials was done using the method of vacuum-bagging adopted from composite material fabrication. This technique places the specimen in a sealed bag connected to a vacuum pump. The bag conforms to the shape of the material within applying a constant pressure over the entire surface. While continually maintaining the vacuum, the bagged specimen is placed in an oven at elevated temperature. Using this

method on the Aclar did not yield good results. The Aclar failed to completely mold to the package contours even as the oven temperature was raised to that near the melting point of the solder used in the package. Another drawback is that when thermoformed Aclar will not self-seal at locations where two pieces of the material are in direct contact. This required the application of epoxy resistant tape along the edges to completely seal the package.

Results from the Con-Tact paper tests were satisfactory. The Con-Tact paper formed to the package geometry at room temperature better than the Aclar did after thermoforming. In addition, the Con-Tact paper was self-sealing at room temperature. Application of the thermoforming process molded the Con-Tact paper perfectly to the package contours. A package covered with Con-Tact paper is shown in Figure 2-3 after it has cooled following the thermoforming process.

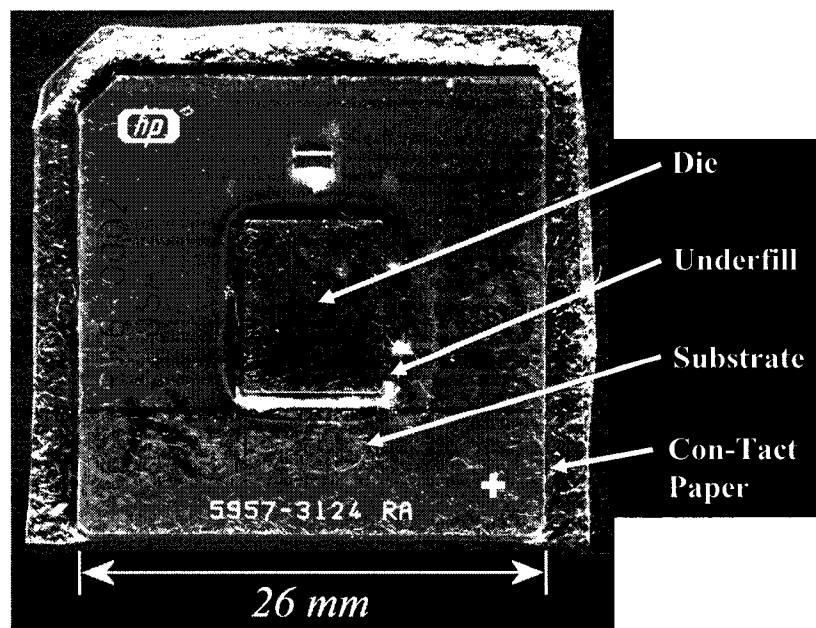


Figure 2-3: Package covered with thermoformed Con-Tact paper prior to encapsulation.

Tests on thermoforming were performed using the Con-Tact paper using different duration and temperature combinations. It was found that at temperatures 280 °F that the Con-Tact paper began to show noticeable signs of degradation due to the elevated temperature. The material developed a brownish color and a loss in flexibility at this temperature. Tests at temperatures between 200 °F and 275 °F revealed that the lower temperatures required longer durations of thermoforming. At 275 °F, only an hour was required while 200 °F needed over four hours to achieve less effective results. For this study, all thermoforming was done at 225 °F for 90 minutes.

2.1.1.3. Encapsulation Materials

The encapsulation material should be selected based on two criteria: (i) transparent encapsulant allowing alignment of the package during sectioning and (ii) easy and complete removal following sectioning. Thus, epoxy was selected as one of the support matrix materials.

For packages that have sharp geometry changes, Con-Tact paper is not always capable of forming completely to the contours. In addition, for packages of configurations other than flip chip (e.g.- wire bonded packages), a method is necessary so that the matrix is applied directly to the package without the need for a barrier material. The need for this form of encapsulant is essential for packages where Con-Tact paper cannot be perfectly molded to the package contours due to internal voids or a package geometry that is not favorable when using the solid barrier material technique. This would require an

encapsulant that can be dissolved in a solvent without harming the package. Epoxy dissolvers are available that will soften and/or dissolve cured epoxy. However, because most substrates use epoxy for the matrix material, use of an epoxy dissolver may damage the specimen, so its use is limited to select samples.

Another polymer, Methyl Methacrylate/Butyl Methacrylate (MBM), is commonly used to encapsulate biological samples for sectioning. The two components of MBM have the appearance and consistency of water, creating a very low viscosity encapsulation material. MBM cures hard and transparent, and is easily dissolved when placed in an acetone bath. For this polymer, the curing must take place in a water bath because the temperature cannot exceed 70 °C at any time during the cure cycle. If the temperature exceeds this value, an exothermic reaction occurs that boils the polymer as it cures, ruining the specimen. The water bath is necessary as it serves as a heat sink; absorbing excess heat generated during the cure cycle to maintain a constant temperature of the encapsulant. Working with MBM requires good ventilation and protection for the eyes and skin, making specimen preparation more difficult than that using epoxy. With the low viscosity of the material, low curing temperature, and the relatively mild solvent required to remove it, MBM is an ideal encapsulation material for samples with wire bonding or other delicate features that may be damaged during the Con-Tact paper thermoforming process.

Before preparing any specimens from an electronic package, preliminary evaluation of the package is necessary to determine which encapsulation technique should be used. One bare package should be placed in epoxy dissolver at an elevated temperature for at least 12 hours. If, after removal from the dissolver the package shows no damage, package encapsulation using epoxy can safely be performed without using Con-Tact paper. For packages damaged by the epoxy dissolver, a visual inspection of the package geometry is needed. For a sample with internal voids or a geometry configuration that would create air pockets when Con-Tact paper is applied, MBM encapsulation is necessary. For all other packages, encapsulation using Con-Tact paper and epoxy is acceptable.

2.1.1.4. Encapsulation Molds

Encapsulation is performed in a mold that does not bond to the matrix material. For smaller samples to be encapsulated with epoxy, plastic clips are applied to the edges of the sample allowing the epoxy to flow under the package. The clipped specimen is then placed in a disposable encapsulation cup, shown in Figure 2-4, and the encapsulation applied. As the epoxy cures, hot spots commonly form. For room temperature cures, these hot spots create localized softening of the encapsulation cup, deforming the cup and even rupturing. To reduce these effects, the cups are placed in a water bath at room temperature during the curing process. After the epoxy fully cures, it is removed from the disposable cups and placed in an oven at 150 °F for one hour to ensure that the epoxy is fully cured before sectioning. If not completely cured, epoxy will bind to the diamond wafering saw during sectioning, shattering the blade. Because of the softening observed

in the disposable cups above room temperature, they are not used for MBM encapsulation.

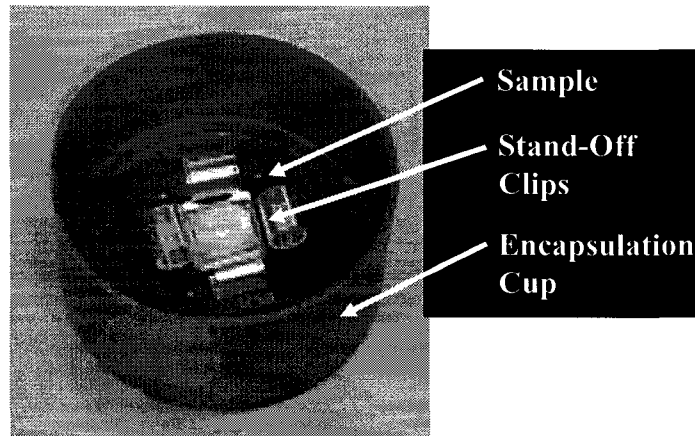


Figure 2-4: *Sample with stand-off clips in a disposable encapsulation cup.*

A mold fixture was designed and built for the specific purpose of encapsulating large samples or when using MBM. The mold employs moveable side walls and has an insert for the base as shown in Figures 2-5a,b. The edges of the mold are sealed with oil-based modeling clay creating a watertight cavity. The material for the mold walls and base is ultra high molecular weight polyethylene (UHMW-PE) with stand-off pins in the base made from oil-impregnated cast Nylon 6. These pins hold the sample above the mold base to facilitate epoxy flow under the package. The metal base and wall supports are fabricated from aluminum. A lid of UHMW-PE can be affixed to the top of the cavity, allowing the mold to be completely submerged in water for temperature control during the curing process. UHMW-PE is highly resistant to bonding by the encapsulation materials while the oil-impregnated cast Nylon 6 is resistant but requires a surface coating. To further aid the removal of specimens after encapsulation, the mold surfaces are coated with either a spray-on composite mold release or with a silicone-based

lubricant. The cure temperatures of the encapsulation materials used in this study were below the glass transition temperature (GTT) of the UHMW-PE, but for higher temperature applications, the UHMW-PE parts can be removed from the aluminum backing plates and replaced with identical parts made from oil-impregnated cast Nylon 6 which has a higher GTT. Plastic stand-off clips are not required due to the integrated stand-off pins in the base but may be used if desired.

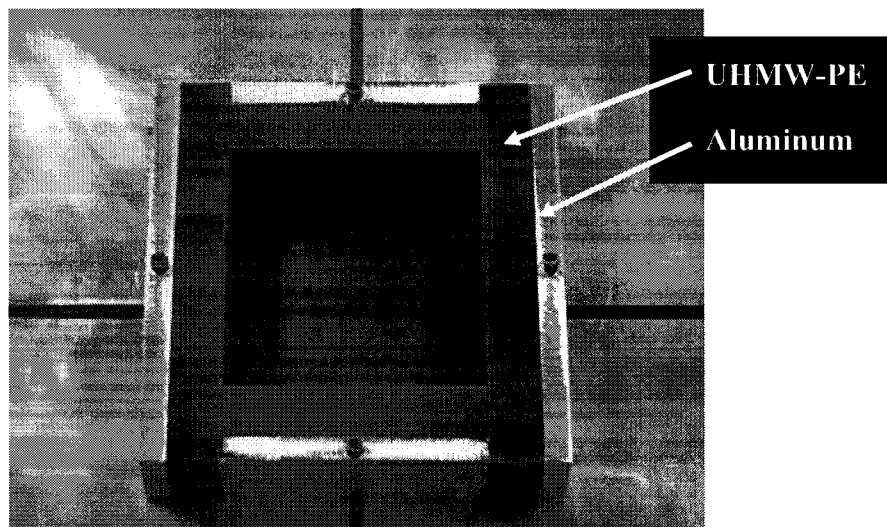


Figure 2-5a: *Custom-built encapsulation mold with face plates closed.*

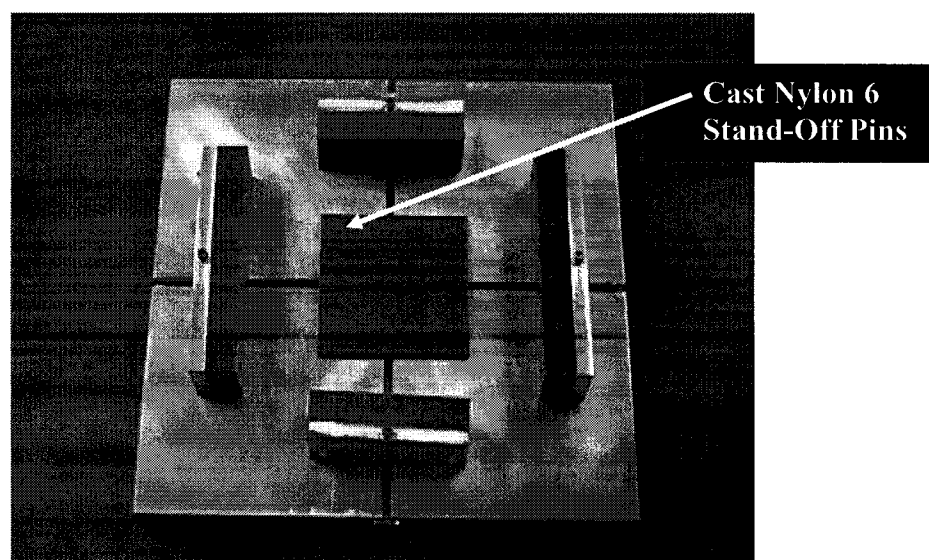


Figure 2-5b: *Encapsulation mold with face plates opened.*

2.1.2. SECTIONING

Once the sample is encapsulated, cross-sections are removed using a diamond bladed wafering saw. The original saw fixture was incapable of gripping the encapsulated samples properly, requiring the fabrication of a custom fixture. The fixture, shown in Figure 2-6, allows the specimen to be rotated so that the blade engages the die first. This cuts the die in compression and minimizes damage to the package during sectioning. A water-based coolant liquid is used in the saw sump because of problems reported using oil-based coolants when sectioning electronic packages of absorption of the coolant into the package materials. Cuts are made into the package perpendicular to the edge of the die with the thickness of the cuts varying from 0.5 to 2 mm, dependent on the amount of damage observed as the package is cut, as thinner cuts are more susceptible to die damage. Figure 2-7 depicts a specimen after sectioning (the sample is covered with Contact paper and encapsulated in epoxy).

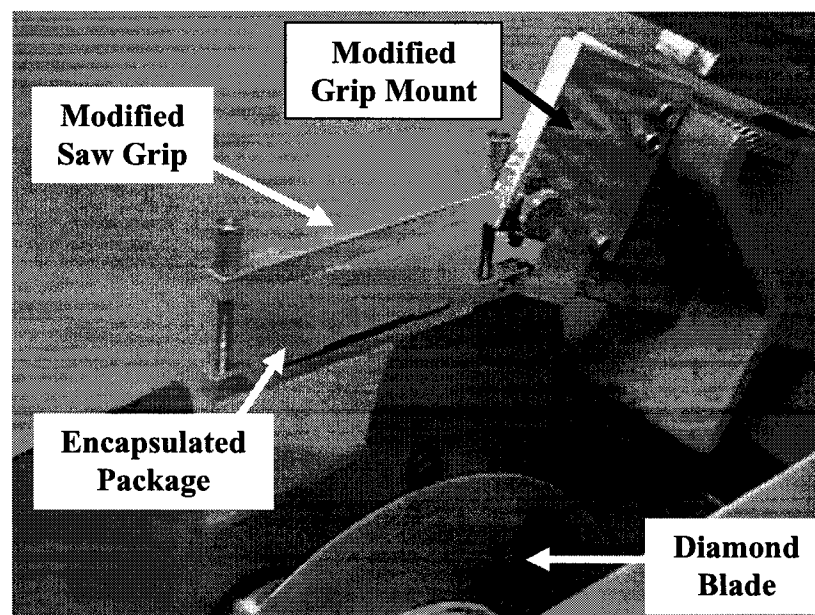


Figure 2-6: *Modified sectioning saw fixture.*

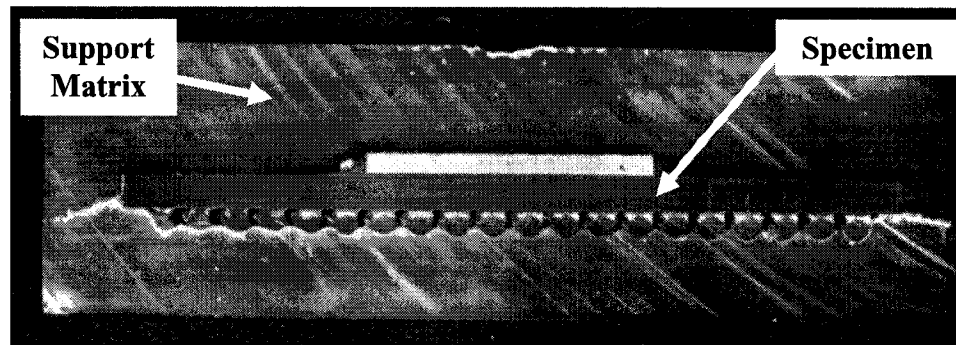


Figure 2-7: *Package section before removal from support matrix.*

2.1.3. MATRIX REMOVAL

After the sectioning process, the support matrix needs to be removed so that bending can be applied to the specimen. Two means of matrix removal were used during this study: mechanical and chemical methods. The matrix material could be removed mechanically if the encapsulant was not bonded to the package or the strength of the bond was weakened enough to allow the specimen to be removed with minimal force.

2.1.3.1. Chemical

The need for a chemical means to remove the support matrix is for the specimens where the encapsulation is in direct contact with the package surface. For packages in an MBM matrix, the specimens are placed in acetone. As the matrix is dissolved, the effectiveness of the remaining acetone is reduced due to contamination, which may require the replacement of the solvent if a large number of samples are placed together. The process can be performed at room temperature without any mechanical agitation but the speed of the removal is enhanced by elevated temperature and solvent movement. If the temperature is too high, the acetone will evaporate quickly, limiting the speed at which the material can be removed. The most effective method found was to place a beaker of

acetone in an ultrasonic cleaner with the water warmed to 30 °C. Specimens must be removed from the acetone solution immediately after the matrix is dissolved because if left for an extended period of time, the acetone will evaporate and the dissolved matrix material will solidify on the bottom of the beaker and the specimens.

The second chemical means of matrix removal was to use epoxy dissolver. This solvent dissolves and softens cured epoxy but does so indiscriminately. This creates problems with organic substrates, a majority of which are FR-4, a fiberglass/epoxy composite. All the organic substrates of packages used in this study, with the exception of one, were damaged when placed in epoxy dissolver, limiting its use. Another problem with epoxy dissolver is that it cannot come into contact with skin and the fumes should not be inhaled, especially when the solvent is heated. Because epoxy dissolver must be heated when used, a beaker of the solvent with specimens was placed in an air-tight oven. Instructions for the epoxy dissolver recommended that the solution be raised to 150 °C when used but experiments at this temperature found that the solvent evaporated rapidly. Reducing the working temperature to 75 °C eliminated the evaporation problem, allowing the specimens to be left in the oven for 12 hours with the heat on, followed by 12 hours with the heat off.

Once the cycle was complete, the fumes from the oven were vented out of the laboratory and the beaker removed from the oven. Even after 24 hours, not all the epoxy would dissolve, however it was found to dissolve at all edges of the matrix material, so the

specimen would fall out of the support matrix with minimal force, if needed. Specimens removed from the epoxy dissolver were placed in a beaker of acetone to clean off any residue from the epoxy dissolver. The solvent was found to be stable at room temperature for extended periods of time and could be reused multiple times before the effectiveness was reduced enough such that the solvent needed to be replaced.

2.1.3.2. Mechanical

For specimens covered with Con-Tact paper, epoxy dissolver could be used if the substrate was unaffected by the solvent, but the time required for the chemical removal is over 24 hours. A quicker method to remove the encapsulation is to mechanically remove it using a razor edge. In Figure 2-7, fine lines can be seen on both sides of the package edge. These lines are the edges of the Con-Tact paper in the matrix material. If a razor is pressed against the encapsulant between the edge of the encapsulant and the end of the Con-Tact paper, the matrix material fractures. Repeating this on both sides and then pulling on the top and bottom of the encapsulant allows the specimen to be freed immediately after sectioning.

2.1.4. CRACK INTRODUCTION

In order to create a testing site, a crack is introduced along the interface. Because of the solder bumps found in the underfill layer in the post-production packages, it was necessary to only use specimens where the crack tip was not in or immediately adjacent to a solder bump to ensure that the test results were unaffected by the solder bump. Two types of cracks were investigated: end cracks, which propagate towards the center of the

specimen when loaded, and center cracks, which propagate from the center out to the ends. For all crack types, a crack precursor was introduced to help control the starting location of the crack.

2.1.4.1. End Cracks

To form an end crack, the interface must first be compromised to create a site for crack propagation. As illustrated in Figure 2-8, the fillet of the underfill was scribed to create a blunt crack tip. Cracks were then driven inward from this point to create a sharp crack for testing.

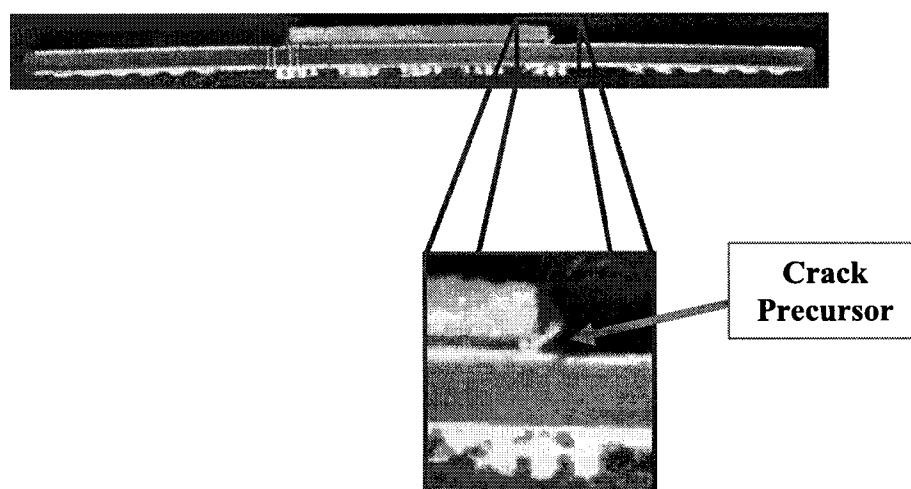


Figure 2-8: *Crack precursor scribed in the underfill fillet.*

The first technique used was to drive the crack inward using thermal shock. The specimen was cycled between liquid nitrogen and hot water to generate thermal stresses. Due to the coefficient of thermal expansion mismatch between the die and substrate, the substrate would experience larger thermal strain. This would cause the substrate to bend away from the die on each low temperature cycle, driving the crack inward. Experiments performed on the specimen found that performing the cycling manually was too slow to

generate the number of cycles required to drive the crack. Thermal shock chambers could automate this task but would take weeks, if not months, to generate the desired crack. Based on these results, thermal methods for crack generation were not pursued further.

Mechanical means to drive the crack were based on the three-point bend fixture. The blunt crack tip was placed over the center load point and the anvils moved together. This generated cracks in all specimens but very few of the cracks followed the interface. Most of the cracks were failures of the die and/or substrate. After extremely limited success, the end crack specimen configuration was abandoned for center cracked samples.

2.1.4.2. Center Cracks

The center cracked specimens were both based on existing techniques but modified for the electronic package samples used in this study. The first method was described by Cao (1989) to create interfacial cracks in brittle specimens. The second specimen is based on standard test specimens for interfacial strength determination.

2.1.4.2.1. Scribe

The scribe technique introduces a crack initiation point on the upper surface of the die using a glass cutter or similar tool to create a fine scratch in the top surface. When placed under three-point loading, the scribe line is the most probable failure point. The cracks from this location propagate down and out from the scribe line towards the interface as shown in Figures 2-9a,b. When the crack reaches the interface, it will follow the

interface if propagation in that direction requires less energy than moving through the bulk materials.

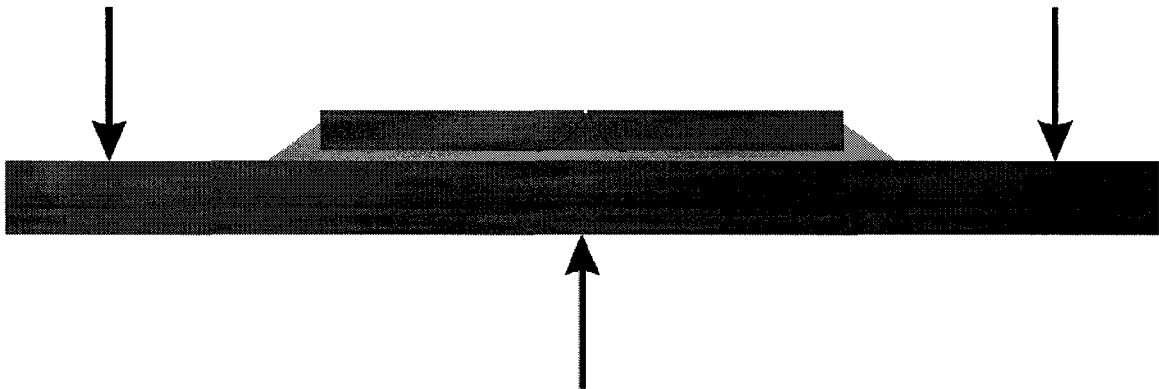


Figure 2-9a: *Schematic of scribe method specimen crack introduction.*

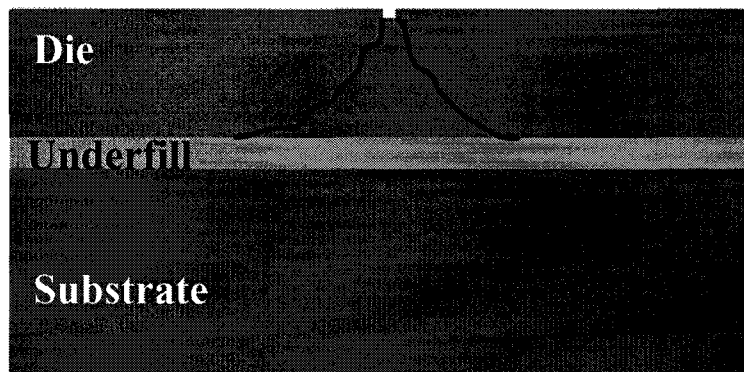


Figure 2-9b: *Detail of crack propagation schematic from Figure 2-9a.*

To minimize equipment changes in the SEM stage, the crack introduction using the scribe method was performed in a separate three-point bend fixture that was monitored using an optical microscope or magnifying lenses. The bend fixture under an optical microscope is shown in Figure 2-10. Tests performed on specimens resulted in cracks propagating as expected in a majority of the samples. One problem was that if the crack moved too far horizontally before reaching the interface, failure of the interface and substrate became

more likely. These failures resulted in vertical cracks forming through the underfill and substrate ruining the sample. It was also found that when the crack opening was large enough to be seen at the interface under the microscope or lens that failure of the underfill or substrate had already occurred. These failures were not apparent until viewed under the SEM. To avoid this, three-point bending was halted before the cracks appeared to reach the interface.

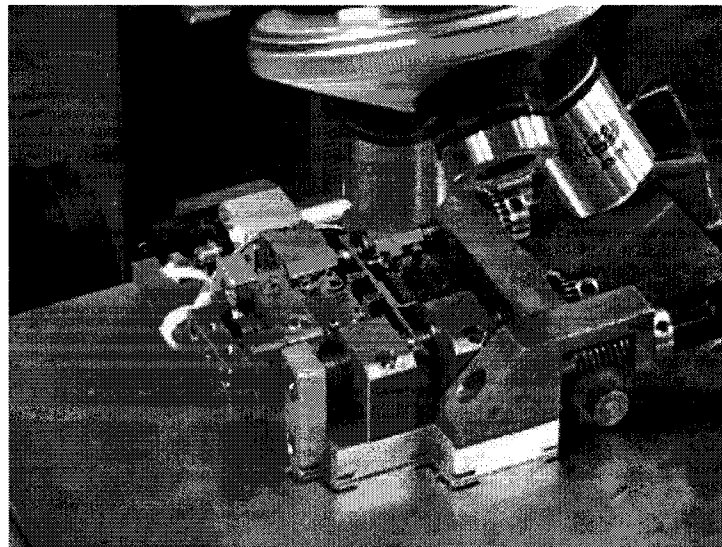


Figure 2-10: *Bend fixture under optical microscope.*

2.1.4.2.2. Notch

The notch specimen was an effort to recreate from the electronic package specimen a standard four-point bend specimen used for interfacial strength determination. A schematic of the standard specimen is shown in Figure 2-11a with the schematic of a specimen created from the electronic package is shown in Figure 2-11b. When the four-point bending is applied, failure occurs along the interface starting at the bottom corners of the notch.

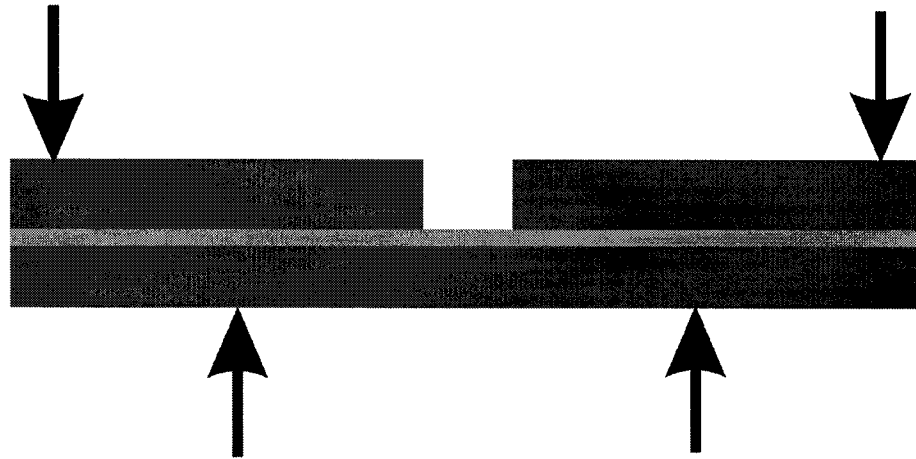


Figure 2-11a: *Standard four-point bend specimen for interfacial strength determination.*

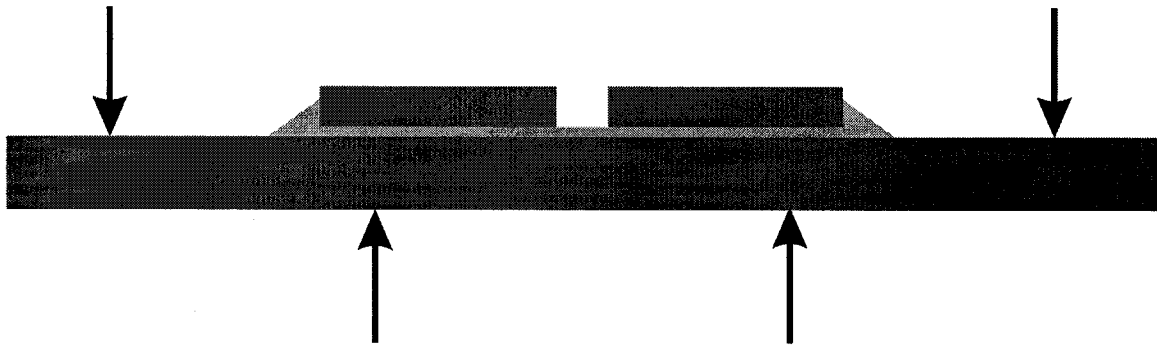


Figure 2-11b: *Schematic of notch method specimen.*

Because of the difficulties in creating a notch that terminates at the interface, most test specimens stop just above the interface, leaving a thin layer of material at the bottom of the notch. When bending is applied, the cracks propagate from the bottom corners of the notch through this thin layer to the interface. The cracks then propagate along the interface from this point.

The creation of a notch in the electronic package specimens was done using the sectioning saw. To support the die during this procedure, the technique of encapsulation was used, as explained in section 2.1.1. During the manufacturing process, voids can

form within the electronic package. Sectioning of the package exposes these pores which become potential sites for bonding during the second encapsulation process. To prevent this, all cross-sections were covered with Con-Tact paper and thermoformed before encapsulation in epoxy. The notch could then be cut into the die and the specimen removed from the matrix as before. Figure 2-12 shows an image of the bottom of the notch created using this process. The curvature is created by the shape of the saw blade.

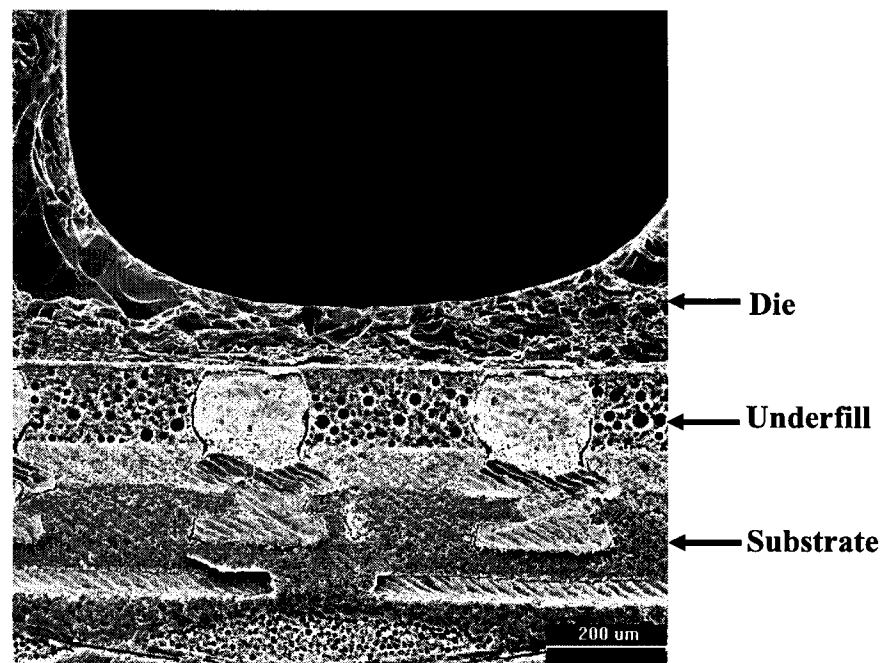


Figure 2-12: SEM image of notch.

2.1.5. CLEANING

The residue of the Con-Tact paper or encapsulant as well as any debris from the cutting procedure is removed using a multi-step ultrasonic cleaning procedure. The sump of the ultrasonic cleaner is filled with water and heated to 50 °C. Two beakers are placed in the ultrasonic cleaner: a beaker of water with a mild detergent and a beaker of clean water.

The specimens are allowed to reach the temperature of the sump before cleaning begins. The specimens are placed in the detergent and cleaned for at least 10 minutes before being moved to the beaker of water for at least 10 more minutes of cleaning to remove the detergent. The specimens are removed from the water and placed in a third beaker of acetone outside of the cleaner. The beakers in the ultrasonic cleaner are removed and the acetone filled beaker is placed in the cleaner. Because of the volatility of the acetone, it is not heated before starting the cleaning but is allowed to warm as the cleaning proceeds. After at least 10 minutes of acetone cleaning, a fourth beaker of isopropyl alcohol is placed in the cleaner and the specimens are moved from the acetone to the alcohol. For similar reasons, the isopropyl alcohol is not warmed before starting the final cleaning step. After a minimum of 10 minutes of cleaning in the isopropyl alcohol, the specimens are placed on a lint-free cloth and dried with compressed air or nitrogen. Specimens that have gone through the cleaning process are shown in Figures 2-13a and 2-13b.

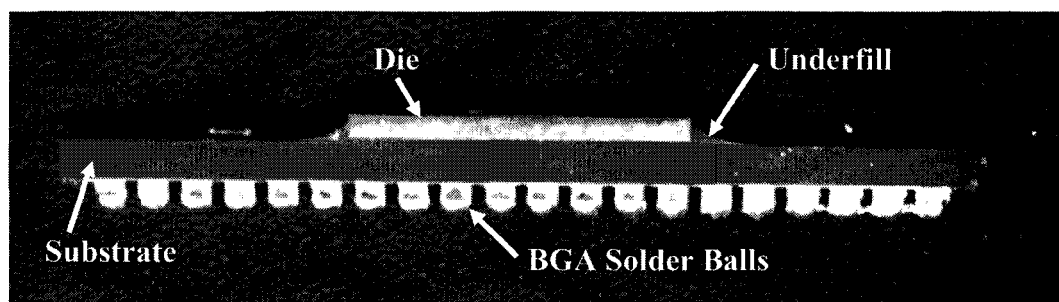


Figure 2-13a: *Final specimen cross-section with BGA solder balls.*

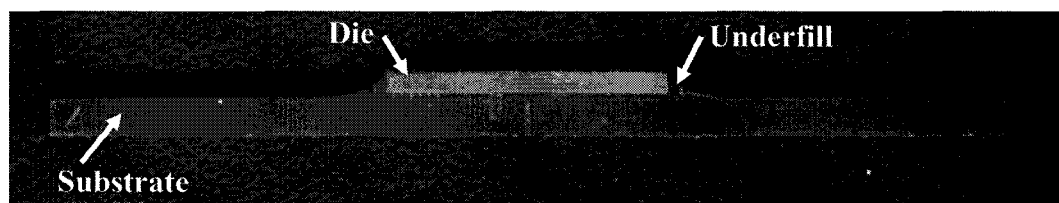


Figure 2-13b: *Final specimen with BGA solder balls removed and fillets scribed.*

2.1.6. REFERENCE POINTS

In order to monitor and measure displacements around the crack tip, reference marks may be required around the crack tip. For the final study, reference points were unnecessary, but the technique developed is unique enough to warrant preservation. The use of reference points requires that the crack introduction be complete and a means of marking the crack tip location available because the technique developed masks the underlying structure, making location of the interface difficult.

The reference marks on the specimen are created by using a transmission electron microscope (TEM) support grid, an example of which is shown in Figure 2-14. A TEM grid is a circular fine mesh of wires 3 mm in diameter constructed of copper, nickel, or gold/palladium. The network of wires with a thickness ranging between 5 and 20 microns has relatively larger open spaces between them. The TEM grid is placed flat on the specimen ahead of the crack tip and a drop of a sucrose solution is applied over the grid. Pressure is applied to the edges of the grid to hold it flat over the surface while the solution dries. When dry, the TEM grid is removed and a negative image of the grid itself is formed, thereby creating the reference marks, as shown in Figure 2-15. The hardened sucrose solution does not add any appreciable strength to the specimen. Preliminary tests using this method showed uniform displacement patterns. One concern of this method was how accurately the displacements of the reference points reflected the movement of the underlying material. Further investigation was not performed since reference points were unnecessary for this study. Another concept of using the TEM grid

as a mask to generate reference points using a sputterer was generated but would require the creation of a high-tension jig to hold the grid perfectly flat against the specimen. Again, this was not investigated further as it was not needed, but the sputter technique would more accurately model the specimen behavior because it removes the possibility of shear lag in the material creating the reference points.

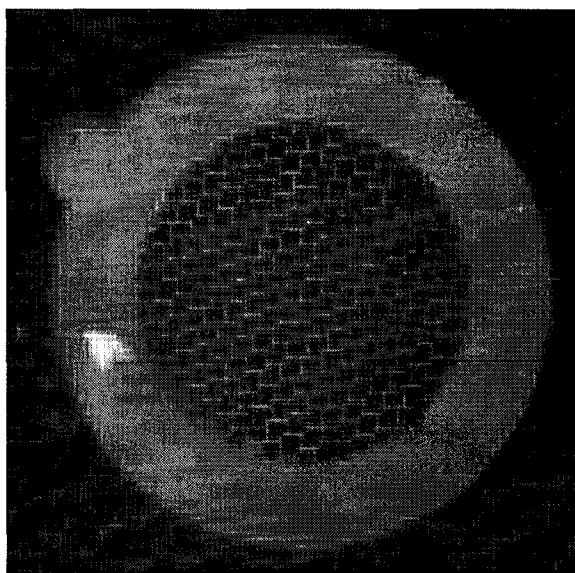


Figure 2-14: *TEM support grid used to create reference marks.*

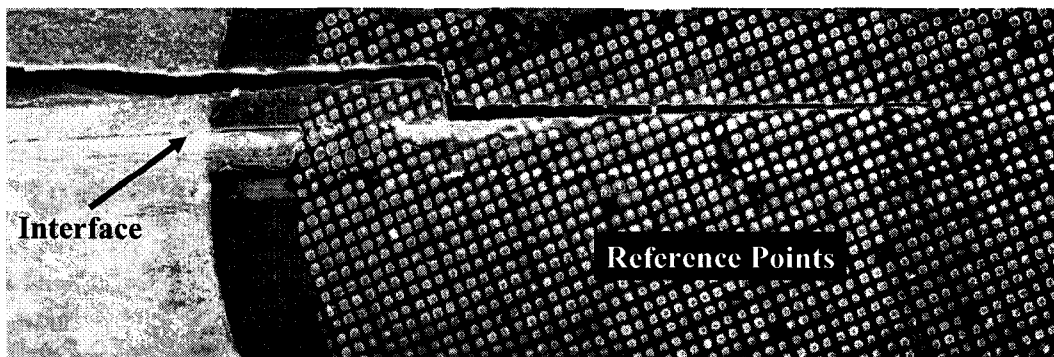


Figure 2-15: *SEM image of underfill crack in a region marked with reference points.*

2.1.7. SPUTTERING

The final step in the specimen preparation procedure is a thin metal sputtering to allow for the imaging of the specimen in the SEM. This step is necessary because non-conductive materials accumulate charge as the electron beam strikes them during normal SEM imaging. This charge build up creates two problems: image distortion and arcing. As the charge builds on the specimen, the electric field in the region of the charge begins to deflect the incoming electron beam, giving the appearance in the image that the return signal came from a different location, creating distortion and image artifacts. As the charge builds, the return signal increases in intensity, creating a bright spot on the image that loses all details and also masks the regions near the charged area. When the charge becomes sufficiently high, the charge arcs from the non-conductive location to a conductive material, which can damage equipment. Applying a thin conductive coat by sputtering the specimen removes these problems. Because the thickness of the film is on the nanometer scale, no appreciable strength is added to the specimen. Also, the thin film is transparent to the electron microscope, allowing for the underlying structures to be easily imaged.

2.2. Testing Procedure

The testing of the prepared specimens is performed in a modified SEM and image acquisition system. The specimen is placed in a bending stage custom made for the SEM. Load is applied to the sample and images are captured on a PC using software to

control the SEM system. After the testing is complete, the images are processed using digital imaging software to determine the displacements that occurred during the test run.

2.2.1. EQUIPMENT

Towards the completion of the study, the SEM chamber has been modified to include a bend test fixture. The loading stage also incorporates temperature control of the load points if thermal loading is desired. The SEM has a digital imaging system to store images on a PC for image correlation analysis after the testing is complete. The custom bending stage, shown in Figures 2-16a-c, was made by Oxford/Gatan, includes displacement and temperature control. The temperature is reduced by the introduction of super-cooled dry nitrogen gas to cool the load application anvils. Similarly, the temperature is increased by turning on resistance heaters in the anvils. The temperature is controlled using a dedicated control box connected to the stage with cables. Since the SEM chamber is at a high vacuum, the temperature control must be applied to the anvils of the bending fixture. Thus, the specimen can only experience temperature cycling by conduction from the anvils. If the portion of the specimen in contact with the anvils is a poor heat conductor, cycling is slow or not possible. In this study only the substrate is in contact with the anvils. Because of the low thermal conductivity of the substrate, thermal cycling is not feasible on these samples and the temperature cycling feature is not used during this study.



Figure 2-16a: *Custom SEM stage with bending fixture and thermal control.*

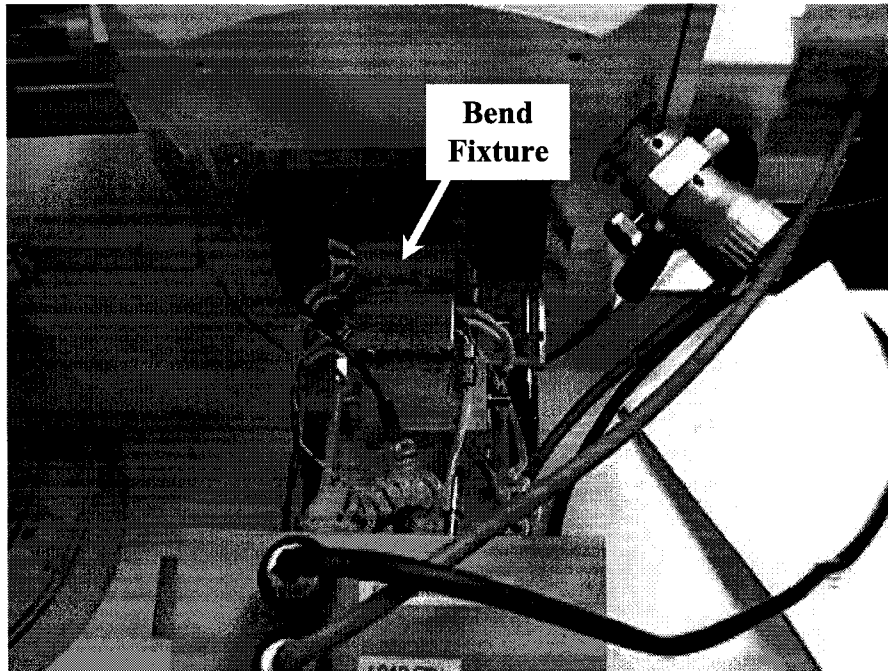


Figure 2-16b: Stage with three-point bend fixture installed.

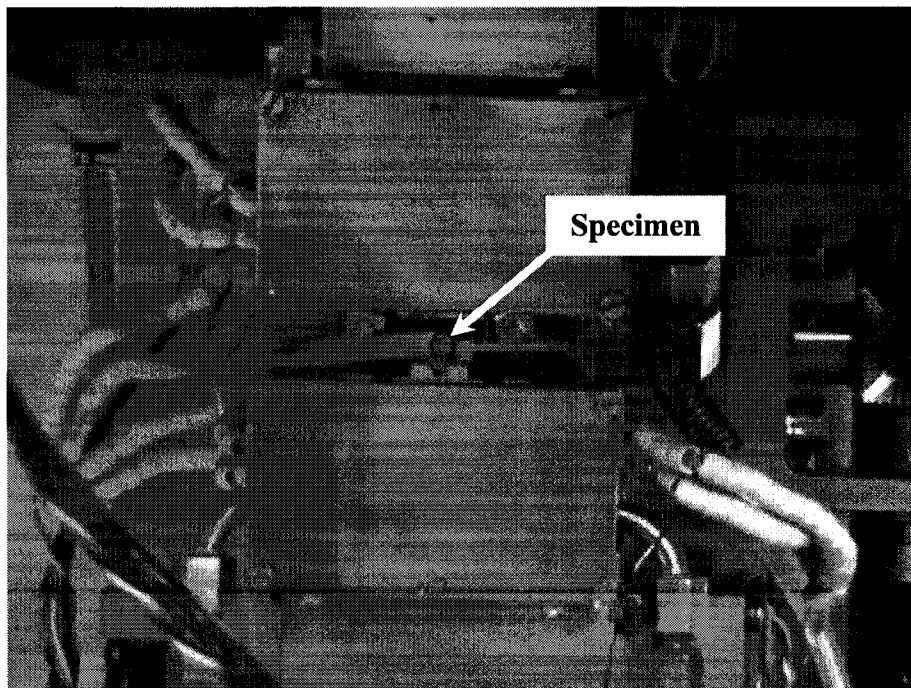


Figure 2-16c: Specimen marked with reference points in three-point bend fixture.

The stage also allows for movement in the horizontal plane of the entire three-point bending test fixture but does not allow for the specimen tilt normally found in SEM stages. This prevents the specimen from being viewed at an angle other than top-down, thereby removing the possible effects of perspective foreshortening. The rotation of the specimen about the vertical (Z) axis common with most SEM stages is also not available. This is due to the connections required to apply the temperature cycling and also the displacement loading of bending test fixture. This eliminates the possibility of aligning the interface along the vertical or horizontal axis but this was not found to be a problem during the testing.

2.2.2. LOAD APPLICATION

The displacement of the anvils in the bending test fixture is achieved by a second controller (Figure 2-17) which can either increase or decrease the distance between the loading points. The speed at which the loading is applied can also be controlled using this unit. If the control is not satisfactory, the loading displacement can be applied manually by means of a knob on the stage itself. The load resulting from the displacement application is read from a transducer in the bend fixture grips and displayed on the displacement controller. This permits the application of displacement load until a desired load value is achieved.

The three-point bend fixture used a standard configuration while the four-point bending anvils used for load application were modified from the standard locations. The inner

load points were moved outward to allow a majority of the die to lie within these points. This was to create a larger working zone for testing due to difficulties in driving the crack as it nears the inner load point locations. Once the crack reaches the loading points, failure occurs down into the sample instead of along the interface.

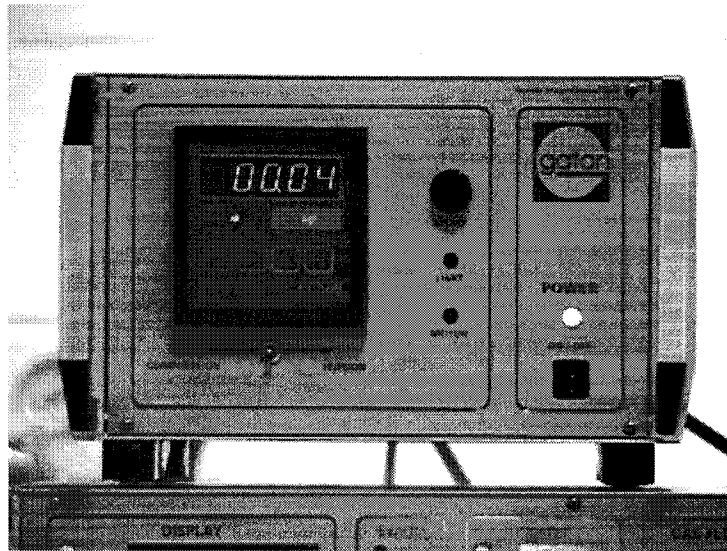


Figure 2-17: *Displacement control and load readout for SEM loading stage.*

2.2.3. IMAGE ACQUISITION

After the bending stage is placed in the chamber, a reference image is captured by means of a ThermoNORAN Level 2 Kevex Sigma System (image capture and analysis hardware/software package) running on a Windows-based PC. An increment of loading is then applied up to a desired load level and the test is paused while another image is captured and saved on the PC. The test is resumed by incrementally increasing the load and capturing the corresponding image until the crack propagates along the interface. All images are stored in a proprietary format and must be converted to bitmaps to allow access by other software. The image capture software also records the distance between

pixels when the image is captured allowing the absolute distances to be determined from the images.

2.2.4. IMAGE ANALYSIS BY DIGITAL IMAGE CORRELATION

The images collected during the testing are analyzed by digital image correlation (DIC) to determine the displacements that occur during the test. The theory behind DIC starts with the selection of a point of interest (POI) on the first (reference) image. The pixels adjacent to the POI are then selected to generate a sub-image near the POI. This sub-image is compared to points on the second (object) image and a correlation calculated. When the region on the object image that corresponds to the same region on the reference image is matched exactly, a perfect correlation is found; if the images do not match at all, then no correlation is found. When the best correlation is found on the object image, coordinates of the correlation point are compared to the coordinates of the POI to determine how far the point moved between images. This process is depicted graphically in Figure 2-18.

The digital image correlation was performed by using a commercially available software package: winDAC from the Fraunhofer Institute in Germany. The software is capable of determining displacements and strains from two input images. The frequency of the data points is determined by a mesh generated in the code or in an external finite element analysis program. Correlation calculations are performed at each nodal point of the mesh.

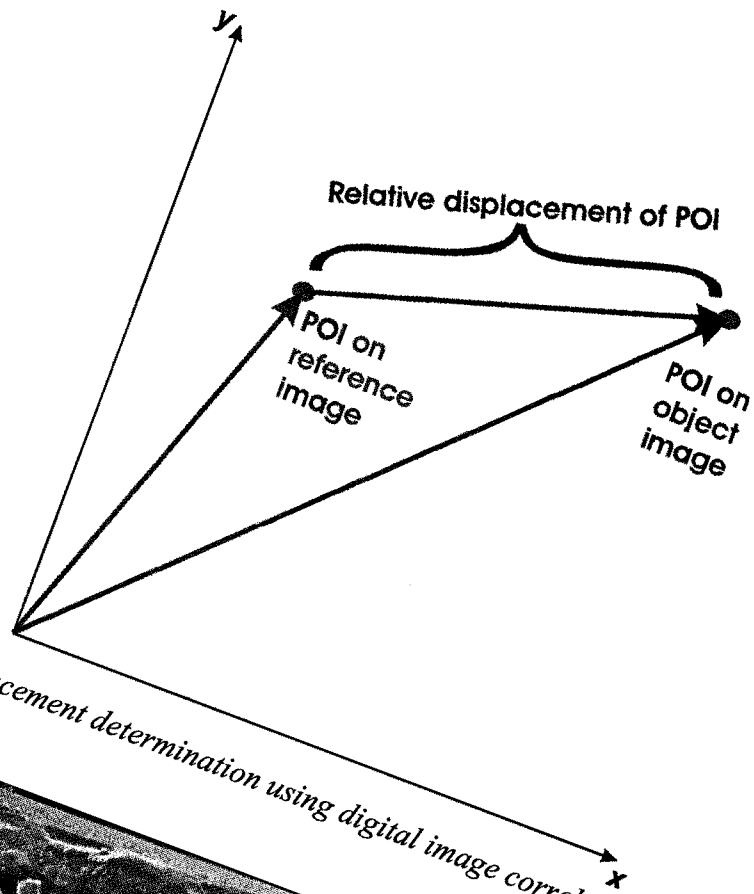


Figure 2-18: Displacement determination using digital image correlation.

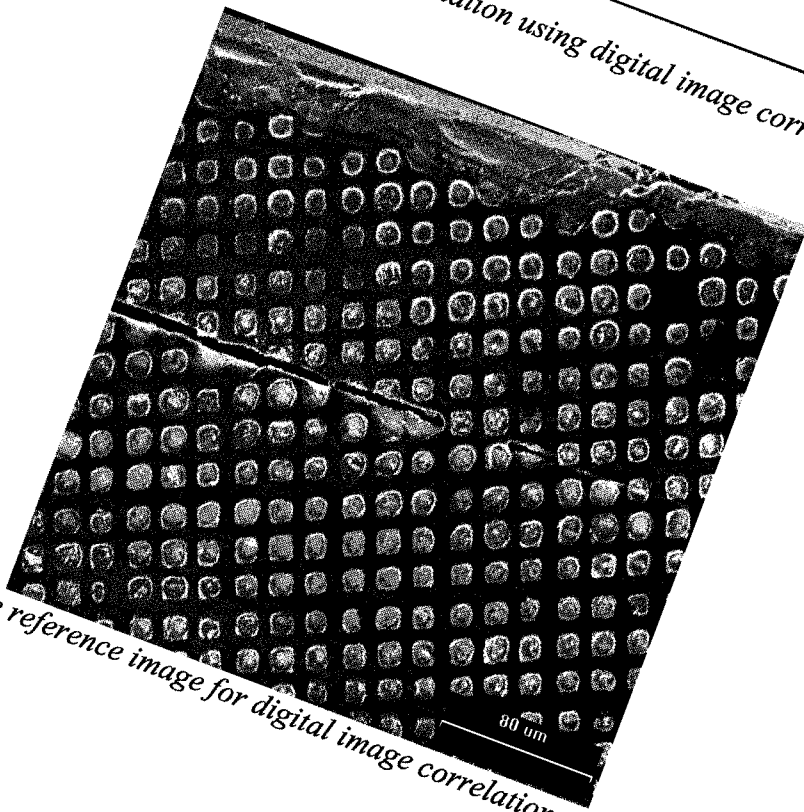


Figure 2-19: Sample reference image for digital image correlation.

The procedure used for software based digital image correlation is to enter the reference and object images into the workspace. A sample image is shown in Figure 2-19. A mesh is generated over the reference image to create the nodal points that correspond to the points of interest where the displacements are to be found. After performing the correlation process, displacements and strains are returned in ASCII text format, allowing the data to be used in a variety of software applications. The undeformed (black) and deformed (white) meshes are depicted in Figure 2-20 and the vector field results are shown in Figure 2-21.

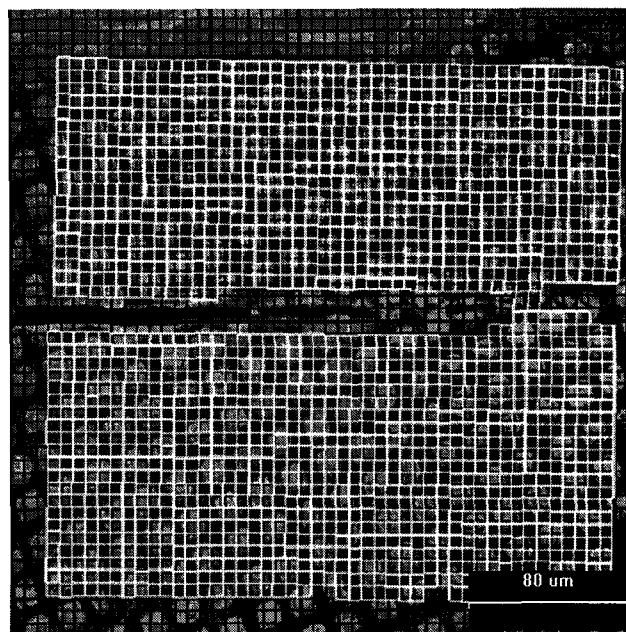


Figure 2-20: *Undeformed and deformed meshes from digital image correlation.*

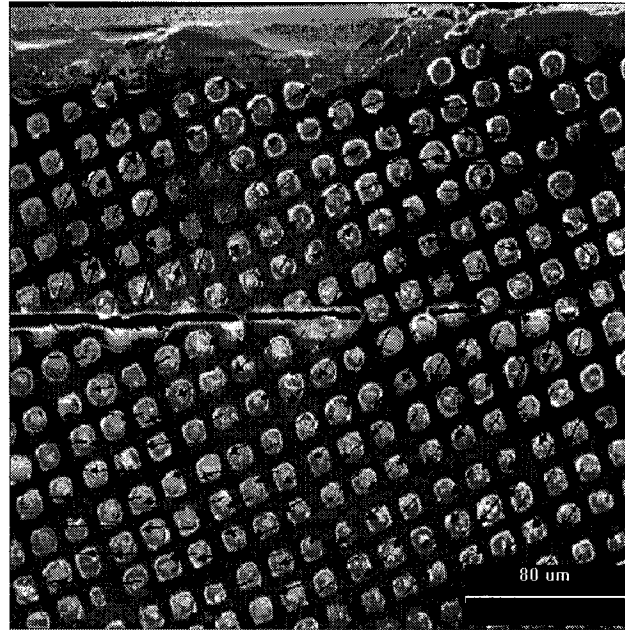


Figure 2-21: *Vector field representation of displacements from digital image correlation (displacement vectors not to scale).*

2.3. Summation

Multiple techniques were developed to section electronic packages. Encapsulation is necessary to prevent severe damage to the die during sectioning. For the samples tested in this dissertation, an epoxy support matrix is used. This matrix is then removed with epoxy dissolver following sectioning. Alternate techniques developed but not used were Methyl Methacrylate / Butyl Methacrylate (MBM) encapsulation, which can be removed with acetone, and encapsulation after a Con-Tact paper covering is placed over the package. The Con-Tact paper is thermoformed prior to encapsulation to remove all air pockets near the die.

Encapsulation is performed in a disposable mold cup. Plastic stand-off clips are placed around the package to allow epoxy to flow underneath the specimen. For larger samples, a custom mold fixture was fabricated of aluminum and ultra-high molecular weight polyethylene (UHMW-PE). The custom mold fixture was not needed for the samples tested in this dissertation. A low speed sectioning saw with a diamond wafering blade is used to section the encapsulated packages. The original saw grip was replaced with a custom machined fixture to ensure the stability of the piece during sectioning.

Two methods were developed for the introduction of the interfacial crack into the sample sections. The first method, end cracking, is to create a notch on the underfill fillet which is driven into the interface by means of a bending load. This method had limited success and was replaced by the center cracking method. Center cracking has two variations: scribing and notching. For scribing, a glass cutter is used to create a fine scratch on the top surface of the die which is propagated down to the interface using a three point bend fixture. Notching requires a second cut into the die to create a site of crack initiation close to the interface. Both center cracking methods were used in this dissertation with the notching method giving better results.

Following the crack introduction, the samples are cleaned using a four step ultrasonic cleaning to remove any residue from encapsulation and also any debris from sectioning and cracking. The final step of sample preparation is the application of a metal sputter coat. This allows the non-conductive regions of the specimen to be imaged in the SEM.

3. ANALYTICAL STRESS ANALYSIS

This chapter presents the second task in this study: the development of an analytical model. This model consists of a finite region that encompasses the crack tip as well as portions of the crack faces and the interface. Within the region, the solution for the stress field is known exactly, but has unknown coefficients. Given the boundary displacements obtained from the experimental work, these coefficients can be determined, allowing the stress field within the region to be solved. Using the stress field information, the stress intensity factors K_I and K_{II} for opening and shearing modes, respectively, can be found. However, the stress intensity factors are dependent on loading conditions, length scale, and other factors, so the interfacial strength is reported using the energy release rate, G , which does not have these limitations. The critical value, G_c , is the energy release rate calculated from the experimental data acquired just prior to crack propagation.

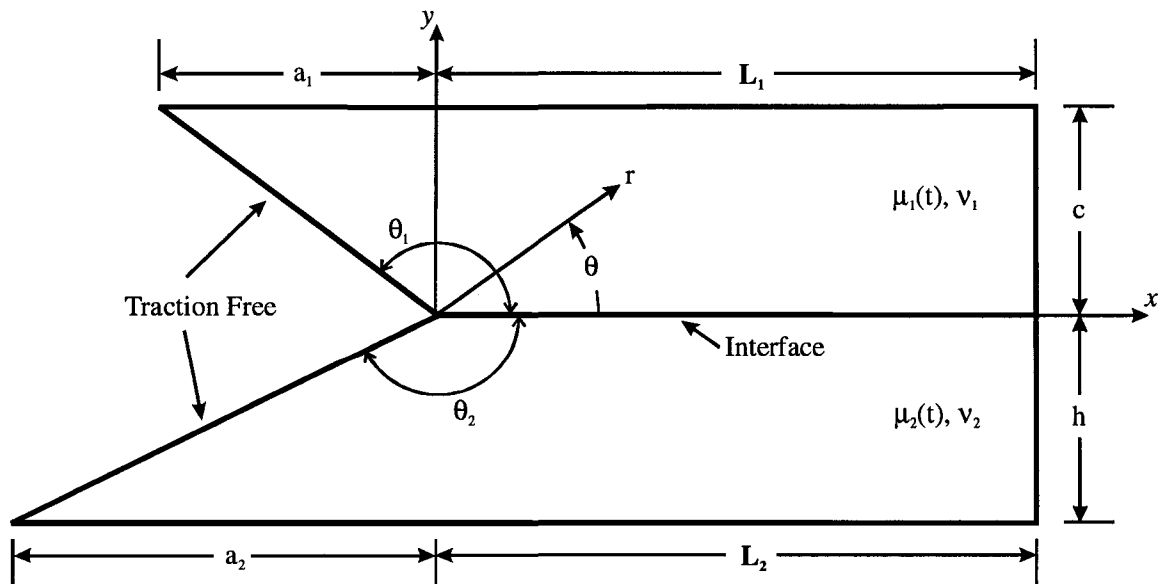


Figure 3-1: Geometry of a finite domain of two dissimilar viscoelastic materials.

3.1. Problem Statement

A finite domain of two dissimilar material sectors, illustrated in Figure 3-1, is considered under general loading conditions. Each sector of the domain represents a viscoelastic, homogeneous, and isotropic material with shear modulus, $\mu_k(t)$, and Poisson's ratio, ν_k , with $k=1,2$. The Poisson's ratios are independent of time. The shear modulus is described by

$$\mu_k(t) = \mu_k^\infty + (\mu_k^0 - \mu_k^\infty)e^{-t/\tau_k} \quad (3-1)$$

in which τ_k is the relaxation time. The parameters μ_k^0 and μ_k^∞ are positive constants representing the shear modulus at $t=0$ and $t=\infty$, respectively. The material sectors are defined by the angle θ_k and the interface has zero thickness with perfect bonding. The origin of the polar coordinate system (r, θ) coincides with the junction.

As shown in Figure 3-2, along the interface, the radial boundaries of the k^{th} sector and their unit normal vectors are denoted by $\bar{\Gamma}_k$, $\bar{\mathbf{n}}^{(k)}$ and $\tilde{\Gamma}_k$, $\tilde{\mathbf{n}}^{(k)}$, respectively. The circumferential segment of the boundary associated with the k^{th} material sector is denoted by Γ_k , and its unit normal to the boundary is $\mathbf{n}^{(k)}$. The radial boundaries defined by $\bar{\Gamma}_1$ and $\tilde{\Gamma}_2$ are traction free. The circumferential segments of the boundary defined by Γ_1 and Γ_2 can be subject to external displacement constraints and tractions. Along the interface, the displacement and traction components are continuous due to perfect bonding.

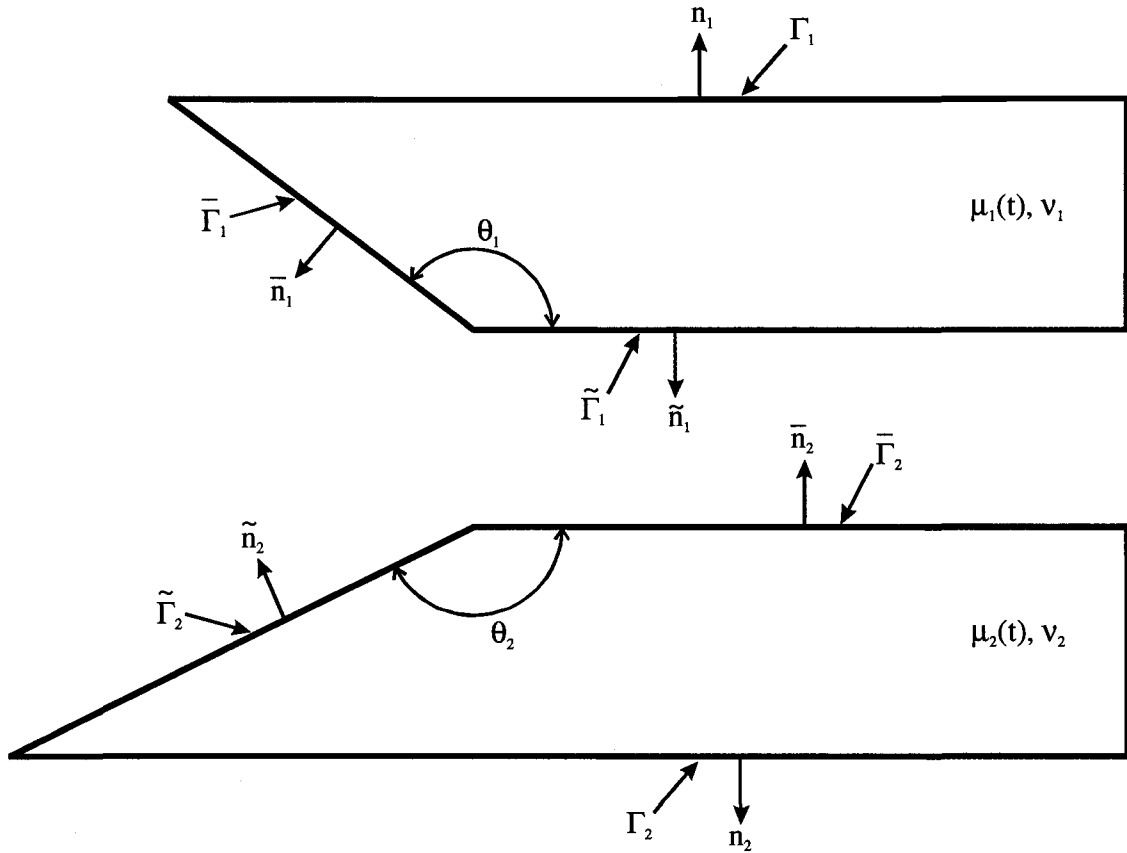


Figure 3-2: Boundary segments and their unit normals

Each sector of material is governed by the two-dimensional and time dependent stress equilibrium equations in polar coordinates given by

$$\sigma_{rr,r}^{(k)}(t) + \frac{1}{r} \sigma_{r\theta,\theta}^{(k)}(t) + \frac{1}{r} (\sigma_{rr}^{(k)}(t) - \sigma_{\theta\theta}^{(k)}(t)) = 0$$

$$\sigma_{r\theta,r}^{(k)}(t) + \frac{1}{r} \sigma_{\theta\theta,\theta}^{(k)}(t) + \frac{2}{r} \sigma_{r\theta}^{(k)}(t) = 0 \quad (3-2)$$

The compatibility condition in terms of the stress components is

$$\left(\frac{\partial^2}{\partial r^2} + \frac{1}{r} \frac{\partial}{\partial r} + \frac{1}{r^2} \frac{\partial^2}{\partial \theta^2} \right) (\sigma_{rr}^{(k)}(t) + \sigma_{\theta\theta}^{(k)}(t)) = 0 \quad (3-3)$$

Under plane strain assumptions, the stress-strain relations for a linear viscoelastic material are given by

$$\sigma_{\alpha\beta}^{(k)}(t) = \int_{-\infty}^t \left\{ K_k(t-\tau) \frac{\partial \varepsilon_{\gamma\gamma}^{(k)}(\tau)}{\partial \tau} \delta_{\alpha\beta} + 2\mu_k(t-\tau) \left(\frac{\partial \varepsilon_{\alpha\beta}^{(k)}(\tau)}{\partial \tau} - \frac{1}{2} \frac{\partial \varepsilon_{\gamma\gamma}^{(k)}(\tau)}{\partial \tau} \delta_{\alpha\beta} \right) \right\} d\tau \quad (3-4)$$

with $\alpha, \beta, \gamma = r, \theta$

in which the bulk modulus $K_k(t)$ is related to the shear $\mu_k(t)$ modulus by

$$K_k(t) = \frac{\mu_k(t)}{(1-2\nu_k)} \quad (3-5)$$

The problem posed is to determine the strength of the singular stress field and its intensification near the junction of dissimilar viscoelastic materials of a finite region under general loading conditions. The solution to this problem permits the examination of the effect of the relaxation parameters, geometry, and difference in shear moduli on the stress intensification and its singular behavior.

3.2. Solution Method

In order to eliminate the time dependency in the governing equations, the stress, $\sigma_{\alpha\beta}^{(k)}$, strain, $\varepsilon_{\alpha\beta}^{(k)}$, and displacement, $u_{\alpha}^{(k)}$, components are defined in the Laplace domain as

$$\hat{\sigma}_{\alpha\beta}^{(k)}(r, \theta; s) = \int_0^{\infty} \sigma_{\alpha\beta}^{(k)}(r, \theta; t) e^{-st} dt$$

$$\hat{\varepsilon}_{\alpha\beta}^{(k)}(r, \theta; s) = \int_0^{\infty} \varepsilon_{\alpha\beta}^{(k)}(r, \theta; t) e^{-st} dt$$

$$\hat{u}_{\alpha\beta}^{(k)}(r, \theta; s) = \int_0^{\infty} u_{\alpha\beta}^{(k)}(r, \theta; t) e^{-st} dt \quad (3-6)$$

with $\alpha, \beta = r, \theta$. Applying the Laplace transformation to the two-dimensional equilibrium, compatibility and constitutive equations of viscoelasticity results in

$$\begin{aligned} \hat{\sigma}_{rr,r} + \frac{1}{r} \hat{\sigma}_{r\theta,\theta} + \frac{1}{r} (\hat{\sigma}_{rr} - \hat{\sigma}_{\theta\theta}) &= 0 \\ \hat{\sigma}_{r\theta,r} + \frac{1}{r} \hat{\sigma}_{\theta\theta,\theta} + \frac{2}{r} \hat{\sigma}_{r\theta} &= 0 \\ \left(\frac{\partial^2}{\partial r^2} + \frac{1}{r} \frac{\partial}{\partial r} + \frac{1}{r^2} \frac{\partial^2}{\partial \theta^2} \right) (\hat{\sigma}_{rr} + \hat{\sigma}_{\theta\theta}) &= 0 \\ \hat{\sigma}_{\alpha\beta}^{(k)} = s \hat{K}_k \hat{\varepsilon}_{\gamma\gamma}^{(k)} \delta_{\alpha\beta} + 2s \hat{\mu}_k \left(\hat{\varepsilon}_{\alpha\beta}^{(k)} - \frac{1}{2} \hat{\varepsilon}_{\gamma\gamma}^{(k)} \delta_{\alpha\beta} \right) & \quad (3-7) \end{aligned}$$

with $\alpha, \beta, \gamma = r, \theta$

The shear, $\mu_k(t)$, and bulk, $K_k(t)$, moduli in the Laplace domain become

$$\hat{\mu}_k(s) = \int_0^{\infty} \mu_k(t) e^{-st} dt \quad \text{and} \quad \hat{K}_k(s) = \int_0^{\infty} K_k(t) e^{-st} dt \quad (3-8)$$

For time independent Poisson's ratio and under plane strain assumptions, these moduli are related by

$$\hat{K}_k(s) = \frac{\hat{\mu}_k(s)}{(1 - 2\nu_k)} \quad (3-9)$$

Thus, the constitutive relations take the form

$$\hat{\varepsilon}_{\alpha\beta}^{(k)} = \frac{1}{2s\hat{\mu}_k} (\hat{\sigma}_{\alpha\beta}^{(k)} - \nu_k \hat{\sigma}_{\gamma\gamma}^{(k)} \delta_{\alpha\beta}) \quad (3-10)$$

Based on the solution form suggested by Williams (1952), the stress and displacement components in the Laplace domain for the k^{th} material sector can be represented in the form

$$\begin{aligned}\hat{\sigma}_{\alpha\beta}^{(k)}(r, \theta; s) &= \sum_{n=0}^{\infty} r^{\lambda_n} \hat{F}_{\alpha\beta}^{(k)}(\theta; s, \lambda_n) \\ \hat{u}_{\alpha}^{(k)}(r, \theta; s) &= \sum_{n=0}^{\infty} r^{\lambda_n+1} \hat{G}_{\alpha}^{(k)}(\theta; s, \lambda_n)\end{aligned}\quad (3-11)$$

with $\alpha, \beta = r, \theta$ ($k = 1, 2$), $\lambda_0 = 0$, and $\lambda_n \neq 0$ for $n = 1, 2, \dots, N$ being unknown parameters.

Under plane strain conditions, the non-dimensional functions $\hat{F}_{\alpha\beta}^{(k)}(\theta; s, \lambda_n)$ and $\hat{G}_{\alpha}^{(k)}(\theta; s, \lambda_n)$ satisfying the equilibrium and compatibility equations can be expressed as

$$\begin{aligned}\hat{F}_{rr}^{(k)}(\theta; s, \lambda_n) &= \frac{(2 - \lambda_n)}{4} \left[\hat{A}_n^{(k)} \cos \lambda_n \theta + \hat{B}_n^{(k)} \sin \lambda_n \theta \right] - \left[\hat{C}_n^{(k)} \cos(\lambda_n + 2)\theta + \hat{D}_n^{(k)} \sin(\lambda_n + 2)\theta \right] \\ \hat{F}_{\theta\theta}^{(k)}(\theta; s, \lambda_n) &= \frac{(2 + \lambda_n)}{4} \left[\hat{A}_n^{(k)} \cos \lambda_n \theta + \hat{B}_n^{(k)} \sin \lambda_n \theta \right] + \left[\hat{C}_n^{(k)} \cos(\lambda_n + 2)\theta + \hat{D}_n^{(k)} \sin(\lambda_n + 2)\theta \right] \\ \hat{F}_{r\theta}^{(k)}(\theta; s, \lambda_n) &= \frac{\lambda_n}{4} \left[\hat{A}_n^{(k)} \sin \lambda_n \theta - \hat{B}_n^{(k)} \cos \lambda_n \theta \right] + \left[\hat{C}_n^{(k)} \sin(\lambda_n + 2)\theta - \hat{D}_n^{(k)} \cos(\lambda_n + 2)\theta \right] \\ \hat{G}_r^{(k)}(\theta; s, \lambda_n) &= \frac{1}{(\lambda_n + 1)} \left\{ \frac{4(1 - \nu_k) - (2 + \lambda_n)}{8s\hat{\mu}_k} \left[\hat{A}_n^{(k)} \cos \lambda_n \theta + \hat{B}_n^{(k)} \sin \lambda_n \theta \right] \right. \\ &\quad \left. - \frac{1}{2s\hat{\mu}_k} \left[\hat{C}_n^{(k)} \cos(\lambda_n + 2)\theta + \hat{D}_n^{(k)} \sin(\lambda_n + 2)\theta \right] \right\} \\ \hat{G}_{\theta}^{(k)}(\theta; s, \lambda_n) &= \frac{1}{(\lambda_n + 1)} \left\{ \frac{4(1 - \nu_k) + \lambda_n}{8s\hat{\mu}_k} \left[\hat{A}_n^{(k)} \sin \lambda_n \theta - \hat{B}_n^{(k)} \cos \lambda_n \theta \right] \right. \\ &\quad \left. + \frac{1}{2s\hat{\mu}_k} \left[\hat{C}_n^{(k)} \sin(\lambda_n + 2)\theta - \hat{D}_n^{(k)} \cos(\lambda_n + 2)\theta \right] \right\}\end{aligned}\quad (3-12)$$

in which $\hat{A}_n^{(k)}(s)$, $\hat{B}_n^{(k)}(s)$, $\hat{C}_n^{(k)}(s)$, and $\hat{D}_n^{(k)}(s)$ are the unknown coefficients associated with the k^{th} sector.

Prior to enforcing the continuity equations and boundary conditions, a combination of these functions is recast as

$$\hat{\mathbf{p}}_n^{(k)}(\theta; s, \lambda_n) = \hat{\mathbf{P}}_n^{(k)}(\theta; s, \lambda_n) \hat{\mathbf{q}}_n^{(k)}(s) ; n = 0, 1, \dots, N \quad (3-13)$$

and

$$\hat{\mathbf{t}}_n^{(k)}(\theta; s, \lambda_n) = \hat{\mathbf{T}}_n^{(k)}(\theta; s, \lambda_n) \hat{\mathbf{q}}_n^{(k)}(s) ; n = 0, 1, \dots, N \quad (3-14)$$

in which the vectors $\hat{\mathbf{p}}_n^{(k)}$, $\hat{\mathbf{t}}_n^{(k)}$ and $\hat{\mathbf{q}}_n^{(k)}$ are defined by

$$\begin{aligned} \hat{\mathbf{p}}_n^{(k)T} &= \left\{ \hat{F}_{\theta\theta}^{(k)}(\theta; s, \lambda_n), \hat{F}_{r\theta}^{(k)}(\theta; s, \lambda_n), \hat{G}_r^{(k)}(\theta; s, \lambda_n), \hat{G}_\theta^{(k)}(\theta; s, \lambda_n) \right\} \\ \hat{\mathbf{t}}_n^{(k)T} &= \left\{ \hat{F}_{\theta\theta}^{(k)}(\theta; s, \lambda_n), \hat{F}_{r\theta}^{(k)}(\theta; s, \lambda_n) \right\} \\ \hat{\mathbf{q}}_n^{(k)T} &= \left\{ \hat{A}_n^{(k)}, \hat{B}_n^{(k)}, \hat{C}_n^{(k)}, \hat{D}_n^{(k)} \right\} \end{aligned} \quad (3-15)$$

The matrices $\mathbf{P}_n^{(k)}$ and $\mathbf{T}_n^{(k)}$ are given by

$$\hat{\mathbf{P}}_n^{(k)}(\theta; s, \lambda_n) = \begin{bmatrix} \frac{2 + \lambda_n}{4} \cos \lambda_n \theta & \frac{2 + \lambda_n}{4} \sin \lambda_n \theta & \cos(\lambda_n + 2)\theta & \sin(\lambda_n + 2)\theta \\ \frac{\lambda_n}{4} \sin \lambda_n \theta & -\frac{\lambda_n}{4} \cos \lambda_n \theta & \sin(\lambda_n + 2)\theta & -\cos(\lambda_n + 2)\theta \\ \frac{4(1 - \nu_k) - (2 + \lambda_n)}{8s\hat{\mu}_k(\lambda_n + 1)} \cos \lambda_n \theta & \frac{4(1 - \nu_k) - (2 + \lambda_n)}{8s\hat{\mu}_k(\lambda_n + 1)} \sin \lambda_n \theta & -\frac{1}{2s\hat{\mu}_k(\lambda_n + 1)} \cos(\lambda_n + 2)\theta & -\frac{1}{2s\hat{\mu}_k(\lambda_n + 1)} \sin(\lambda_n + 2)\theta \\ \frac{4(1 - \nu_k) + \lambda_n}{8s\hat{\mu}_k(\lambda_n + 1)} \sin \lambda_n \theta & -\frac{4(1 - \nu_k) + \lambda_n}{8s\hat{\mu}_k(\lambda_n + 1)} \cos \lambda_n \theta & \frac{1}{2s\hat{\mu}_k(\lambda_n + 1)} \sin(\lambda_n + 2)\theta & -\frac{1}{2s\hat{\mu}_k(\lambda_n + 1)} \cos(\lambda_n + 2)\theta \end{bmatrix}$$

and

$$\hat{\mathbf{T}}_n^{(k)}(\theta; s, \lambda_n) = \begin{bmatrix} \frac{2 + \lambda_n}{4} \cos \lambda_n \theta & \frac{2 + \lambda_n}{4} \sin \lambda_n \theta & \cos(\lambda_n + 2)\theta & \sin(\lambda_n + 2)\theta \\ \frac{\lambda_n}{4} \sin \lambda_n \theta & -\frac{\lambda_n}{4} \cos \lambda_n \theta & \sin(\lambda_n + 2)\theta & -\cos(\lambda_n + 2)\theta \end{bmatrix} \quad (3-16)$$

The traction-free boundary conditions and the continuity conditions between the adjacent sectors are given by

$$\begin{aligned} \hat{\mathbf{t}}_n^{(1)}(\theta_1; s, \lambda_n) &= \hat{\mathbf{t}}_n^{(2)}(\theta_2; s, \lambda_n) = \mathbf{0} \\ \hat{\mathbf{p}}_n^{(1)}(0; s, \lambda_n) - \hat{\mathbf{p}}_n^{(2)}(0; s, \lambda_n) &= \mathbf{0} \end{aligned} \quad (3-17)$$

with $n = 1, \dots, N$. Enforcing these conditions leads to a homogeneous system of equations in the form

$$\hat{\mathbf{Q}}(\theta; s, \lambda_n) \hat{\mathbf{q}}_n = \mathbf{0} \quad (3-18)$$

The vector of unknown coefficients $\hat{\mathbf{q}}_n$ are defined by

$$\hat{\mathbf{q}}_n^T = \left\{ \hat{\mathbf{q}}_n^{(1)T}, \hat{\mathbf{q}}_n^{(2)T} \right\} \quad (3-19)$$

The coefficient matrices, $\hat{\mathbf{Q}}(\theta; s, \lambda_n)$, associated with the homogeneous system of equations are defined by

$$\hat{\mathbf{Q}} = \begin{bmatrix} \hat{\mathbf{T}}_n^{(1)}(\theta_1; s, \lambda_n) & \mathbf{0} \\ \hat{\mathbf{P}}_n^{(1)}(0; s, \lambda_n) & -\hat{\mathbf{P}}_n^{(2)}(0; s, \lambda_n) \\ \mathbf{0} & \hat{\mathbf{T}}_n^{(2)}(\theta_2; s, \lambda_n) \end{bmatrix} \quad (3-20)$$

A non-trivial solution to the homogeneous system exists for values of λ_n that cause the determinant of the coefficient matrix $\hat{\mathbf{Q}}(\theta; s, \lambda_n)$ to vanish. They may be complex, depending on the properties of the material sectors. These particular values of λ_n are the roots of the characteristic equation

$$\begin{aligned} & \hat{M}_1(s)R_{11}(\lambda_n) + \hat{M}_2(s)R_{12}(\lambda_n) + \hat{M}_3(s)R_{12}(\lambda_n)R_{21}(\lambda_n) \\ & + \hat{M}_4(s)R_{11}(\lambda_n)R_{22}(\lambda_n) - \hat{M}_5(s)R_{11}(\lambda_n)R_{12}(\lambda_n) - \hat{M}_6(s)R^*(\lambda_n) = 0 \end{aligned} \quad (3-21)$$

where \hat{M}_i with $i=1,6$, dependent only on the material properties and Laplace transform variable, are defined as

$$\begin{aligned} \hat{M}_1 &= \frac{16(1-\nu_1)^2}{s}; \quad \hat{M}_2 = \frac{16(1-\nu_2)^2}{s} \frac{\hat{\rho}_1^2}{\hat{\rho}_2^2}; \quad \hat{M}_3 = \frac{8(1-\nu_1)}{s} \left(1 - \frac{\hat{\rho}_1}{\hat{\rho}_2}\right); \\ \hat{M}_4 &= \frac{8(1-\nu_2)}{s} \left(\frac{\hat{\rho}_1^2}{\hat{\rho}_2^2} - \frac{\hat{\rho}_1}{\hat{\rho}_2}\right); \quad \hat{M}_5 = \frac{1}{s} \left(1 - \frac{\hat{\rho}_1}{\hat{\rho}_2}\right)^2; \quad \hat{M}_6 = \frac{32(1-\nu_1)(1-\nu_2)}{s} \frac{\hat{\rho}_1}{\hat{\rho}_2} \end{aligned} \quad (3-22)$$

The functions, R_{ji} with $i, j=1,2$, independent of Laplace transformation variable, involve the angles of the material sectors, θ_i , and the unknown parameter λ_n as

$$\begin{aligned} R_{1i} &= 2 \left[\lambda_n (\lambda_n + 2) (1 - \cos(2\theta_i)) - 2 \sin(\lambda_n \theta_i) \sin((\lambda_n + 2)\theta_i) \right] \\ R_{2i} &= -1 - \cos(2\theta_i) \left(1 - 2 \cos^2[(\lambda_n + 2)\theta_i]\right) + 2 \cos[(\lambda_n + 2)\theta_i] \sin[(\lambda_n + 2)\theta_i] \sin(2\theta_i) \\ R^* &= G_{12} + G_{21} + H_1 + H_2 + H_3 \end{aligned} \quad (3-23)$$

in which

$$\begin{aligned} G_{ij} &= \left(-\cos[(\lambda_n + 2)\theta_i] \sin[(\lambda_n + 2)\theta_j]\right)^2 \left[\lambda_n (\lambda_n + 2) \left\{ (1 - \cos(2\theta_i))(1 - \cos(2\theta_j)) + \sin(2\theta_i) \sin(2\theta_j) \right\} \right] \\ &\quad - 2 \left(-\cos[(\lambda_n + 2)\theta_i] \sin[(\lambda_n + 2)\theta_j]\right)^2 \left[\cos(2\theta_j)(1 - \cos(2\theta_i)) - \sin(2\theta_i) \sin(2\theta_j) \right] \quad (i \neq j) \\ H_1 &= \lambda_n (\lambda_n + 2) \left\{ \cos^2[(\lambda_n + 2)\theta_1] \cos^2[(\lambda_n + 2)\theta_2] + \sin^2[(\lambda_n + 2)\theta_1] \sin^2[(\lambda_n + 2)\theta_2] \right\} \cdot \\ &\quad \left[(1 - \cos(2\theta_1))(1 - \cos(2\theta_2)) + \sin(2\theta_1) \sin(2\theta_2) \right] \\ H_2 &= -2 \left(\cos(2\theta_2) \sin(2\theta_1) - \cos(2\theta_1) \sin(2\theta_2) \right) \cdot \\ &\quad \frac{1}{4} \left\{ -\cos[2(\lambda_n + 2)\theta_1] \sin[2(\lambda_n + 2)\theta_2] + \cos[2(\lambda_n + 2)\theta_2] \sin[2(\lambda_n + 2)\theta_1] \right\} \end{aligned}$$

$$\begin{aligned}
 H_3 = & -2 \sin^2 [(\lambda_n + 2)\theta_1] \sin^2 [(\lambda_n + 2)\theta_2] (\cos(2\theta_1) + \cos(2\theta_2)) \\
 & + \sin [2(\lambda_n + 2)\theta_2] \sin(2\theta_2) + \sin [2(\lambda_n + 2)\theta_1] \sin(2\theta_1) \\
 & - \sin [2(\lambda_n + 2)\theta_1] \sin [2(\lambda_n + 2)\theta_2] \{ \cos(2\theta_1) \cos(2\theta_2) + \sin(2\theta_1) \sin(2\theta_2) \}
 \end{aligned} \tag{3-24}$$

In the Laplace domain, the shear modulus of the material becomes

$$\hat{\mu}_k = \frac{\mu_k^\infty}{s} + \frac{\mu_k^0 - \mu_k^\infty}{s + \frac{1}{\tau_k}} \quad \text{with } k = 1, 2 \tag{3-25}$$

The roots of the characteristic equation for specified value of Laplace transform variable provide the eigenvalues of the homogeneous system of equations in the Laplace domain. Determination of the roots requires numerical calculations because of the complexity of the characteristic equation. Depending on the material properties, their values may be complex. The roots only in the range of $-1 < \text{Re}(\lambda_n) < \infty$ are acceptable in the construction of the solution for the stress and displacement fields in order to achieve bounded strain energy at the junction.

As suggested by Lee (1997), after substituting for $\hat{\mu}_k$ in the expressions for \hat{M}_i and performing algebraic manipulations, their inversion can be expressed as

$$\begin{aligned}
 M_1 &= 16(1-\nu_1)^2 \\
 M_2(t) &= 16(1-\nu_2)^2 \left[\left(\frac{\mu_1^\infty}{\mu_2^\infty} \right)^2 + \{ 2\gamma_1 \mu_1^\infty (\tau_1 - \tau_2) \tau_1 + \ell_1(t) \} (\tau_1 - \tau_2) \kappa_1(t) - \gamma_2 (\ell_2(t) + \ell_3(t) \mu_2^\infty) \kappa_2(t) \right] \\
 M_3(t) &= 8(1-\nu_1) \left[1 - \frac{\mu_1^\infty}{\mu_2^\infty} - \gamma_1^2 (\tau_1 - \tau_2) \tau_1 \kappa_1(t) - \gamma_2 \mu_2^\infty (\gamma_1 \mu_2^0)^2 \tau_2 \kappa_2(t) \right]
 \end{aligned}$$

$$\begin{aligned}
 M_4(t) &= 8(1-\nu_2) \left[\frac{\mu_1^\infty}{\mu_2^\infty} \left(\frac{\mu_1^\infty}{\mu_2^\infty} - 1 \right) - \left\{ \gamma_1 \left(\gamma_3 + (\mu_1^\infty - \mu_2^\infty) \tau_1 - \mu_1^\infty \tau_2 \right) \tau_1 \right\} (\tau_1 - \tau_2) \kappa_1(t) + \right. \\
 &\quad \left. \gamma_2 \left\{ \ell_2(t) + \mu_2^\infty (\ell_3(t) - \gamma_4) \right\} \kappa_2(t) \right] \\
 M_5(t) &= \left(\frac{\mu_1^\infty}{\mu_2^\infty} - 1 \right)^2 + (2\gamma_1 \gamma_3 \tau_1 + \ell_1(t)) (\tau_1 - \tau_2) \kappa_1(t) + \gamma_2 \left(\ell_2(t) + \mu_2^\infty (\ell_3(t) - 2\gamma_4) \right) \kappa_2(t) \\
 M_6(t) &= 32(1-\nu_1)(1-\nu_2) \left[\frac{\mu_1^\infty}{\mu_2^\infty} + \gamma_1^2 (\tau_1 - \tau_2) \tau_1 \kappa_1(t) + \gamma_2 \mu_2^\infty (\gamma_1 \mu_2^0)^2 \tau_2 \kappa_2(t) \right] \quad (3-26)
 \end{aligned}$$

in which the functions $\kappa_k(t)$ are defined as

$$\begin{aligned}
 \kappa_1(t) &= \frac{\mu_1^0 - \mu_1^\infty}{\gamma_1^3 \tau_1} e^{-t/\tau_1} \\
 \kappa_2(t) &= \frac{\mu_2^0 - \mu_2^\infty}{(\mu_2^\infty)^2 (\mu_2^0)^3 \gamma_1^3 \tau_2} e^{-(\mu_2^\infty t)/(\mu_2^0 \tau_2)} \quad (3-27)
 \end{aligned}$$

with the requirement that $\gamma_i \neq 0$. The constants γ_i , with $i = 1, 4$, involving the initial and final shear moduli and the relaxation time are defined as

$$\begin{aligned}
 \gamma_1 &= \mu_2^\infty \tau_1 - \mu_2^0 \tau_2 \\
 \gamma_2 &= \mu_2^\infty \mu_1^0 \tau_1 - \mu_1^\infty \mu_2^0 \tau_2 \\
 \gamma_3 &= (\mu_1^\infty - \mu_2^\infty) (\tau_1 - \tau_2) + (\mu_2^0 - \mu_2^\infty) \tau_2 \\
 \gamma_4 &= (\gamma_1 \mu_2^0)^2 \tau_2 \quad (3-28)
 \end{aligned}$$

The functions $\ell_i(t)$, with $i = 1, 3$, that are linear in time are defined as

$$\ell_1(t) = (\mu_1^0 - \mu_1^\infty) \left[-\mu_2^\infty (t - \tau_1) (\tau_1 - \tau_2)^2 + \tau_2 (\mu_2^0 - \mu_2^\infty) \left\{ \tau_1 (t + \tau_1) - \tau_2 (t - \tau_1) \right\} \right]$$

$$\begin{aligned} \ell_2(t) &= \mu_1^\infty \gamma_1^2 \left[t \mu_2^\infty (\mu_2^0 - \mu_2^\infty) + \mu_2^0 (\mu_2^0 + \mu_2^\infty) \tau_2 \right] \\ \ell_3(t) &= (\mu_1^0 - \mu_1^\infty) \tau_1 \left[(\tau_1 - \tau_2) \left\{ (\mu_2^0)^2 (\mu_2^0 - \mu_2^\infty) (t + 3\tau_2) + 2(\mu_2^\infty)^3 \tau_2 \right\} + \right. \\ &\quad \left. \tau_2 (\mu_2^0 - \mu_2^\infty) \left\{ (\mu_2^0 - \mu_2^\infty) \tau_2 - \mu_2^\infty (t - \tau_1) \right\} \right] \end{aligned} \quad (3-29)$$

It is worth noting that the functions $\kappa_k(t)$ vanish for time independent elastic material response. In the case of one material, $\mu_1(t)$, being viscoelastic and the other, $\mu_2^0 = \mu_2^\infty$, elastic, it is necessary to select $\tau_1 \neq \tau_2$ so that $\gamma_1 \neq 0$. After inverting the coefficients,

\hat{M}_i , the characteristic equation in time can be expressed in the form

$$\begin{aligned} M_1(t)R_{11}(\lambda_n) + M_2(t)R_{12}(\lambda_n) + M_3(t)R_{12}(\lambda_n)R_{21}(\lambda_n) \\ + M_4(t)R_{11}(\lambda_n)R_{22}(\lambda_n) - M_5(t)R_{11}(\lambda_n)R_{12}(\lambda_n) - M_6(t)R^*(\lambda_n) = 0 \end{aligned} \quad (3-30)$$

The roots of the characteristic equation in this form provide the eigenvalues of the homogeneous system of equations for a specified time. The eigenvalues, $\lambda_n(t)$, and the corresponding eigenvectors permit the determination of the stress field within a multiplicative coefficient. This multiplicative coefficient depends on the magnitude of the loading and the geometry of the region. Therefore, in order to account for the finite geometry and loading, the solution method is based on the principle of virtual work and the study by Barut et al. (2001) that provides the singular stress fields at junctions of multiple dissimilar elastic materials under mechanical and thermal loading. In the Laplace domain, the total potential is expressed in the form

$$\pi(s) = \sum_{k=1}^2 \left\{ \frac{1}{2} \int_{A_k} \hat{\sigma}_{\alpha\beta}^{(k)} \hat{\varepsilon}_{\alpha\beta}^{(k)} dA - \int_{\Gamma_k} \hat{T}_\alpha^{(k)} (\hat{u}_\alpha^{(k)} - \hat{U}_\alpha^k) d\Gamma - \int_{\Gamma_k} \hat{t}_\alpha^k \hat{U}_\alpha^{(k)} d\Gamma \right\} \quad (3-31)$$

with $\alpha, \beta = x, y$. The unknown components of traction and displacement vectors along the circumferential boundary segments, Γ_k (shown in Figure 3-2), are denoted by \hat{T}_α^k and \hat{U}_α^k . The known applied traction components are represented by ${}^* \hat{t}_\alpha^k$. Substituting for the strain components in terms of displacement components in the expression for the total potential results in

$$\pi(s) = \sum_{k=1}^2 \left\{ \frac{1}{2} \int_{A_k} \hat{\sigma}_{\alpha\beta}^{(k)} \hat{u}_{\alpha,\beta}^{(k)} dA - \int_{\Gamma_k} \hat{T}_\alpha^{(k)} (\hat{u}_\alpha^{(k)} - \hat{U}_\alpha^k) d\Gamma - \int_{\Gamma_k} {}^* \hat{t}_\alpha^k \hat{U}_\alpha^{(k)} d\Gamma \right\} \quad (3-32)$$

Applying the divergence theorem leads to

$$\begin{aligned} \pi(s) = & \frac{1}{2} \sum_{k=1}^2 \left\{ - \int_{A_k} \hat{\sigma}_{\alpha\beta}^{(k)} \hat{u}_\alpha^{(k)} dA + \int_{\Gamma_k} \hat{\sigma}_{\alpha\beta}^{(k)} \hat{u}_\alpha^{(k)} n_\beta^{(k)} d\Gamma + \int_{\bar{\Gamma}_k} \hat{\sigma}_{\alpha\beta}^{(k)} \hat{u}_\alpha^{(k)} \bar{n}_\beta^{(k)} d\Gamma + \int_{\bar{\Gamma}_k} \hat{\sigma}_{\alpha\beta}^{(k)} \hat{u}_\alpha^{(k)} \bar{n}_\beta^{(k)} d\Gamma \right\} \\ & - \sum_{k=1}^2 \left\{ \int_{\Gamma_k} \hat{T}_\alpha^{(k)} (\hat{u}_\alpha^{(k)} - \hat{U}_\alpha^k) d\Gamma + \int_{\Gamma_k} {}^* \hat{t}_\alpha^k \hat{U}_\alpha^{(k)} d\Gamma \right\} \end{aligned} \quad (3-33)$$

The continuity conditions between the adjacent sectors require that

$$\begin{aligned} \tilde{u}_\alpha^{(1)} &= \bar{u}_\alpha^{(2)} \\ \sigma_{\alpha\beta}^{(1)} \tilde{n}_\alpha^{(1)} &= -\sigma_{\alpha\beta}^{(2)} \bar{n}_\alpha^{(2)} \end{aligned} \quad (3-34)$$

Traction-free surfaces are enforced as

$$\sigma_{\alpha\beta}^{(2)} \tilde{n}_\alpha^{(2)} = \sigma_{\alpha\beta}^{(1)} \bar{n}_\alpha^{(1)} = 0 \quad (3-35)$$

Invoking the equilibrium equations in each sector and enforcing these conditions while noting that the adjacent boundaries are related to each other by $\bar{\Gamma}_1 = \bar{\Gamma}_2$ and the expression for the total potential reduces to

$$\pi(s) = \sum_{k=1}^2 \left\{ \frac{1}{2} \int_{\Gamma_k} \hat{\sigma}_{\alpha\beta}^{(k)} \hat{u}_\alpha^{(k)} n_\beta^{(k)} d\Gamma - \int_{\Gamma_k} \hat{T}_\alpha^{(k)} (\hat{u}_\alpha^{(k)} - \hat{U}_\alpha^{(k)}) d\Gamma - \int_{\Gamma_k} \hat{t}_\alpha^k \hat{U}_\alpha^{(k)} d\Gamma \right\} \quad (3-36)$$

Representing the unknown components of the traction as $\hat{T}_\alpha^{(k)} = \hat{\sigma}_{\alpha\beta}^{(k)} n_\beta^{(k)}$ and substituting for them in the expression for the total potential results in

$$\pi(s) = \sum_{k=1}^2 \left\{ -\frac{1}{2} \int_{\Gamma_k} \hat{\sigma}_{\alpha\beta}^{(k)} \hat{u}_\alpha^{(k)} n_\beta^{(k)} d\Gamma + \int_{\Gamma_k} \hat{\sigma}_{\alpha\beta}^{(k)} \hat{U}_\alpha^k n_\beta^{(k)} d\Gamma - \int_{\Gamma_k} \hat{t}_\alpha^k \hat{U}_\alpha^{(k)} d\Gamma \right\} \quad (3-37)$$

In matrix notation, this expression can be written as

$$\pi(s) = \sum_{k=1}^2 \left\{ -\frac{1}{2} \int_{\Gamma_k} \hat{\boldsymbol{\sigma}}^{(k)T} \mathbf{n}^{(k)T} \hat{\mathbf{u}}^{(k)} d\Gamma + \int_{\Gamma_k} \hat{\boldsymbol{\sigma}}^{(k)T} \mathbf{n}^{(k)T} \hat{\mathbf{U}}^{(k)} d\Gamma - \int_{\Gamma_k} \hat{\mathbf{U}}^{(k)T} \hat{\mathbf{t}}^{(k)} d\Gamma \right\} \quad (3-38)$$

in which the vectors $\hat{\boldsymbol{\sigma}}^{(k)}$, $\hat{\mathbf{u}}^{(k)}$, $\hat{\mathbf{T}}^{(k)}$, and $\hat{\mathbf{U}}^{(k)}$ are defined as

$$\begin{aligned} \hat{\boldsymbol{\sigma}}^{(k)T} &= \{ \hat{\sigma}_{xx}^{(k)}, \hat{\sigma}_{yy}^{(k)}, \hat{\sigma}_{xy}^{(k)} \} \\ \hat{\mathbf{u}}^{(k)T} &= \{ \hat{u}_x^{(k)}, \hat{u}_y^{(k)} \} \\ \hat{\mathbf{t}}^{(k)T} &= \{ \hat{t}_x^{(k)}, \hat{t}_y^{(k)} \} \\ \hat{\mathbf{U}}^{(k)T} &= \{ \hat{U}_x^{(k)}, \hat{U}_y^{(k)} \} \end{aligned} \quad (3-39)$$

and the matrix $\mathbf{n}^{(k)}$ contains the components of the unit normal along Γ_k

$$\mathbf{n}^{(k)T} = \begin{bmatrix} n_x^{(k)} & 0 \\ 0 & n_y^{(k)} \\ n_y^{(k)} & n_x^{(k)} \end{bmatrix} \quad (3-40)$$

The transformation matrices, $\mathbf{Z}_\sigma^{(k)}$ and $\mathbf{Z}_u^{(k)}$, given by

$$\mathbf{Z}_\sigma^{(k)} = \begin{bmatrix} (n_x^{(k)})^2 & (n_y^{(k)})^2 & -2n_x^{(k)}n_y^{(k)} \\ (n_y^{(k)})^2 & (n_x^{(k)})^2 & 2n_x^{(k)}n_y^{(k)} \\ n_x^{(k)}n_y^{(k)} & -n_x^{(k)}n_y^{(k)} & (n_x^{(k)})^2 - (n_y^{(k)})^2 \end{bmatrix}$$

and

$$\mathbf{Z}_u^{(k)} = \begin{bmatrix} n_x^{(k)} & -n_y^{(k)} \\ n_y^{(k)} & n_x^{(k)} \end{bmatrix} \quad (3-41)$$

permit the vectors of stress and displacement components to be expressed as

$$\begin{aligned} \hat{\boldsymbol{\sigma}}^{(k)} &= \mathbf{Z}_\sigma^{(k)} \hat{\boldsymbol{\sigma}}_p^{(k)} \\ \hat{\mathbf{u}}^{(k)} &= \mathbf{Z}_u^{(k)} \hat{\mathbf{u}}_p^{(k)} \end{aligned} \quad (3-42)$$

Their substitution in the total potential results in

$$\pi(s) = \sum_{k=1}^2 \left\{ -\frac{1}{2} \int_{\Gamma_k} \hat{\boldsymbol{\sigma}}_p^{(k)T} \mathbf{Z}_\sigma^{(k)T} \mathbf{n}^{(k)} \mathbf{Z}_u^{(k)} \hat{\mathbf{u}}_p^{(k)} d\Gamma + \int_{\Gamma_k} \hat{\boldsymbol{\sigma}}_p^{(k)T} \mathbf{Z}_\sigma^{(k)T} \mathbf{n}^{(k)} \hat{\mathbf{U}}^{(k)} d\Gamma - \int_{\Gamma_k} \hat{\mathbf{U}}^{(k)T} * \hat{\mathbf{t}}^{(k)} d\Gamma \right\} \quad (3-43)$$

The vectors of stress and displacement components in the Laplace domain are defined by

$$\hat{\boldsymbol{\sigma}}_p^{(k)T} = \{ \hat{\sigma}_{rr}^{(k)}, \hat{\sigma}_{\theta\theta}^{(k)}, \hat{\sigma}_{r\theta}^{(k)} \} \text{ and } \hat{\mathbf{u}}_p^{(k)T} = \{ \hat{u}_r^{(k)}, \hat{u}_\theta^{(k)} \} \quad (3-44)$$

and that they can be expressed as

$$\hat{\boldsymbol{\sigma}}_p^{(k)} = \text{Re} \left\{ \sum_{n=1}^N \hat{\mathbf{F}}_n^{(k)}(r, \theta; s, \lambda_n) \hat{\mathbf{q}}_n^{(k)} \hat{\alpha}_n \right\} \text{ and } \hat{\mathbf{u}}_p^{(k)} = \text{Re} \left\{ \sum_{n=1}^N \hat{\mathbf{G}}_n^{(k)}(r, \theta; s, \lambda_n) \hat{\mathbf{q}}_n^{(k)} \hat{\alpha}_n \right\} \quad (3-45)$$

The vector $\hat{\mathbf{q}}_n^{(k)}$ contains the known coefficients, $\hat{A}_n^{(k)}$, $\hat{B}_n^{(k)}$, $\hat{C}_n^{(k)}$, and $\hat{D}_n^{(k)}$ in terms of $\hat{\alpha}_n$ corresponding to λ_n . The matrices $\hat{\mathbf{F}}_n^{(k)}$ and $\hat{\mathbf{G}}_n^{(k)}$ are defined as

$$\hat{\mathbf{F}}_n^{(k)} = r^{\lambda_n} \begin{bmatrix} \frac{(2-\lambda_n)}{4} \cos \lambda_n \theta & \frac{(2-\lambda_n)}{4} \sin \lambda_n \theta & -\cos(2+\lambda_n)\theta & -\sin(2+\lambda_n)\theta \\ \frac{(2+\lambda_n)}{4} \cos \lambda_n \theta & \frac{(2+\lambda_n)}{4} \sin \lambda_n \theta & \cos(2+\lambda_n)\theta & \sin(2+\lambda_n)\theta \\ \frac{\lambda_n}{4} \sin \lambda_n \theta & -\frac{\lambda_n}{4} \cos \lambda_n \theta & \sin(2+\lambda_n)\theta & -\cos(2+\lambda_n)\theta \end{bmatrix} \quad (3-46)$$

and

$$\hat{\mathbf{G}}_n^{(k)} = r^{\lambda_n+1} \begin{bmatrix} \hat{a}_n^{(k)} \cos \lambda_n \theta & \hat{a}_n^{(k)} \sin \lambda_n \theta & -\hat{b}_n^{(k)} \cos(\lambda_n+2)\theta & -\hat{b}_n^{(k)} \sin(\lambda_n+2)\theta \\ \hat{c}_n^{(k)} \sin \lambda_n \theta & \hat{c}_n^{(k)} \cos \lambda_n \theta & \hat{b}_n^{(k)} \sin(\lambda_n+2)\theta & -\hat{b}_n^{(k)} \cos(\lambda_n+2)\theta \end{bmatrix} \quad (3-47)$$

in which

$$\hat{a}_n^{(k)} = \frac{4(1-\nu_k) - (2+\lambda_n)}{8(1+\lambda_n)s\hat{\mu}_k}; \quad \hat{b}_n^{(k)} = \frac{1}{2s\hat{\mu}_k}; \quad \hat{c}_n^{(k)} = \frac{4(1-\nu_k) + \lambda_n}{8(1+\lambda_n)s\hat{\mu}_k} \quad (3-48)$$

The stress and displacement vectors can be rewritten in terms of real variables as

$$\hat{\mathbf{\sigma}}_p^{(k)} = \sum_{n=1}^N {}^* \hat{\mathbf{F}}_n^{(k)} {}^* \hat{\mathbf{a}}_n \quad \text{and} \quad \hat{\mathbf{u}}_p^{(k)} = \sum_{n=1}^N {}^* \hat{\mathbf{G}}_n^{(k)} {}^* \hat{\mathbf{a}}_n \quad (3-49)$$

where the real matrices ${}^* \hat{\mathbf{F}}_n^{(k)}$ and ${}^* \hat{\mathbf{G}}_n^{(k)}$, and the real vector ${}^* \hat{\mathbf{a}}_n$ are defined by

$${}^* \hat{\mathbf{F}}_n^{(k)} = \left[\text{Re} \left\{ \hat{\mathbf{F}}_n^{(k)} \hat{\mathbf{q}}_n^{(k)} \right\} \mid -\text{Im} \left\{ \hat{\mathbf{F}}_n^{(k)} \hat{\mathbf{q}}_n^{(k)} \right\} \right]$$

$${}^* \hat{\mathbf{G}}_n^{(k)} = \left[\text{Re} \left\{ \hat{\mathbf{G}}_n^{(k)} \hat{\mathbf{q}}_n^{(k)} \right\} \mid -\text{Im} \left\{ \hat{\mathbf{G}}_n^{(k)} \hat{\mathbf{q}}_n^{(k)} \right\} \right]$$

$${}^* \hat{\mathbf{a}}_n^T = \{ \text{Re}(\hat{a}_n), \text{Im}(\hat{a}_n) \} \quad (3-50)$$

The circumferential boundary can be discretized by introducing collocation points as shown in Figure 3-3. The displacement components associated with the collocation points are contained in the vector $\hat{\mathbf{v}}$, and they vary linearly between the two consecutive

collocation points. Thus, the vector of displacement components, $\hat{\mathbf{U}}^{(k)}$, along the circumferential boundary can be expressed in the form

$$\hat{\mathbf{U}}^{(k)} = \mathbf{\Lambda}^{(k)} \hat{\mathbf{v}} \quad (3-51)$$

in which the matrix $\mathbf{\Lambda}^{(k)}$ contains the linear interpolation functions given in Appendix A.

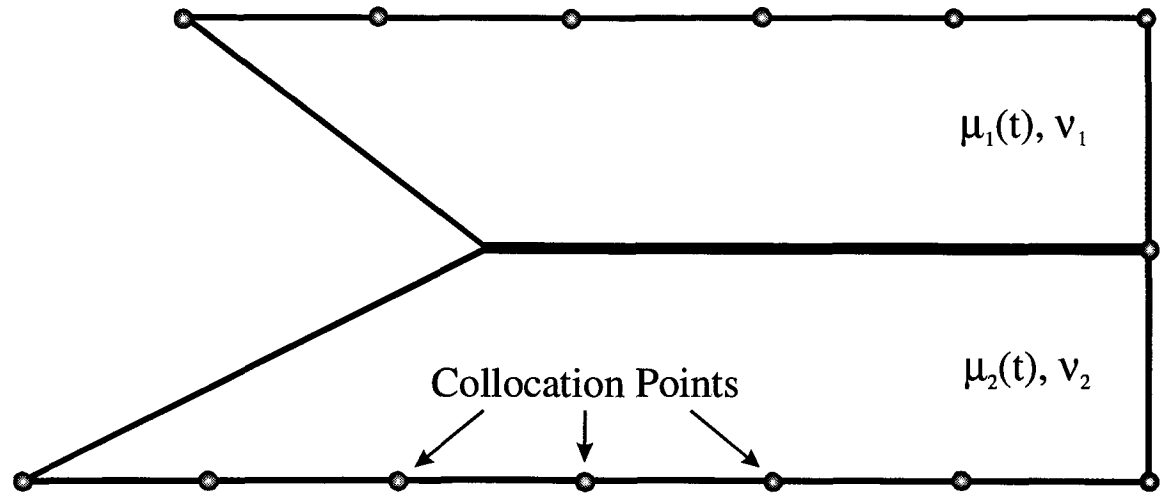


Figure 3-3: Collocation (integration) points along the boundary of the finite region.

Substituting for $\hat{\mathbf{g}}_p^{(k)}$, $\hat{\mathbf{u}}_p^{(k)}$, and $\hat{\mathbf{U}}^{(k)}$ in the expression for the total potential leads to

$$\begin{aligned} \pi(s) = & -\frac{1}{2} \sum_{k=1}^2 \sum_{i=1}^N \sum_{j=1}^N \hat{\mathbf{a}}_i^T \left\{ \int_{\Gamma_k} \hat{\mathbf{F}}_i^{(k)T} \mathbf{Z}_\sigma^{(k)T} \mathbf{n}^{(k)} \mathbf{Z}_u^{(k)} \hat{\mathbf{G}}_j^{(k)} d\Gamma \right\} \hat{\mathbf{a}}_j \\ & + \sum_{k=1}^2 \sum_{i=1}^N \hat{\mathbf{a}}_i^T \left\{ \int_{\Gamma_k} \hat{\mathbf{F}}_i^{(k)T} \mathbf{Z}_\sigma^{(k)T} \mathbf{n}^{(k)} \mathbf{\Lambda}^{(k)} d\Gamma \right\} \hat{\mathbf{v}} - \sum_{k=1}^2 \hat{\mathbf{v}}^T \left\{ \int_{\Gamma_k} \mathbf{\Lambda}^{(k)T} \hat{\mathbf{t}}_u^{(k)} d\Gamma \right\} \end{aligned} \quad (3-52)$$

The total potential can be rewritten as

$$\pi(s) = -\frac{1}{2} \sum_{k=1}^2 \sum_{i=1}^N \sum_{j=1}^N \hat{\mathbf{a}}_i^T \mathbf{H}_{ij}^{(k)} \hat{\mathbf{a}}_j + \sum_{k=1}^2 \sum_{i=1}^N \hat{\mathbf{a}}_i^T \mathbf{R}_i^{(k)} \hat{\mathbf{v}} - \sum_{k=1}^2 \hat{\mathbf{v}}^T \hat{\mathbf{f}}_i^{(k)} \quad (3-53)$$

where

$$\begin{aligned}\hat{\mathbf{H}}_{ij}^{(k)} &= \int_{\Gamma_k} \hat{\mathbf{F}}_i^{(k)T} \mathbf{Z}_\sigma^{(k)T} \mathbf{n}^{(k)} \mathbf{Z}_u^{(k)} \hat{\mathbf{G}}_j^{(k)} d\Gamma \\ \hat{\mathbf{R}}_i^{(k)} &= \int_{\Gamma_k} \hat{\mathbf{F}}_i^{(k)T} \mathbf{Z}_\sigma^{(k)T} \mathbf{n}^{(k)} \boldsymbol{\Lambda}^{(k)} d\Gamma \\ {}^* \hat{\mathbf{f}}^{(k)} &= \int_{\Gamma_k} \boldsymbol{\Lambda}^{(k)T} {}^* \hat{\mathbf{t}}^{(k)} d\Gamma\end{aligned}\quad (3-54)$$

The total potential can be cast as

$$\pi(s) = -\frac{1}{2} \sum_{k=1}^2 \hat{\boldsymbol{\alpha}}^T \mathbf{H}^{(k)} \hat{\boldsymbol{\alpha}} + \sum_{k=1}^2 \hat{\boldsymbol{\alpha}}^T \mathbf{R}^{(k)} \hat{\mathbf{v}} - \sum_{k=1}^2 \hat{\mathbf{v}}^T {}^* \mathbf{f}^{(k)} \quad (3-55)$$

in which

$$\hat{\boldsymbol{\alpha}}^T = \left\{ \hat{\boldsymbol{\alpha}}_1^T, \hat{\boldsymbol{\alpha}}_2^T, \hat{\boldsymbol{\alpha}}_3^T, \dots, \hat{\boldsymbol{\alpha}}_N^T \right\} \quad (3-56)$$

and

$$\hat{\mathbf{H}}^{(k)} = \begin{bmatrix} \hat{\mathbf{H}}_{11}^{(k)} & \hat{\mathbf{H}}_{12}^{(k)} & \dots & \hat{\mathbf{H}}_{1N}^{(k)} \\ \hat{\mathbf{H}}_{21}^{(k)} & \hat{\mathbf{H}}_{22}^{(k)} & \dots & \hat{\mathbf{H}}_{2N}^{(k)} \\ \vdots & \vdots & & \vdots \\ \hat{\mathbf{H}}_{N1}^{(k)} & \hat{\mathbf{H}}_{N1}^{(k)} & \dots & \hat{\mathbf{H}}_{NN}^{(k)} \end{bmatrix}$$

$$\hat{\mathbf{R}}^{(k)T} = \left\{ \hat{\mathbf{R}}_1^{(k)T}, \hat{\mathbf{R}}_2^{(k)T}, \hat{\mathbf{R}}_3^{(k)T}, \dots, \hat{\mathbf{R}}_N^{(k)T} \right\} \quad (3-57)$$

Defining

$$\hat{\mathbf{H}} = \sum_{k=1}^2 \hat{\mathbf{H}}^{(k)}; \quad \hat{\mathbf{R}} = \sum_{k=1}^2 \hat{\mathbf{R}}^{(k)}; \quad {}^* \hat{\mathbf{f}} = \sum_{k=1}^2 {}^* \hat{\mathbf{f}}^{(k)} \quad (3-58)$$

permits the expression of the potential energy in its final form as

$$\pi(s) = -\frac{1}{2} \hat{\boldsymbol{\alpha}}^T \hat{\mathbf{H}} \hat{\boldsymbol{\alpha}} + \hat{\boldsymbol{\alpha}}^T \hat{\mathbf{R}} \hat{\mathbf{v}} - \hat{\mathbf{v}}^T {}^* \hat{\mathbf{f}} \quad (3-59)$$

The unknown vectors $\hat{\mathbf{a}}$ and $\hat{\mathbf{v}}$ represent the generalized coordinates associated with the deformations and the displacements components at the collocation points. In order to express the total potential in terms of one unknown vector, $\hat{\mathbf{v}}$, the first variation of the total potential with respect to $\hat{\mathbf{a}}$ is taken, leading to

$$\delta\pi = -\delta\hat{\mathbf{a}}^T \{ \hat{\mathbf{H}}' \hat{\mathbf{a}} - \hat{\mathbf{R}} \hat{\mathbf{v}} \} = 0 \quad (3-60)$$

in which

$$\hat{\mathbf{H}}' = \frac{1}{2} \{ \hat{\mathbf{H}} + \hat{\mathbf{H}}^T \} = \hat{\mathbf{H}}$$

where $\hat{\mathbf{H}} = \hat{\mathbf{H}}^T$ is based on Maxwell's reciprocal theorem. Enforcing the first variation with respect to $\hat{\mathbf{a}}$ to vanish results in

$$\delta\hat{\mathbf{a}}^T \{ \hat{\mathbf{H}}' \hat{\mathbf{a}} - \hat{\mathbf{R}} \hat{\mathbf{v}} \} = 0 \quad (3-61)$$

Solution to this equation yields $\hat{\mathbf{a}}$ in terms of the nodal displacement vector, $\hat{\mathbf{v}}$, as

$$\hat{\mathbf{a}} = \hat{\mathbf{H}}^{-1} \hat{\mathbf{R}} \hat{\mathbf{v}} \quad (3-62)$$

Substituting for $\hat{\mathbf{a}}$ in the expression for the total potential leads to

$$\pi(s) = \frac{1}{2} \hat{\mathbf{v}}^T \hat{\mathbf{R}}^T \hat{\mathbf{H}}^{-1} \hat{\mathbf{R}} \hat{\mathbf{v}} - \hat{\mathbf{v}}^T \hat{\mathbf{f}} \quad (3-63)$$

Enforcing the first variation of the total potential to vanish results in the final form of the equilibrium equations as

$$\delta\pi = \hat{\mathbf{v}}^T \{ \hat{\mathbf{K}} \hat{\mathbf{v}} - \hat{\mathbf{f}} \} = 0 \quad (3-64)$$

leading to

$$\hat{\mathbf{K}} \hat{\mathbf{v}} = \hat{\mathbf{f}} \quad (3-65)$$

in which $\hat{\mathbf{K}}$ is defined as $\hat{\mathbf{K}} = \hat{\mathbf{R}}^T \hat{\mathbf{H}}^{-1} \hat{\mathbf{R}}$. The vector ${}^* \hat{\mathbf{f}}$ represents external force components. Finally, the unknown vectors, $\hat{\alpha}$ and $\hat{\mathbf{v}}$, are determined as

$$\hat{\mathbf{v}} = \hat{\mathbf{K}}^{-1} {}^* \hat{\mathbf{f}} \text{ and } \hat{\alpha} = \hat{\mathbf{H}}^{-1} \hat{\mathbf{R}} \hat{\mathbf{K}}^{-1} {}^* \hat{\mathbf{f}} \quad (3-66)$$

Determination of $\hat{\alpha}$ permits the calculation of the stress and displacement components in the Laplace domain. Their inversion to the time space is achieved by employing the approximate inversion method introduced by Schapery (1961). Based on this method, the stress and displacement components are inverted as

$$\sigma_p^{(k)}(t) = \left\{ s \hat{\sigma}_p^{(k)}(s) \right\} \Big|_{s=1/2t} \text{ and } \mathbf{u}_p^{(k)}(t) = \left\{ s \hat{\mathbf{u}}_p^{(k)}(s) \right\} \Big|_{s=1/2t} \quad (3-67)$$

This approach captures the exact nature of the singular stress field near the junction arising from the material and geometric discontinuities. The equilibrium equations are also satisfied exactly. The boundary conditions are satisfied in a sense of principle of minimum potential energy while enforcing linear displacement variation along the boundary between the collocation points. The inversion of the characteristic equation yielding the strength of the singularity is exact while the inversion of the stress and displacement components along the interface is approximate.

Stress intensity factor can be expressed as

$$K = \sigma \sqrt{\pi r} \quad (3-68)$$

which allows for the calculation of K if the stress field is known and an appropriate value of r is selected. In order to avoid difficulties associated with the selection of a proper r value, though, the dependence can be removed by expressing the stress with

$$\sigma = \frac{1}{\sqrt{r}} F(\theta) \quad (3-69)$$

where the function F is the inverse transform of one of the functions $\hat{F}_{\alpha\beta}^{(k)}(\theta; s, \lambda_n)$ as defined in (3-11) and (3-12). The arguments s and λ_n are known from the problem solution and for cracks in the dissimilar material junction formulation presented the angle θ is defined as zero. This allows (3-68) to be recast as

$$\begin{aligned} K_I &= \sqrt{\pi} F_{\theta\theta}(0) \\ K_{II} &= \sqrt{\pi} F_{r\theta}(0) \end{aligned} \quad (3-70)$$

The energy release rate for an interfacial crack is given by Hutchinson (1991) as

$$G = \frac{1-\beta^2}{E_*} (K_I^2 + K_{II}^2) \quad (3-71)$$

where E_* is a pseudo-Young's Modulus based on the two dissimilar material properties and defined as

$$\frac{1}{E_*} = \frac{1}{2} \left(\frac{1}{E_1} + \frac{1}{E_2} \right) \quad (3-72)$$

and the terms \overline{E}_i are given as

$$\begin{aligned} \overline{E}_i &= E_i \quad (\text{plane stress}) \\ &= \frac{E_i}{1-\nu_i^2} \quad (\text{plane strain}) \end{aligned} \quad (3-73)$$

The parameter β is a measure of the mismatch between the material properties of the two regions and is defined by

$$\beta = \frac{1}{2} \frac{\mu_1(1-2\nu_2) - \mu_2(1-2\nu_1)}{\mu_1(1-\nu_2) + \mu_2(1-\nu_1)} \quad (3-74)$$

It should be noted that for both regions having the same material properties (3-71) simplifies to the equation for the energy release rate for a crack in a homogeneous material.

3.3. Validation of Analytical Model

In order to establish the validity of the present solution method, two bonded dissimilar regions, shown in Figure 3-4, are considered under uniform strain. As the relaxation parameter of the shear modulus, τ_2 , approaches infinity, the second material loses all time dependent behavior, thereby becoming an elastic material. In this case, the elastic and viscoelastic material combination considered by Lee (1997) is recovered, thus serving as the validation of the current formulation. The shear moduli of the materials specified by Lee are $\mu_1^0 = 1000$ MPa, $\mu_1^\infty = 500$ MPa, $\tau_1 = 10$ min, $\mu_2^0 = 100,000$ MPa and $\mu_2^\infty = 50,000$ MPa with varying τ_2 . The time independent Poisson's ratios are specified as $\nu_1 = 0.35$ and $\nu_2 = 0.2$. As shown in Figure 4-1, the finite geometry of the region is defined by the parameters $L = 7$ cm, $c = 1$ cm, and $h = 1$ cm, with the wedge angles of $\theta_1 = -\theta_2 = \frac{\pi}{2}$. The boundary conditions for the finite model are prescribed by $u_y(x, y = -h) = 0$ and $u_y(x, y = c) = \varepsilon_0(c+h)H(t)$ with $\varepsilon_0 = 0.01$ for $x \in (0, L)$. The remaining boundary conditions are enforced as $u_x(x = L, y) = 0$ and $\sigma_{xx}(x = 0, y) = \sigma_{xy}(x = 0, y) = 0$ for $y \in (-h, c)$. In this analysis, the number of

eigenvalues retained in the solution and the number of collocation points along the boundary are taken as 17.

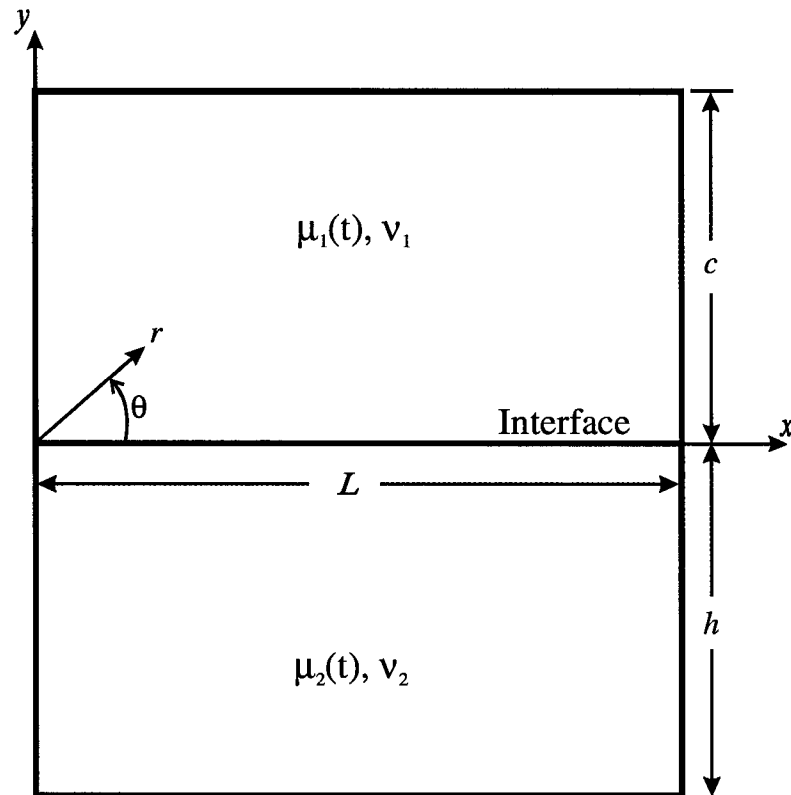


Figure 3-4: *Bonded dissimilar viscoelastic regions.*

As shown in Figure 3-5, the strength of the singularity is dictated by the degree of relaxation of the materials. As the relaxation time τ_2 increases, the result reported by Lee (1997) is recovered exactly when $\tau_2 = 100,000\tau_1$. As expected for this material combination, the strength of the singularity ceases to be time dependent for the dissimilar materials having equal relaxation times. In the limiting case ($\tau_2 \rightarrow \infty$) of bonded viscoelastic and elastic materials, the relaxation of the peeling and shear stresses close to the junction along the interface is shown in Figures 3-6 and 3-7. The variation of these stress components along the interface at specific times are shown in Figures 3-8 and 3-9.

In the limiting time values ($t = 0, \infty$), the present analysis recovers the stresses obtained from an elastic finite element analysis. In the limiting cases (0 and ∞) of the relaxation time τ_1 , the finite element analysis predictions deviate from the results by Lee (1997) by a factor of four. Therefore, it is suspected that there exists a typographical error involving a factor of four in Lee's study.

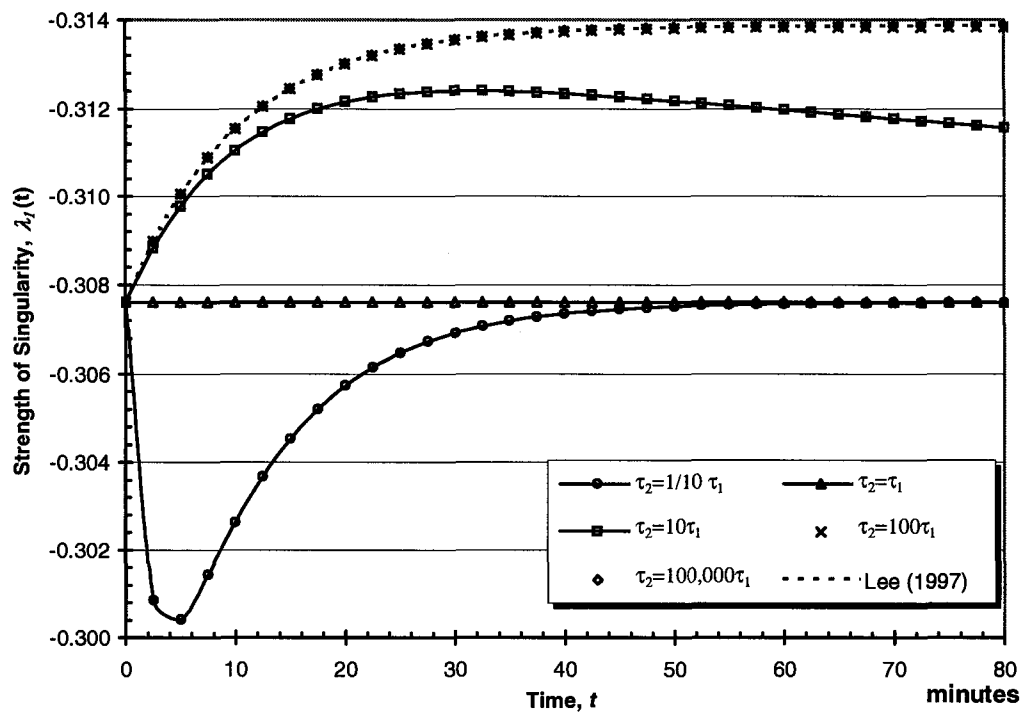


Figure 3-5: Strength of the singularity as the second material loses its relaxation.

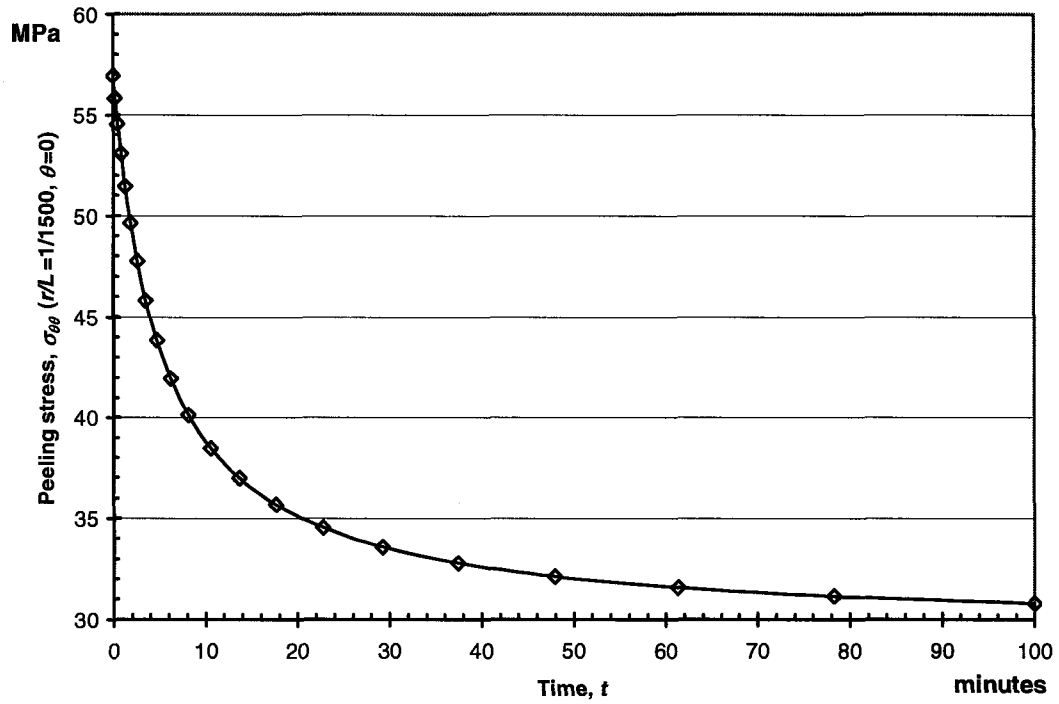


Figure 3-6: Relaxation of peeling stress near the junction point along the interface for a combination of viscoelastic and elastic materials.

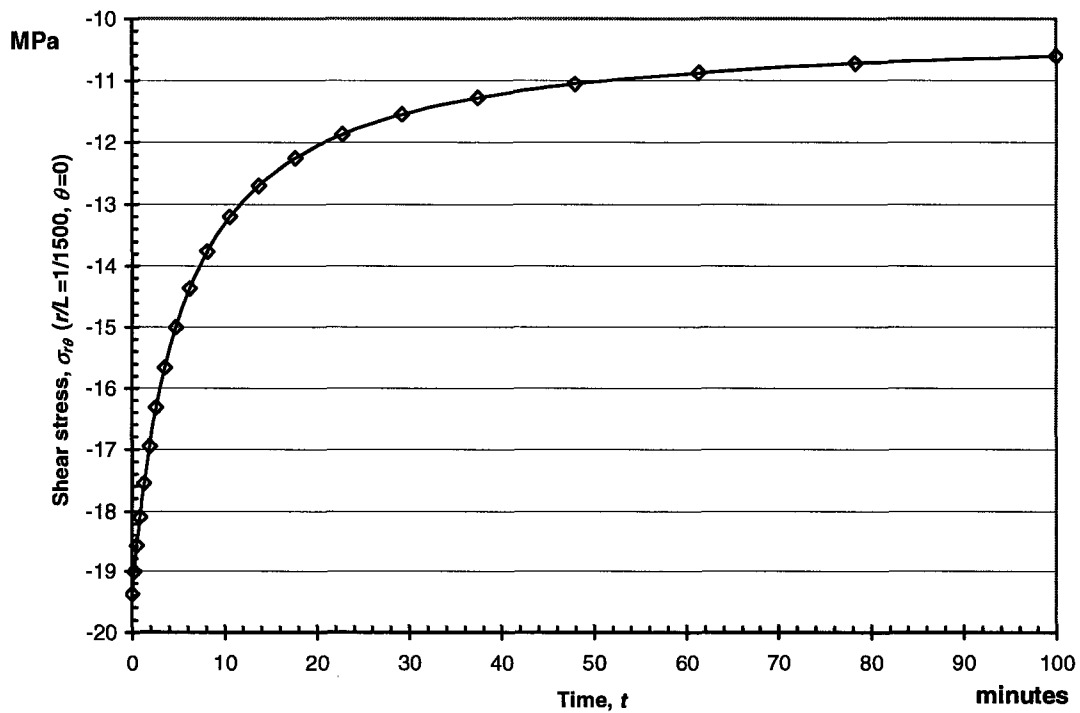


Figure 3-7: Relaxation of shear stress near the junction point along the interface for a combination of viscoelastic and elastic materials.

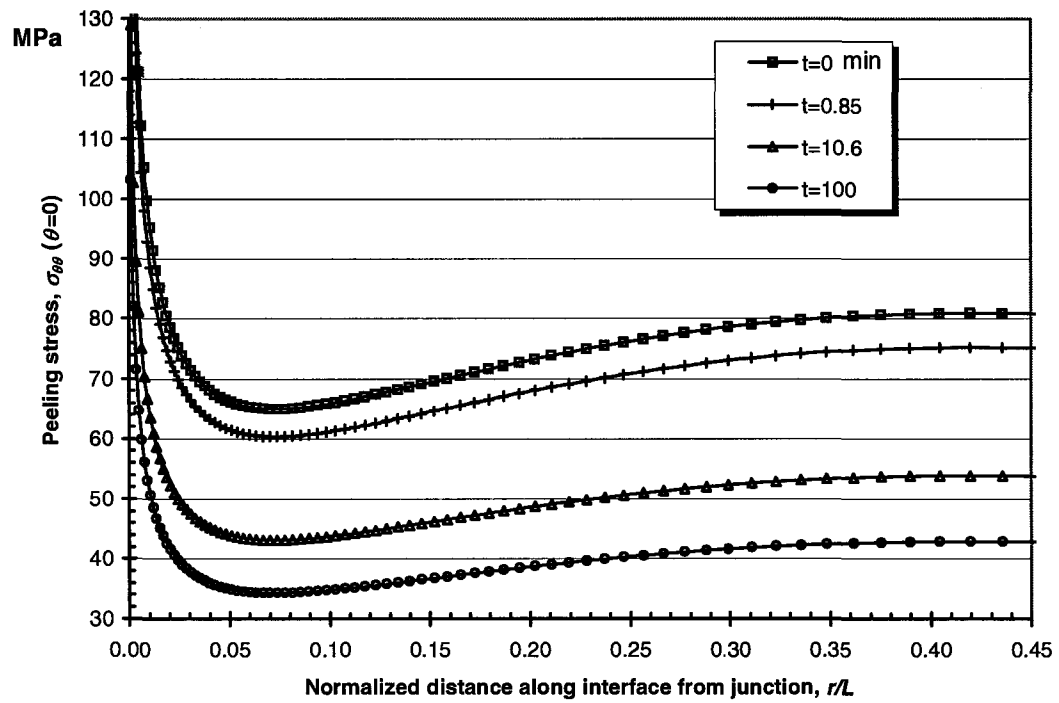


Figure 3-8: Variation of the peeling stress along the interface away from the junction point at various times for a combination of viscoelastic and elastic materials.

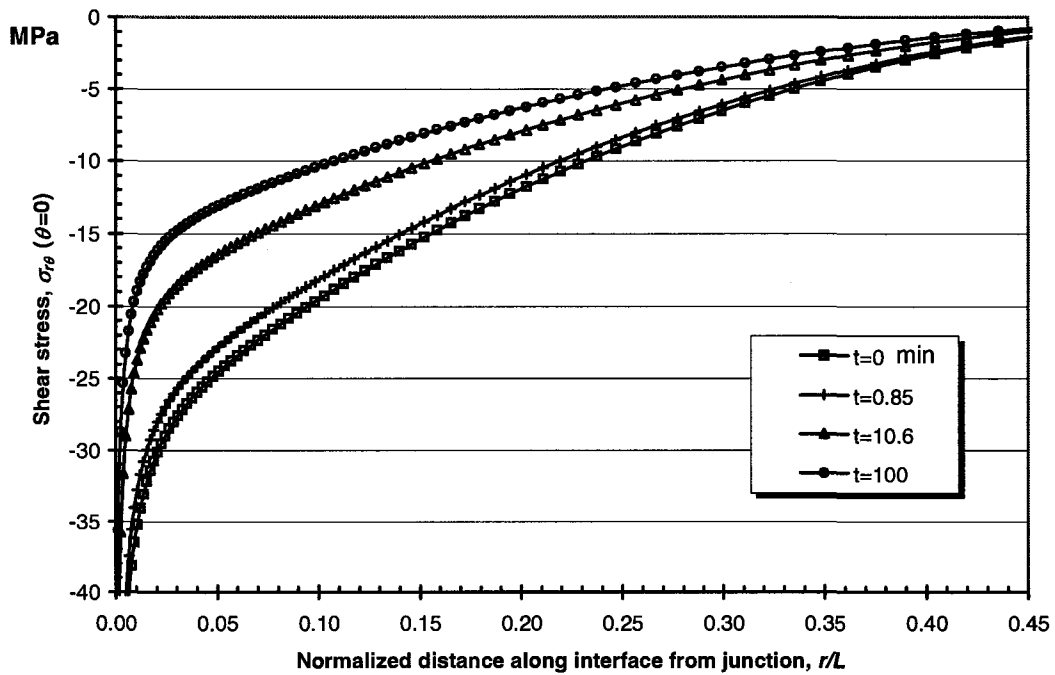


Figure 3-9: Variation of the shear stress along the interface away from the junction point at various times for a combination of viscoelastic and elastic materials.

After the validation of the current formulation, as an extension of the previous geometric configuration, a crack between two dissimilar viscoelastic materials, shown in Figure 3-10, is considered by defining the wedge angles to be $\theta_1 = -\theta_2 = \pi$. The loading and boundary conditions remains the same as in the previous configuration. Along the crack surface, the traction free boundary conditions are enforced. The material constants for the shear moduli are specified as $\mu_1^0 = 300$ MPa, $\mu_1^\infty = 200$ MPa, $\tau_1 = 20$ min and $\mu_2^0 = 700$ MPa, $\mu_2^\infty = 500$ MPa, $\tau_2 = 5$ min. Their Poisson's ratios are specified as $\nu_1 = 0.29$ and $\nu_2 = 0.32$. The finite geometry of the region (Figure 3-10) is defined by the parameters $L = 7$ cm, $a = 1.75$ cm, $c = 1$ cm, and $h = 1$ cm. In this analysis, the number of collocation points along the boundaries is 15 and the number of eigenvalues retained is 21. The stress intensity factors are calculated by using $K_I(t) = \lim_{r \rightarrow 0} \left[\sigma_{\theta\theta}(t) (2\pi r)^{\lambda_1(t)} \right]$ and $K_{II}(t) = \lim_{r \rightarrow 0} \left[\sigma_{r\theta}(t) (2\pi r)^{\lambda_1(t)} \right]$, where $\lambda_1(t)$ is the leading order singularity.

As expected, the real part of the singularity is not time dependent and is equal to $-1/2$. The time dependency of the oscillatory (imaginary) part of the singularity is shown in Figure 3-11. As time goes to infinity, the solution for the elastic problem corresponding to the limiting value is recovered. The relaxation of the stress intensity factors are presented in Figure 3-12. Again, in the limiting case, the elastic solutions are recovered.

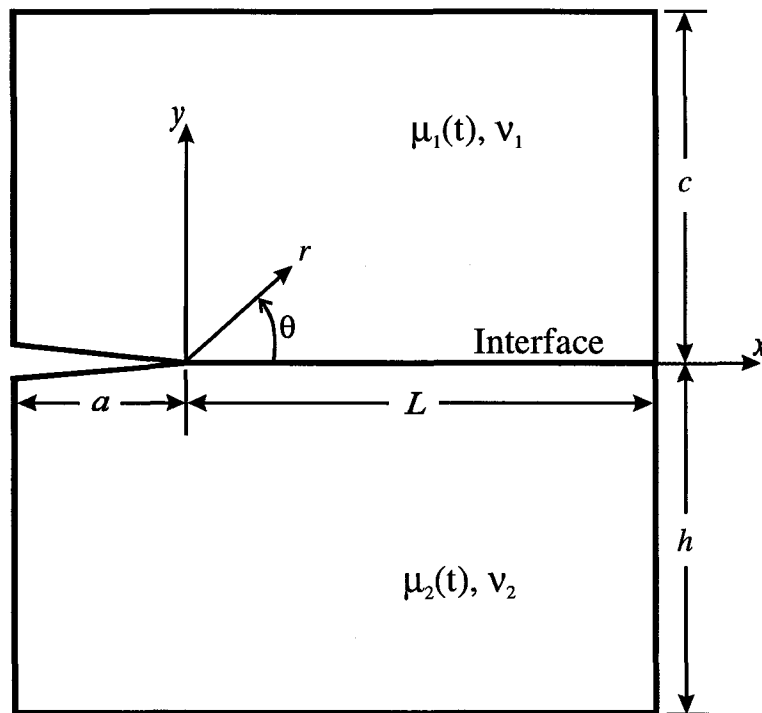


Figure 3-10: An interface crack between two bonded dissimilar viscoelastic materials.

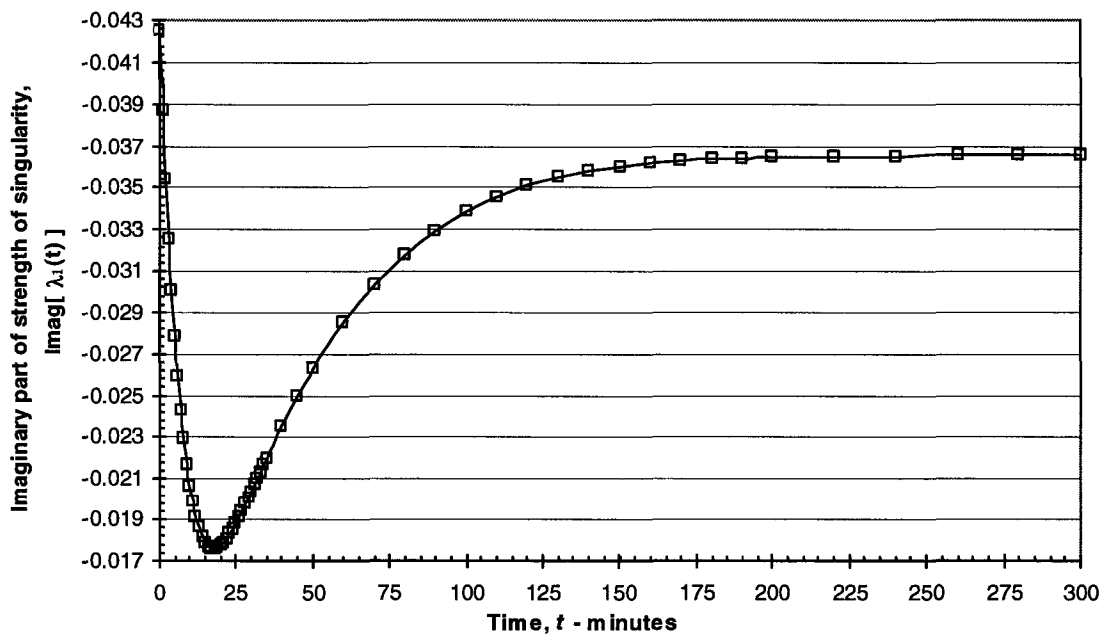


Figure 3-11: Time dependence of the imaginary (oscillatory) part of the singularity for an interface crack between two viscoelastic materials.

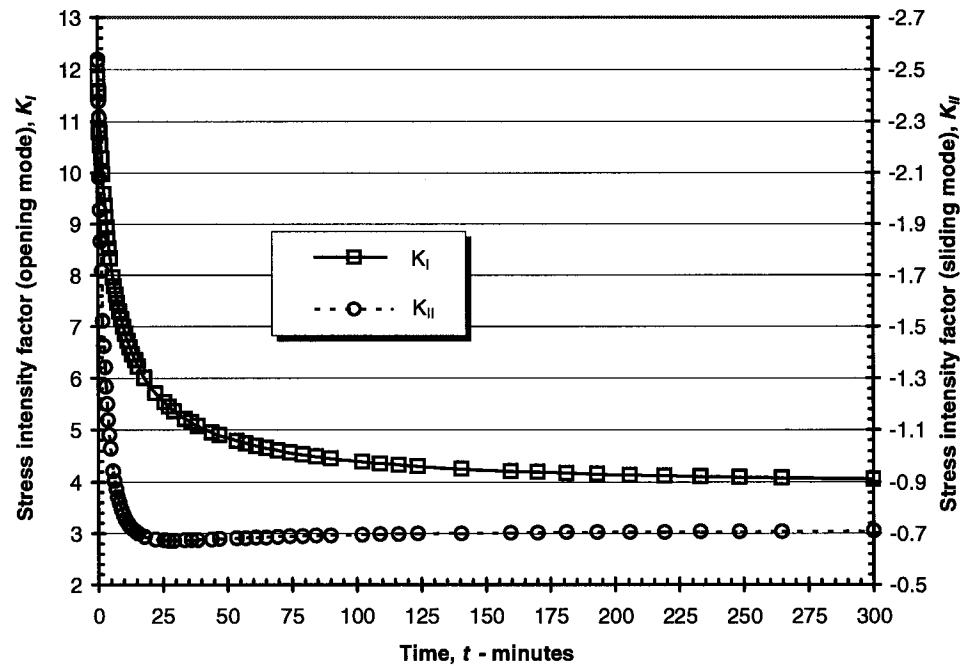


Figure 3-12: Relaxation of the stress intensity factor for an interface crack between two viscoelastic materials.

3.4. Summation

Also necessary for this study was the development of an analysis method for determining the strength of the singularity and the stress field in a finite region of two dissimilar viscoelastic materials under general loading conditions. The strength of the singularity is obtained in time space without resorting to approximate Laplace inversion techniques. In order to account for the effect of finite geometry, the stress field is obtained based on the principle of virtual work in conjunction with the use of Laplace transformation to eliminate time dependency. In the Laplace domain, the equilibrium equations are satisfied exactly; however, the boundary conditions are satisfied approximately in the

sense of energy minimization. The expressions for the stress field in the time domain are obtained by employing an approximate inversion technique.

In the limiting case for two viscoelastic regions, where one viscoelastic material becomes elastic, the results from previous studies for the strength of the singularity are recovered. In addition, the stresses obtained from the approximate Laplace inversion method also match favorably with previous studies, further validating the technique. When a crack is introduced between dissimilar viscoelastic regions, the value of the leading order eigenvalue becomes complex. For this geometry, the stress intensity factors also experience relaxation.

4. EXTRACTION OF FRACTURE PARAMETERS

In this chapter, the analytical model developed in Chapter 3 is validated and then applied to two problems. The remainder of the chapter presents the work on six post-production electronic packages. For all of the test cases, the first and last images captured during the testing procedure are presented followed by an image showing the interface, crack tip, and the region of correlation. Due to the large number of data points (over 20,000), the displacement data from the digital image correlation is not given but the process used to find the relative displacements from the raw data is outlined in Appendix B. The stresses along the interface from the analytical model are then given, as are the stress intensity factors. Finally, the critical energy release rate is calculated. A summary of the stress intensity factors and critical energy release rates from all tests ends the chapter.

4.1. Experimental Measurements and Extraction of Fracture Parameters

The results from each specimen are presented as a separate subsection. Each test result consists of an image pair obtained from the testing, an image highlighting the active correlation area, crack tip, and interface, a plot of the stresses near the crack tip along the interface obtained from the model, the stress intensity factors, and the critical energy release rate. Comments on each test are given at the end of each subsection. Note that due to the immense number of data points obtained from the digital image correlation (approximately 20,000 data points), these results are not given. The process used to obtain the relative displacements from the raw data is outlined in Appendix B.

All specimens were created from the same package type. In all images the upper material is the die (silicon), the middle layer is the underfill (filled epoxy) and the bottom material is FR-4 (fiberglass composite). All of the materials are elastic and the viscoelastic (time dependent) extension of the analytical model is not used. The material properties used for the die were $E = 163$ MPa, $\nu = 0.278$ and the properties for the underfill were $E = 5$ MPa, $\nu = 0.35$. E^* is given as 9.70238×10^{-3} from Equation 3-72 while using Equation 3-74 gives β as 0.304583. These values are used for all calculations of G_c using Equation 3-71.

All interfacial strength tests were performed at the die/underfill interface. Loading was created using increments of displacement applied to the test fixture. The resulting load value was visually monitored. Testing completed when a drop in the load was observed after an increase in displacement loading. Visual confirmation of crack propagation was performed using the SEM.

4.2.1. TEST NUMBER 1

The first specimen tested was end cracked and the load was applied using a three-point bend fixture. This was the only specimen tested under these conditions due to the difficulty in both creating the specimen and applying the loading.

The left image in Figure 4-1 shows the interface in the unloaded condition before testing begins while the right image is the last image captured before failure.

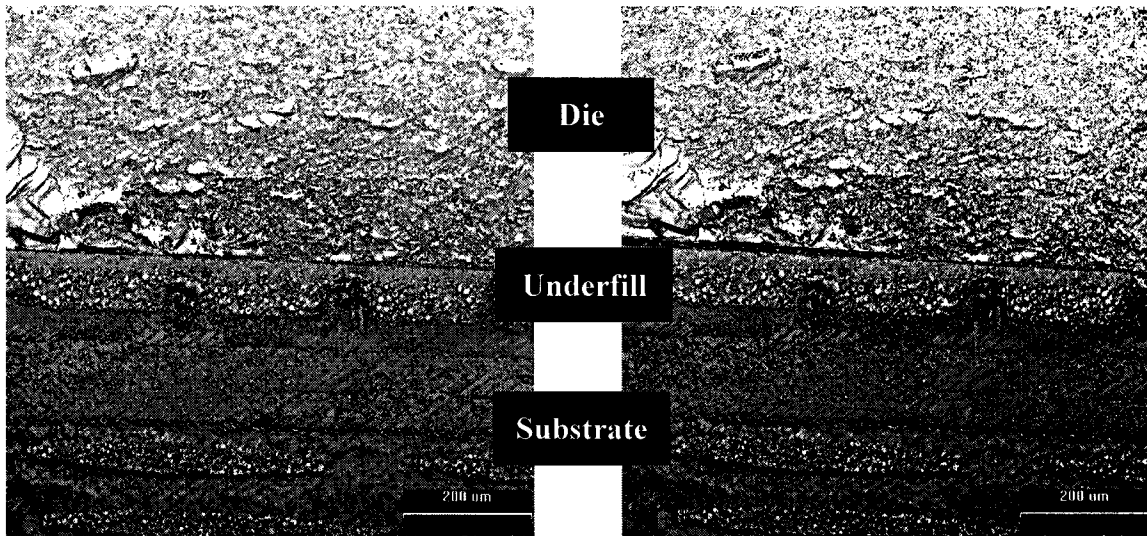


Figure 4-1: *An image pair from test number 1.*

The region where the digital image correlation was performed is shown by the dashed box in Figure 4-2. The interface between the die and the underfill is highlighted with a solid line and the crack tip location is indicated by the circle in the same figure.

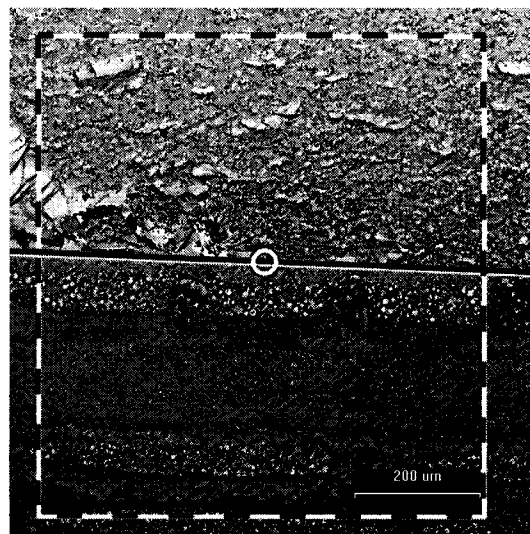


Figure 4-2: *Correlation boundary, interface and crack tip locations from test number 1.*

Node #	x coordinate (microns)	y coordinate (microns)	x displacement (microns)	y displacement (microns)
1	-181.76	8.96	-2.808E-03	2.691E-03
2	-181.76	-42.24	-3.368E-03	-6.001E-04
3	-181.76	-93.44	-1.649E-03	1.381E-03
4	-130.56	-93.44	-2.420E-03	1.434E-03
5	-66.56	-93.44	-1.349E-03	1.316E-03
6	-2.56	-93.44	-1.624E-03	5.532E-04
7	35.84	-93.44	-3.807E-03	3.755E-03
8	87.04	-93.44	-3.512E-03	1.958E-04
9	87.04	-42.24	-1.814E-03	-1.127E-04
10	87.04	-3.84	-2.050E-03	2.198E-03
11	87.04	47.36	-2.776E-03	2.202E-03
12	87.04	111.36	-1.744E-03	2.043E-03
13	35.84	111.36	1.748E-04	1.646E-03
14	-2.56	111.36	-2.054E-03	1.311E-03
15	-66.56	111.36	-1.542E-03	6.400E-04
16	-130.56	111.36	-2.657E-03	4.751E-03
17	-130.56	60.16	-2.212E-03	-3.099E-04
18	-130.56	8.96	-4.963E-04	4.882E-03

Table 4-1: Numeric values of relative boundary displacements from test number 1 used to perform analytical stress analysis.

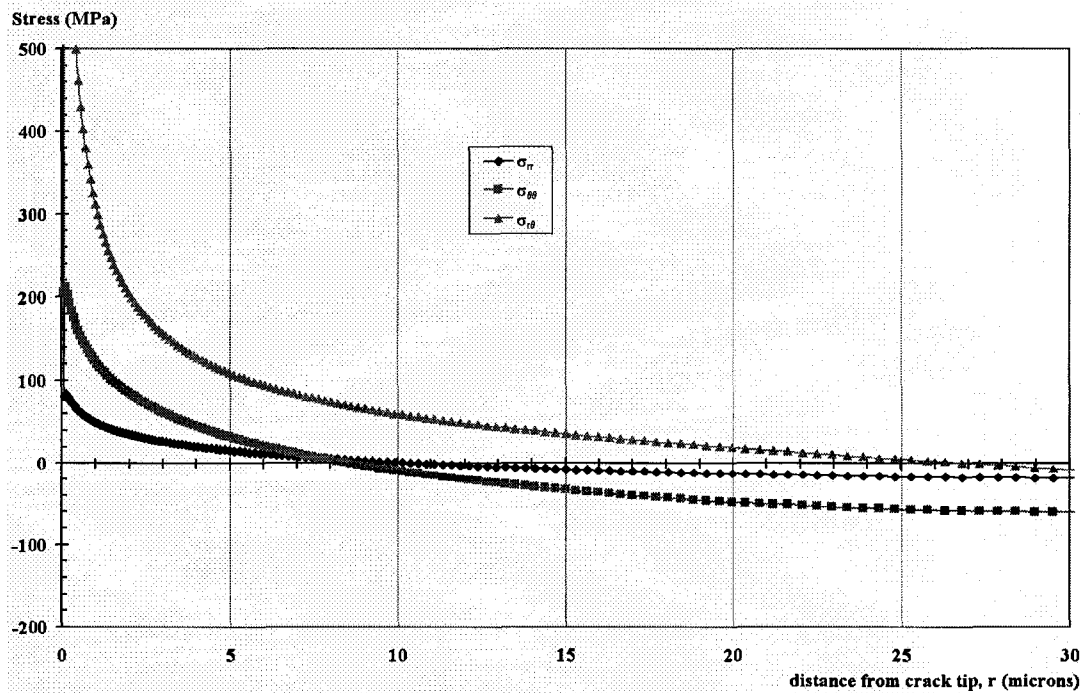


Figure 4-3: Interfacial stresses from analytical model for test number 1.

The stress intensity factors extracted were $K_I = 3.6804 \times 10^{-4} \text{ N}\sqrt{\mu\text{m}}/\mu\text{m}^2$ and $K_{II} = 8.1131 \times 10^{-4} \text{ N}\sqrt{\mu\text{m}}/\mu\text{m}^2$. Using Equation 3-71, G_c is found to be 74.2 J/m^2 .

This was the only successful test using an end cracked specimen in conjunction with the three-point bend fixture. Neither end cracked specimens nor the three-point bend fixture were used for the remaining tests due to the difficulties encountered. Creating an end notched specimen was difficult because the outer portion of the underfill had to be removed before the crack could be introduced. Also, the crack created was generally blunter than those created from center cracks.

The three-point bend fixture was replaced with the four-point bend setup when it was found that misalignment of the test specimen caused the tests to fail. The mode of these failures was crack propagation perpendicular to the interface instead of along the interface. In the few specimens where the middle load point was directly under the crack tip, failure occurred at an acute angle from the interface (with the exception of this specimen).

4.2.2. TEST NUMBER 2

The second specimen was loaded using the four-point bend fixture. The crack was created using the center notch method as explained in Chapter 2.

The left image in Figure 4-4 shows the interface in the unloaded condition before testing begins while the right image is the last image captured before failure.

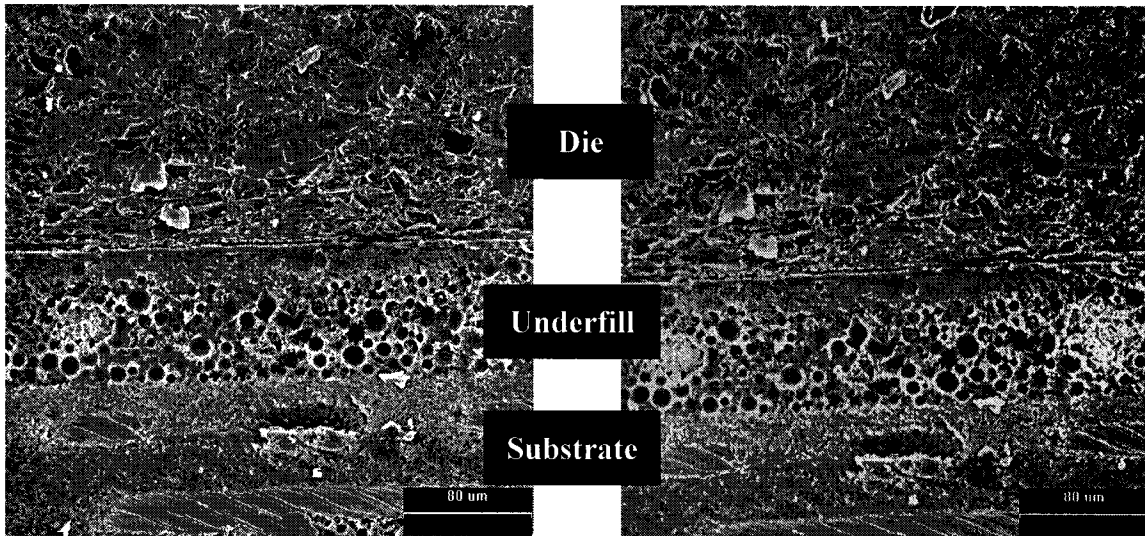


Figure 4-4: *An image pair from test number 2.*

The region where the digital image correlation was performed is shown by the dashed box in Figure 4-5. The interface between the die and the underfill is highlighted with a solid line and the crack tip location is indicated by the circle in the same figure.

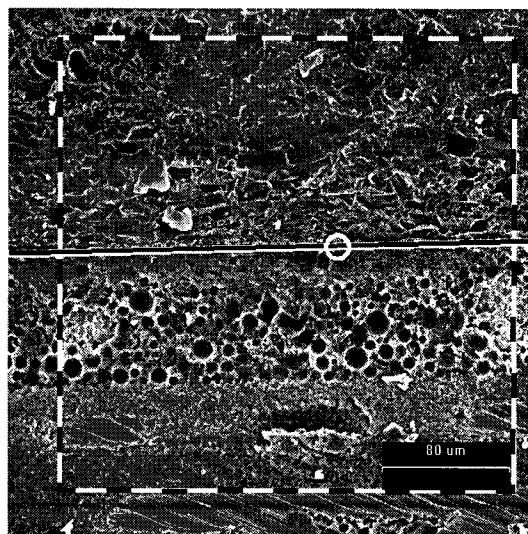


Figure 4-5: *Correlation boundary, interface and crack tip locations from test number 2.*

Node #	x coordinate (microns)	y coordinate (microns)	x displacement (microns)	y displacement (microns)
1	-47.104	2.048	-3.871E-04	3.013E-03
2	-47.104	-28.672	-1.731E-03	2.978E-03
3	-47.104	-57.344	-4.992E-03	2.602E-03
4	-20.480	-57.344	-4.459E-03	6.917E-04
5	4.096	-57.344	-3.982E-03	-7.665E-04
6	20.480	-57.344	-3.580E-03	-1.754E-03
7	40.960	-57.344	-3.071E-03	-2.965E-03
8	40.960	-28.672	-1.384E-03	-3.026E-03
9	40.960	-4.096	-3.694E-05	-2.560E-03
10	40.960	36.864	2.477E-03	-1.468E-03
11	40.960	63.488	3.394E-03	-1.257E-03
12	20.480	63.488	3.122E-03	-1.802E-04
13	4.096	63.488	3.003E-03	7.274E-04
14	-20.480	63.488	2.865E-03	2.346E-03
15	-40.960	63.488	2.484E-03	4.481E-03
16	-65.536	63.488	2.687E-03	5.532E-03
17	-65.536	36.864	1.865E-03	5.270E-03
18	-65.536	4.096	-1.879E-04	3.692E-03

Table 4-2: Numeric values of relative boundary displacements from test number 2 used to perform analytical stress analysis.

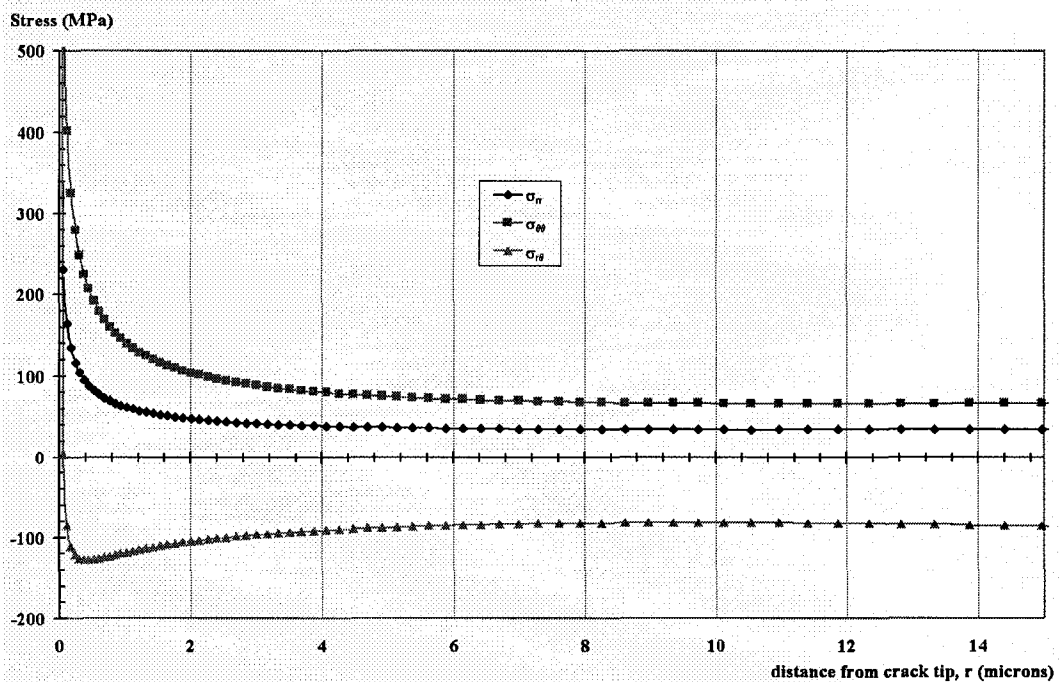


Figure 4-6: Interfacial stresses from analytical model for test number 2.

The stress intensity factors extracted were $K_I = 3.3235 \times 10^{-4} \text{ N}\sqrt{\mu\text{m}}/\mu\text{m}^2$ and $K_{II} = -9.6548 \times 10^{-4} \text{ N}\sqrt{\mu\text{m}}/\mu\text{m}^2$. Using Equation 3-71, G_c is found to be 97.5 J/m^2 .

Changing the load application method and the cracking technique created a sharper crack tip which is evident in the tightening of the singular stress region shown in Figure 4-6. The drawback of having a sharper crack tip is that accurate identification of the tip is difficult as compared to cases without a sharp crack tip. To locate the crack tip, loading was applied to the specimen, but not enough for failure. The mouth of the crack was then located at the center notch region and traced manually on the SEM under high magnification. Once the tip was located, it was centered on the screen and the magnification level reduced. The reduction in magnification level was to insure that sufficient data ahead of the crack tip was captured on the image to allow definition of a finite region for the analytical model. When the crack tip was located and the first reference image captured, the pixel coordinates of the crack tip were recorded to make identification of the location possible after testing was complete.

A second issue was that the crack propagation could not be confirmed visually as the test was underway because failure along the interface was not as dramatic as that seen with the end cracked specimen under three-point loading. Thus, failures were detected by examining the area under higher magnification between load applications and also by monitoring for sudden changes in the load on the test fixture as the anvils were moved together. A slight drop in the load as the anvils moved together was due to a loss in

stiffness in the specimen caused by cracking. Since the test region was not the only location that may experience crack propagation, visual inspection under higher magnification was necessary to confirm that the crack in the test region was where the failure had occurred.

4.2.3. TEST NUMBER 3

The third specimen was loaded using the four-point bend fixture. The crack was created using the center scribe method.

The left image in Figure 4-7 shows the interface in the unloaded condition before testing begins while the right image is the last image captured before failure.

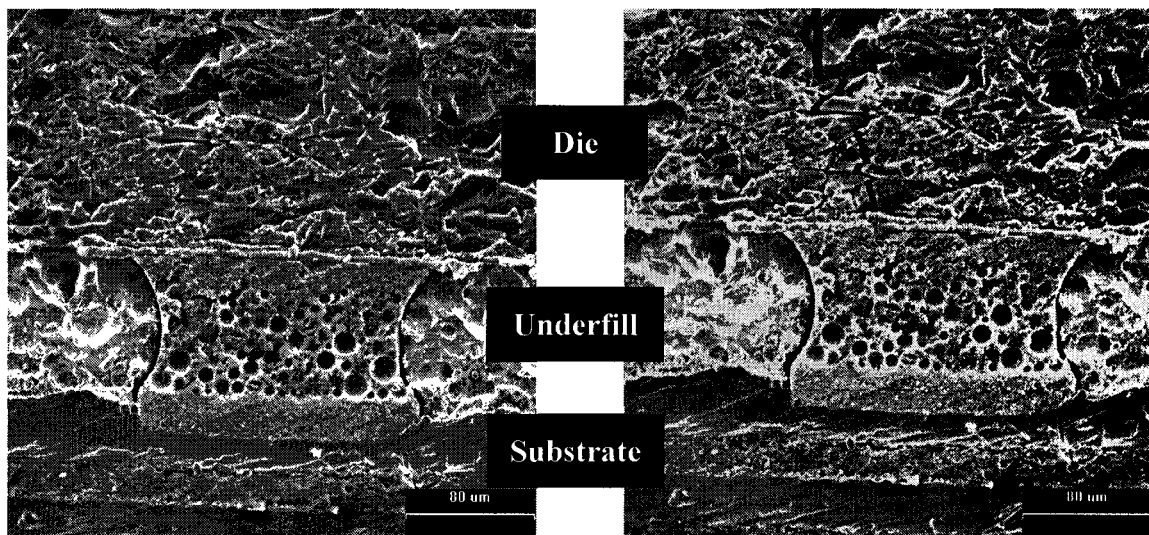


Figure 4-7: *An image pair from test number 3.*

The region where the digital image correlation was performed is shown by the dashed box in Figure 4-8. The interface between the die and the underfill is highlighted with a solid line and the crack tip location is indicated by the circle in the same figure.

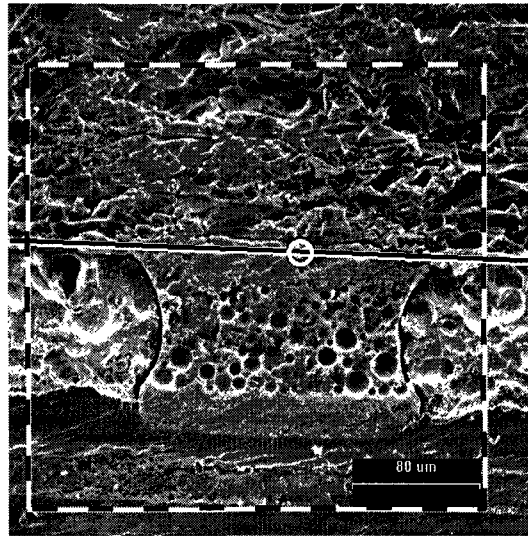


Figure 4-8: Correlation boundary, interface and crack tip locations from test number 3.

Node #	x coordinate (microns)	y coordinate (microns)	x displacement (microns)	y displacement (microns)
1	-18.43	-2.05	-1.135E-04	-2.381E-04
2	-18.43	-26.62	1.080E-03	-4.188E-04
3	-18.43	-47.10	1.723E-03	-7.447E-04
4	0.00	-47.10	2.003E-03	-4.334E-04
5	22.53	-47.10	3.669E-03	-2.964E-04
6	47.10	-47.10	3.998E-03	4.630E-04
7	47.10	-24.58	3.958E-03	1.429E-03
8	47.10	2.05	2.154E-03	1.519E-04
9	47.10	26.62	-4.925E-04	1.665E-03
10	47.10	51.20	-7.940E-04	2.023E-03
11	22.53	51.20	-1.152E-03	1.674E-03
12	0.00	51.20	-1.494E-03	1.254E-03
13	-16.38	51.20	-1.567E-03	9.692E-04
14	-32.77	51.20	-1.668E-03	6.297E-04
15	-32.77	26.62	-1.132E-03	4.018E-05
16	-32.77	-2.05	-4.149E-04	-5.923E-04

Table 4-3: Numeric values of relative boundary displacements from test number 3 used to perform analytical stress analysis.

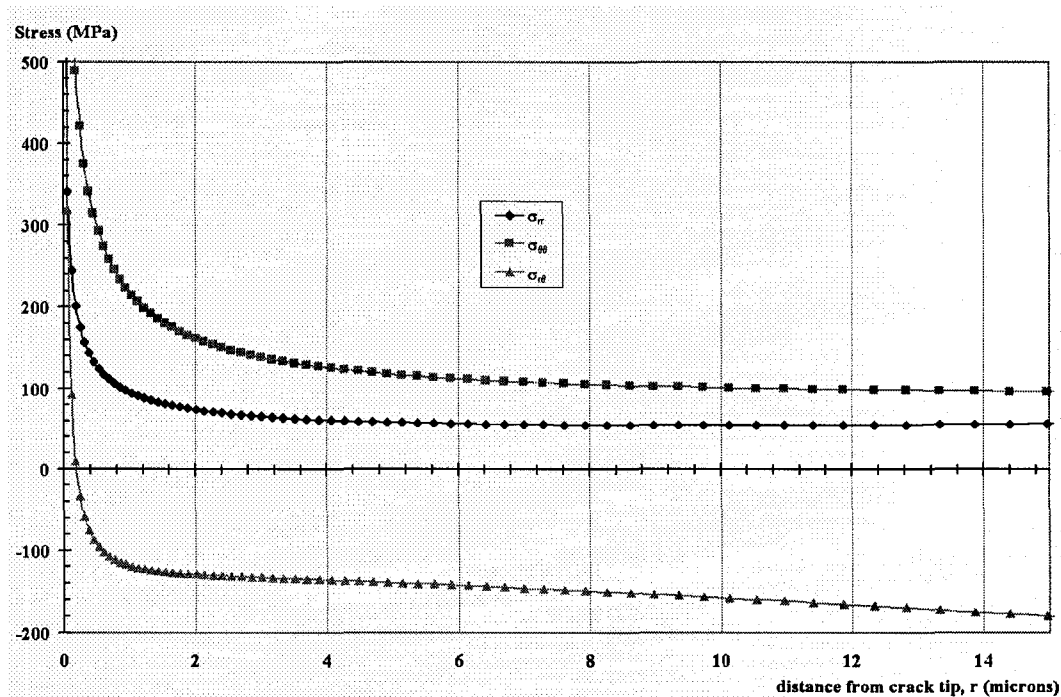


Figure 4-9: *Interfacial stresses from analytical model for test number 3.*

The stress intensity factors extracted were $K_I = 5.0788 \times 10^{-4} \text{ N}\sqrt{\mu\text{m}}/\mu\text{m}^2$ and $K_{II} = -8.3504 \times 10^{-4} \text{ N}\sqrt{\mu\text{m}}/\mu\text{m}^2$. Using Equation 3-71, G_c is found to be 89.3 J/m^2 .

The creation of the crack tip using the scribe technique yielded mixed results. Creation of test specimens became easier because a notch did not have to be created but the cracks created traveled vertically before turning at the interface, causing a few difficulties. First, if the crack traveled straight down, then it was not possible to use the specimen since the crack axis had to be along the interface. Second, the crack had to travel far enough along the interface to ensure that there was enough area behind the crack tip for the finite region to encompass only that portion of the crack that was along the interface.

4.2.4. TEST NUMBER 4

The fourth specimen was loaded using the four-point bend fixture. The crack was created using the center scribe method.

The left image in Figure 4-10 shows the interface in the unloaded condition before testing begins while the right image is the last image captured before failure.

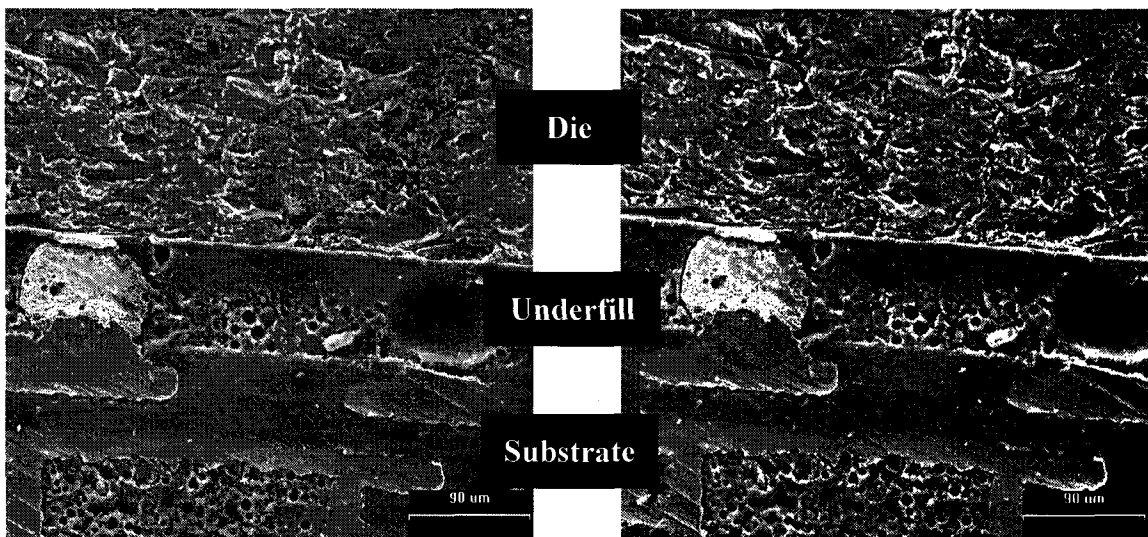


Figure 4-10: *An image pair from test number 4.*

The region where the digital image correlation was performed is shown by the dashed box in Figure 4-11. The interface between the die and the underfill is highlighted with a solid line and the crack tip location is indicated by the circle in the same figure.

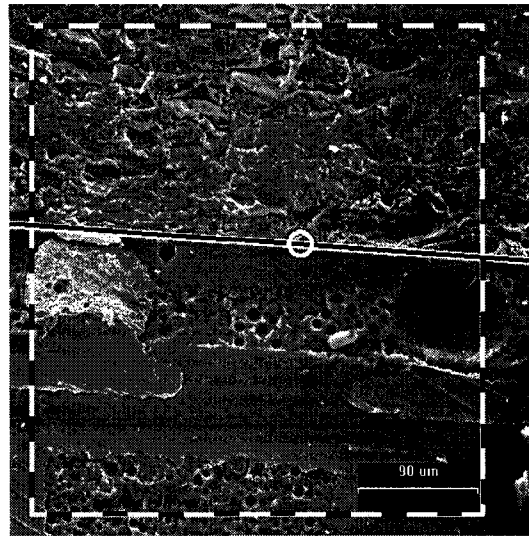


Figure 4-11: Correlation boundary, interface and crack tip locations from test number 4.

Node #	x coordinate (microns)	y coordinate (microns)	x displacement (microns)	y displacement (microns)
1	-65.90	-7.32	-2.440E-03	-1.702E-03
2	-65.90	-41.49	-1.020E-03	-1.438E-03
3	-65.90	-85.42	1.291E-04	-1.550E-03
4	-34.17	-85.42	7.183E-04	-7.724E-04
5	0.00	-85.42	1.549E-03	-3.508E-05
6	41.49	-85.42	2.372E-03	1.462E-03
7	85.42	-85.42	3.572E-03	2.512E-03
8	85.42	-41.49	2.689E-03	2.553E-03
9	85.42	7.32	1.513E-03	2.614E-03
10	85.42	41.49	1.145E-03	2.929E-03
11	85.42	85.42	8.809E-04	3.298E-03
12	41.49	85.42	5.595E-04	1.652E-03
13	0.00	85.42	-5.022E-03	2.414E-03
14	-34.17	85.42	-5.291E-03	1.153E-03
15	-82.98	85.42	-5.809E-03	-3.104E-04
16	-82.98	41.49	-4.545E-03	-1.441E-03
17	-82.98	-4.88	-3.128E-03	-2.441E-03

Table 4-4: Numeric values of relative boundary displacements from test number 4 used to perform analytical stress analysis.

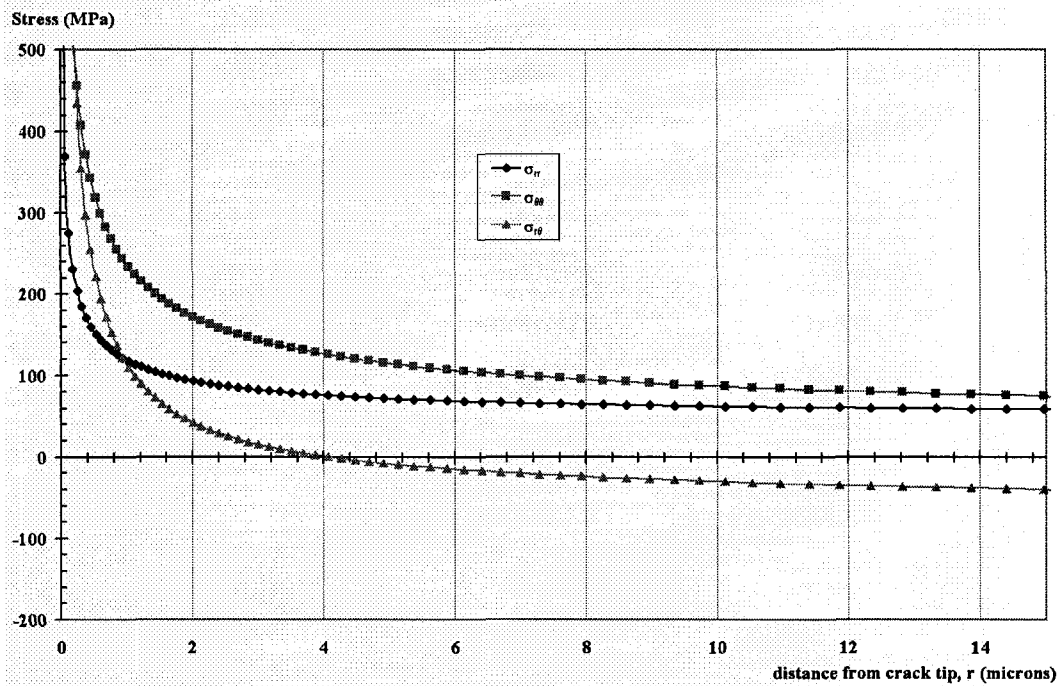


Figure 4-12: Interfacial stresses from analytical model for test number 4.

The stress intensity factors extracted were $K_I = 5.8139 \times 10^{-4} \text{ N}\sqrt{\mu\text{m}}/\mu\text{m}^2$ and $K_{II} = 9.0331 \times 10^{-4} \text{ N}\sqrt{\mu\text{m}}/\mu\text{m}^2$. Using Equation 3-71, G_c is found to be 107.9 J/m^2 .

As observed with the previous center scribe specimen, the crack moved down to the interface close to the test region, but did so at a shallower angle.

4.2.5. TEST NUMBER 5

The fifth specimen was loaded using the four-point bend fixture. The crack was created using the center notch method.

The left image in Figure 4-13 shows the interface in the unloaded condition before testing begins while the right image is the last image captured before failure.

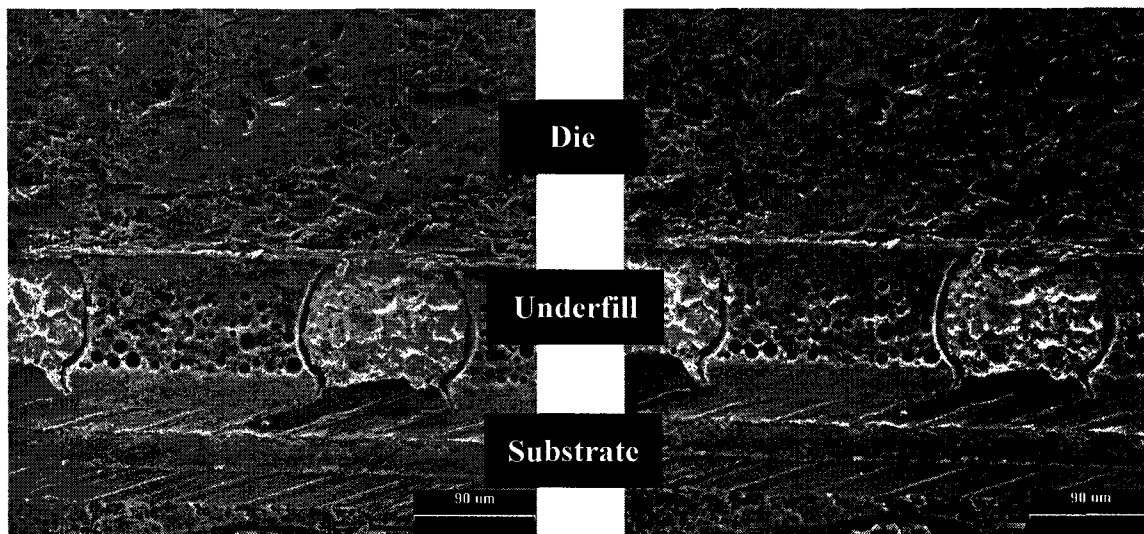


Figure 4-13: *An image pair from test number 5.*

The region where the digital image correlation was performed is shown by the dashed box in Figure 4-14. The interface between the die and the underfill is highlighted with a solid line and the crack tip location is indicated by the circle in the same figure.

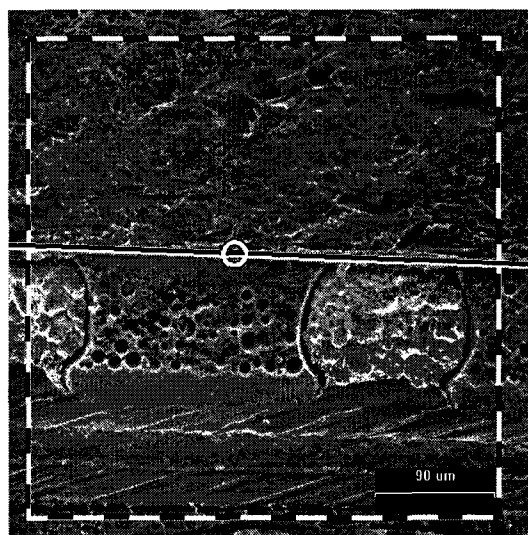


Figure 4-14: *Correlation boundary, interface and crack tip locations from test number 5.*

Node #	x coordinate (microns)	y coordinate (microns)	x displacement (microns)	y displacement (microns)
1	73.22	2.44	6.913E-04	-8.992E-04
2	73.22	-41.49	-6.123E-04	-1.100E-03
3	73.22	-85.42	-2.526E-03	-1.356E-03
4	41.49	-85.42	-2.767E-03	-9.769E-04
5	0.00	-85.42	-3.443E-03	-6.471E-04
6	-51.25	-85.42	-4.127E-03	-1.132E-04
7	-100.07	-85.42	-5.684E-03	-4.553E-04
8	-100.07	-41.49	-4.160E-03	-5.586E-04
9	-100.07	-2.44	-8.335E-04	1.871E-03
10	-100.07	41.49	8.676E-05	2.101E-03
11	-100.07	85.42	5.882E-04	2.184E-03
12	-51.25	85.42	5.527E-04	1.699E-03
13	0.00	85.42	1.565E-03	8.306E-04
14	61.02	85.42	1.851E-03	2.882E-04
15	61.02	41.49	1.509E-03	-1.426E-04
16	61.02	2.44	6.282E-04	-7.979E-04

Table 4-5: Numeric values of relative boundary displacements from test number 5 used to perform analytical stress analysis.

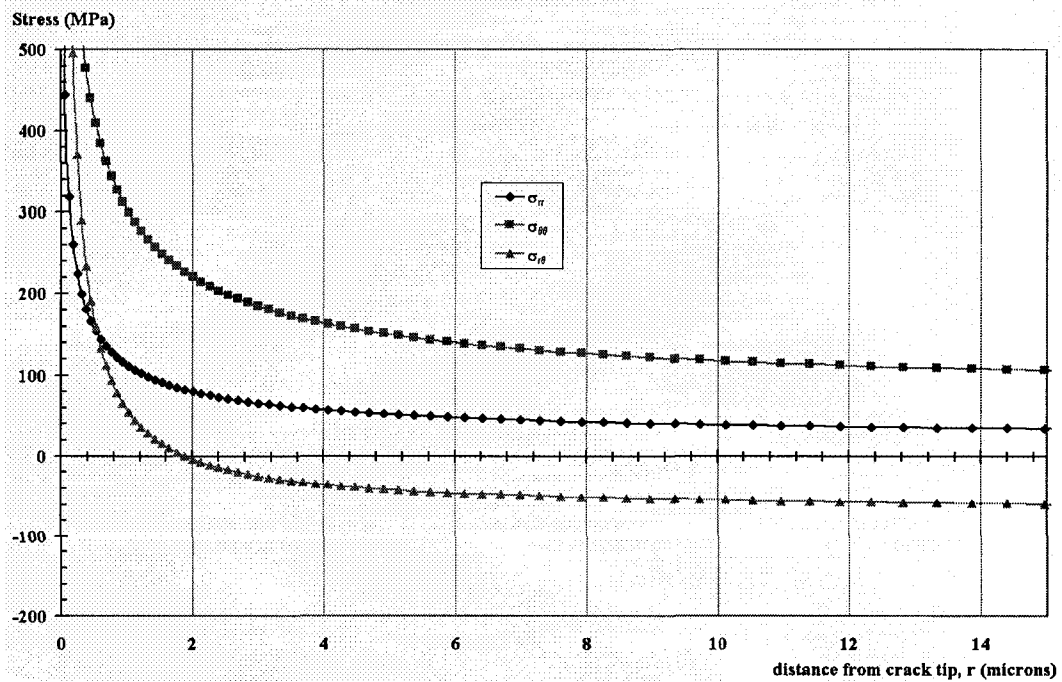


Figure 4-15: Interfacial stresses from analytical model for test number 5.

The stress intensity factors extracted were $K_I = 7.3814 \times 10^{-4} \text{ N}\sqrt{\mu\text{m}}/\mu\text{m}^2$ and $K_{II} = 4.1307 \times 10^{-4} \text{ N}\sqrt{\mu\text{m}}/\mu\text{m}^2$. Using Equation 3-71, G_c is found to be 66.9 J/m^2 .

Test 5 was the only specimen that showed stronger Mode I behavior than Mode II and also reported the lowest value for the critical energy release rate. The crack tip used for this test was far from the center notch and close to the location of the inner four-point loading anvil. The inner loading points of the four-point fixture used were spaced further apart than those found on standard fixtures in order to place the loading points near the edges of the die to maximize the working area during testing. This combined with the center region of the specimen being stiffer than the outer portions because of the die created more curvature near the loading points than that found near the center of the specimen. This may account for the different behavior observed during the test. Since both materials along the interface are brittle, it is expected that the interface would tend to be more sensitive to strong opening mode loads. Thus, the failure of the interface at a load lower than the other specimens is reasonable.

4.2.6. TEST NUMBER 6

The sixth specimen was loaded using the four-point bend fixture. The crack was created using the center notch method.

The left image in Figure 4-16 shows the interface in the unloaded condition before testing begins while the right image is the last image captured before failure.

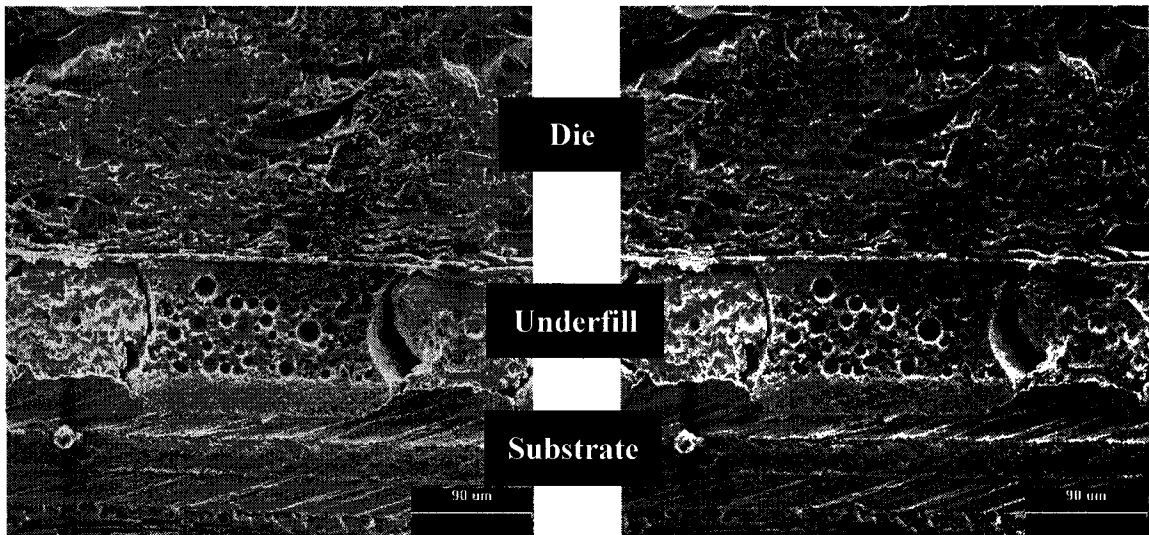


Figure 4-16: *An image pair from test number 6.*

The region where the digital image correlation was performed is shown by the dashed box in Figure 4-17. The interface between the die and the underfill is highlighted with a solid line and the crack tip location is indicated by the circle in the same figure.

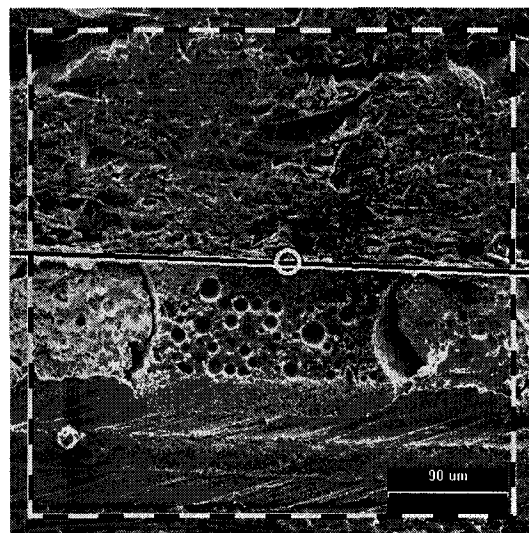


Figure 4-17: *Correlation boundary, interface and crack tip locations from test number 6.*

Node #	x coordinate (microns)	y coordinate (microns)	x displacement (microns)	y displacement (microns)
1	-39.05	0.00	-3.8621E-04	2.1143E-03
2	-39.05	-26.85	-1.8467E-03	1.7911E-03
3	-39.05	-51.25	-3.2377E-03	1.5598E-03
4	0.00	-51.25	-2.6720E-03	-3.1244E-04
5	24.41	-51.25	-2.5196E-03	-1.9312E-03
6	51.25	-51.25	-1.8213E-03	-3.2233E-03
7	51.25	-26.85	-7.9763E-04	-2.8219E-03
8	51.25	2.44	1.2113E-03	-2.7216E-03
9	51.25	26.85	1.7725E-03	-2.1186E-03
10	51.25	51.25	3.0840E-03	-1.7706E-03
11	24.41	51.25	2.6053E-03	-3.6798E-04
12	0.00	51.25	1.9807E-03	9.4871E-04
13	-24.41	51.25	1.6965E-03	2.4288E-03
14	-51.25	51.25	1.6452E-03	3.8704E-03
15	-51.25	26.85	4.9559E-04	3.7279E-03
16	-51.25	0.00	-4.6407E-04	2.8675E-03

Table 4-6: Numeric values of relative boundary displacements from test number 6 used to perform analytical stress analysis.

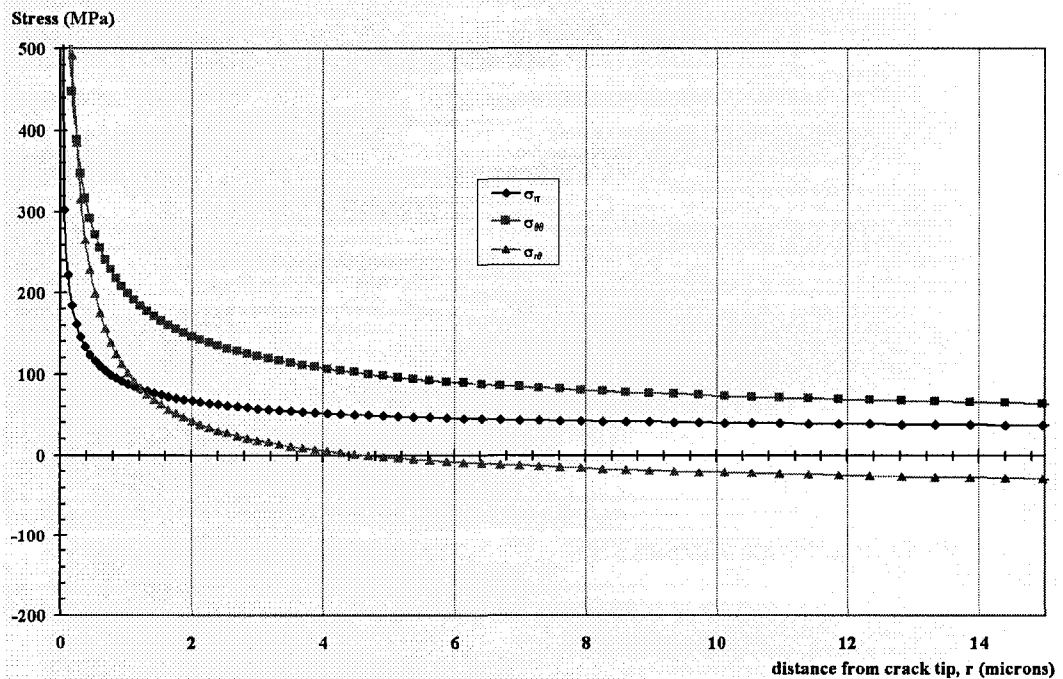


Figure 4-18: Interfacial stresses from analytical model for test number 6.

The stress intensity factors extracted were $K_I = 4.9727 \times 10^{-4} \text{ N}\sqrt{\mu\text{m}} / \mu\text{m}^2$ and $K_{II} = 8.2780 \times 10^{-4} \text{ N}\sqrt{\mu\text{m}} / \mu\text{m}^2$. Using Equation 3-71, G_c is found to be 87.2 J/m^2 .

4.2. Summary of Critical Stress Intensity Factors

Numeric values of the critical stress intensity factors are given in Table 4-7 and are plotted in Figure 4-19. Note that the magnitude of the Mode II values is shown in Figure 4-19 for clarity. The stress intensity factors show a trend of Mode II dominance from the test results with the exception of test number 5. The relative stability of the values even though the crack introduction and loading methods were not identical is due to the localized nature of the measurements. Some of the variation, especially with the fifth specimen, can be attributed to using a bend fixture for the load application. Possible methods to reduce these fluctuations are discussed in Chapter 5.

Test Number	$K_I,$ $\text{N}\sqrt{\mu\text{m}} / \mu\text{m}^2$	$K_{II},$ $\text{N}\sqrt{\mu\text{m}} / \mu\text{m}^2$	$\text{MAG}(K_{II}),$ $\text{N}\sqrt{\mu\text{m}} / \mu\text{m}^2$
1	3.68E-04	8.11E-04	8.11E-04
2	3.32E-04	-9.65E-04	9.65E-04
3	5.08E-04	-8.35E-04	8.35E-04
4	5.81E-04	9.03E-04	9.03E-04
5	7.38E-04	4.13E-04	4.13E-04
6	4.97E-04	8.28E-04	8.28E-04

Table 4-7: Numeric values of critical stress intensity factors.

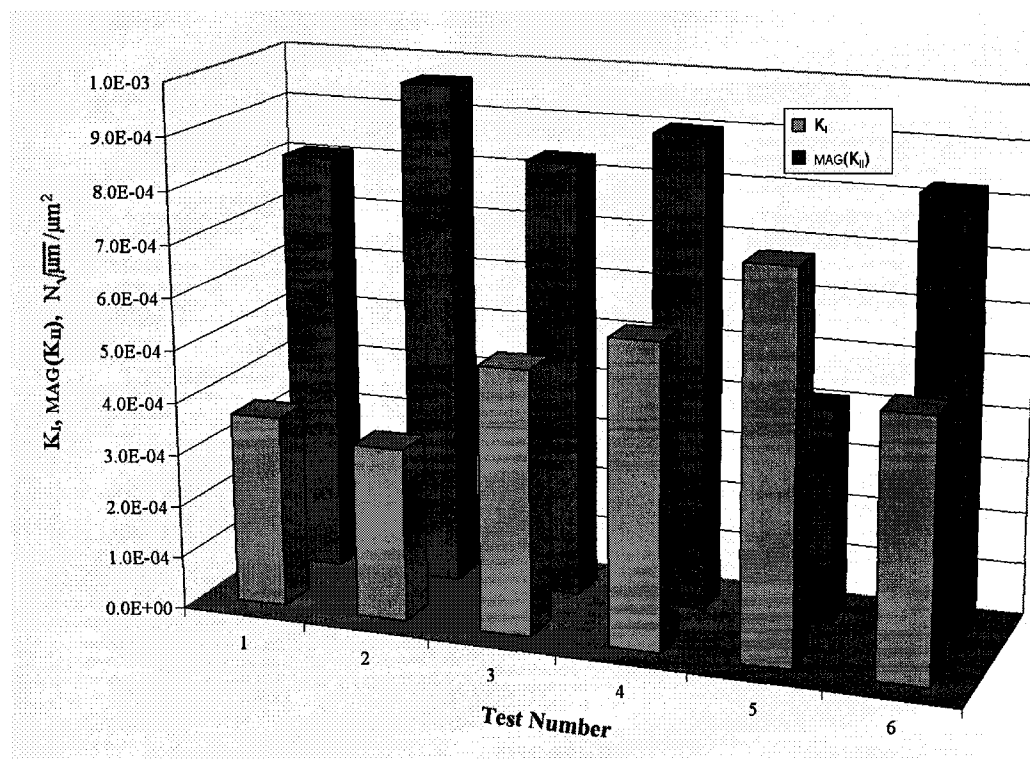


Figure 4-19: Summary of critical stress intensity factors.

4.3. Summary of Critical Energy Release Rates

The variations seen in the stress intensity factors are not reflected in the critical energy release rate values summarized in Table 4-8 and Figure 4-20. In fact, the values vary from the mean one-fourth the amount than that of the stress intensity factors. The mean value of G_c computed using equations 4-1 through 4-3 (identical to 3-71, 3-72, and 3-74, respectively) is 87.2 J/m 2 and the largest deviations from this are 23.8% (specimen 4) and -23.3% (specimen 5).

$$G = \frac{1 - \beta^2}{E_*} (K_I^2 + K_{II}^2) \tag{4-1}$$

where:

$$\frac{1}{E_*} = \frac{1}{2} \left(\frac{1}{E_1} + \frac{1}{E_2} \right) \tag{4-2}$$

$$\beta = \frac{1}{2} \frac{\mu_1(1-2\nu_2) - \mu_2(1-2\nu_1)}{\mu_1(1-\nu_2) + \mu_2(1-\nu_1)} \tag{4-3}$$

Test Number	$G_c, J/m^2$
1	74.2
2	97.5
3	89.3
4	107.9
5	66.9
6	87.2

Table 4-8: Numeric values of critical energy release rate.

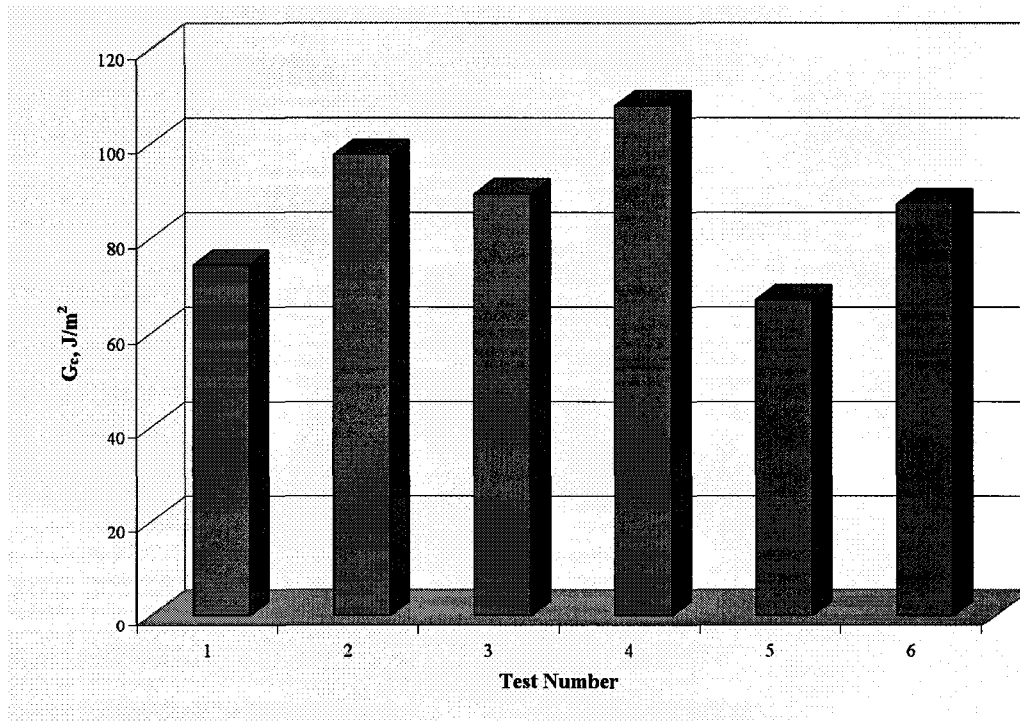


Figure 4-20: Summary of critical energy release rates.

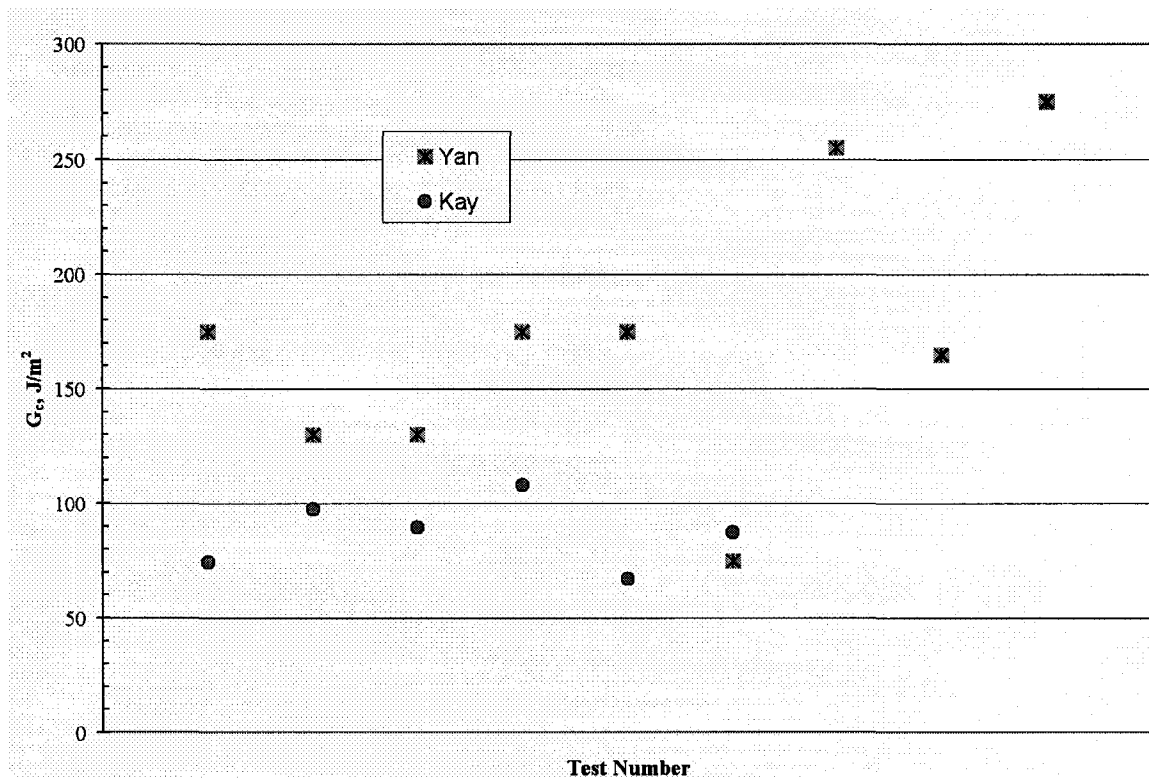


Figure 4-21: Comparison of current study results to Yan (1998).

Yan (1998) investigated the interfacial strength of specimens he created to mimic the components found in electronic packages. Similar to the current study, a crack was introduced along the interface and the specimen subjected to a bending load, which in Yan's case was using a four-point bend test fixture. The critical energy release rates were calculated by means of J-Integrals based on the load-displacement data from the tests. Yan also looked at the behavior of different specimens as he changed the materials and the techniques used to fabricate them. The results of his work for die/underfill interfaces are compared to the values obtained in this study in Figure 4-21.

The large variation in the values obtained by Yan is because each of his data points are for a different combination of three die passivation and four underfill materials giving a total of 12 data points. Because the materials in the packages used to create the specimens for this study are unknown, it is not possible to compare directly to Yan's configuration that best matches the packages used in this work. Even so, the comparison of the data points is good. The lower values obtained in this study are most likely a combination of how the specimens were created and the methods used to determine G_c . Using post-production packages will generally result in specimens that are weaker than those custom made specifically for testing. As discussed in Chapter 1, using the experimental J-Integral based on load-displacement curves assumes that all the energy introduced into the system is used entirely at the crack tip. Because this is usually not true, the values returned from experimental J-Integrals will be higher than the true values. Thus, the values from the current study would be expected to be lower than those found by Yan. Since a majority of Yan's values are not much larger than those found in this study, the results are considered a good match.

4.4. Summation

The work resulted in six tests where the critical energy release rate for the die/underfill interface was determined. The mean value of the interfacial strength is 87.2 J/m^2 with a variation less than 25%. Having these values with the same order of magnitude reflects the robustness of this technique. Taking into consideration the variation inherently present in the experimental work and that the critical energy release rate is dependent on the square of the stress intensity factors, these results are an achievement. Comparison

against published results for these values is also favorable when differences in specimen and testing methods are included.

5. CLOSING REMARKS

In this dissertation, a new technique is developed for determining the strength of the dissimilar material interfaces in electronic packages using a combination of experimental and analytical methods. Previous methods for interfacial strength determination used specimens fabricated specifically for testing. However, in the present study specimens were created from actual packages in order to gain a better understanding of the strength of post-production packages. Creating test specimens from actual packages required the development of novel sample preparation techniques for the sectioning of electronic packages. Because the bare packages cannot be sectioned without introducing severe damage, methods for removable encapsulation were developed to support the package during sectioning. The three techniques developed allow for specimens to be created from a wide variety of electronic packages.

The final step of the specimen preparation is the introduction of a crack to the interface of interest. Two methods were used for the crack introduction. The first method, based on a technique described by Cao (1989), scribes a line on the top surface of the die. The package is then subjected to three-point bending causing the cracks to propagate from the scribe down to the interface. This technique is the quickest way to create interfacial cracks but involves difficulty in controlling the location of the crack tip. In addition, failure of the substrate commonly occurs as the crack is propagated down to the interface.

Lastly, forming a useable crack surface along the interface before failure occurs in the specimen at other locations is a challenging task.

The second method of crack introduction involves cutting a notch into the die to replicate test specimens commonly used under four-point bending to determine interfacial strengths. The notch method requires another cycle of covering with Con-Tact paper, encapsulation, cutting, and matrix removal that is not necessary with the scribe technique. The benefit of this additional work is that the cracks initiate much closer to the interface than those created from scribe lines. These cracks travel nearly parallel to the interface, making creation of crack surface along the interface much easier. Consequently, the notch method is the preferred method for crack introduction.

For the testing procedure, the load was initially applied using a three-point bend fixture. Following a series of specimen failures in directions other than along the interface, the loading method was replaced with a four-point bend fixture. Failure rates outside of the test region were reduced but the number of specimens that failed in modes other than the desired mode was still high. Alternative load application methods would be an area of investigation for future research work. One concept would be the development of a new testing fixture that used single cantilever loading on the specimen. If the center portion of the specimen was fixed to prevent bending of the die and a load applied on the substrate such that the substrate is bent away from the die, then end cracks could be driven along the interface with less chance of brittle failure of the die. End cracks allow

for both the die/underfill and underfill/substrate interfaces to be investigated. Center cracks do not allow for this underfill/substrate investigation since the crack is driven down through the die to the underfill layer.

The method for image acquisition using the scanning electron microscope was sufficient for the material tested but would be inadequate for materials with rapidly changing material properties. By its nature, the SEM scans the specimen to create an image line by line. If the material properties changed on a time scale similar to that of the SEM scan time, then the top of the image would be for a material with different properties than the bottom. For applications involving these types of materials, imaging equipment that could capture the entire specimen simultaneously would be needed. Optical microscopes using digital cameras would be able to accomplish this. The drawback would be the severe loss in the depth of field in the image inherent with optical microscopes. Any misalignment of the specimen would create areas that were out of focus. Even so, given the distinct advantages available, future work would best be performed using high power optical microscopes (magnifications of 500x or more) in conjunction with digital imaging equipment. Optical imaging would also allow for thermal loading tests to be performed that are not possible in the vacuum of the SEM chamber.

Digital image correlation is an area of optical research that is still in the developmental stage. Because of the immaturity of the field, nearly all of the work done in industry is through custom programming for a specific task, leaving few commercial packages

available for end users. The software that was used for this study performed the correlation itself admirably, but the pre-processing component was surprisingly difficult for a commercial software package and would be impossible to automate. For example, image registration would have made alignment of the images a simple task during the pre-processing stage and made automation a possibility, but this commonly used technique was not incorporated into the software package. Thus, while the time investment required to generate custom code would be large, it may be necessary for many projects requiring correlation of images.

The concept of determining properties of materials from post-production samples has been shown to be feasible. Use of digital image correlation reduces the error created by using measurement of quantities far away from the test region to estimate what is occurring at the area of interest. The creation of an analytical model to better capture the stresses near a singular point also reduces the error associated with using traditional finite element analysis at regions with high stress gradients. Reporting the interfacial strength as a critical stress intensity factor limits the usefulness of the results because these values are dependent on the loading conditions. Since the critical energy release rate is not dependent on loading, using it when reporting interface strengths provides results useful for a wider range of applications.

APPENDICES

APPENDIX A

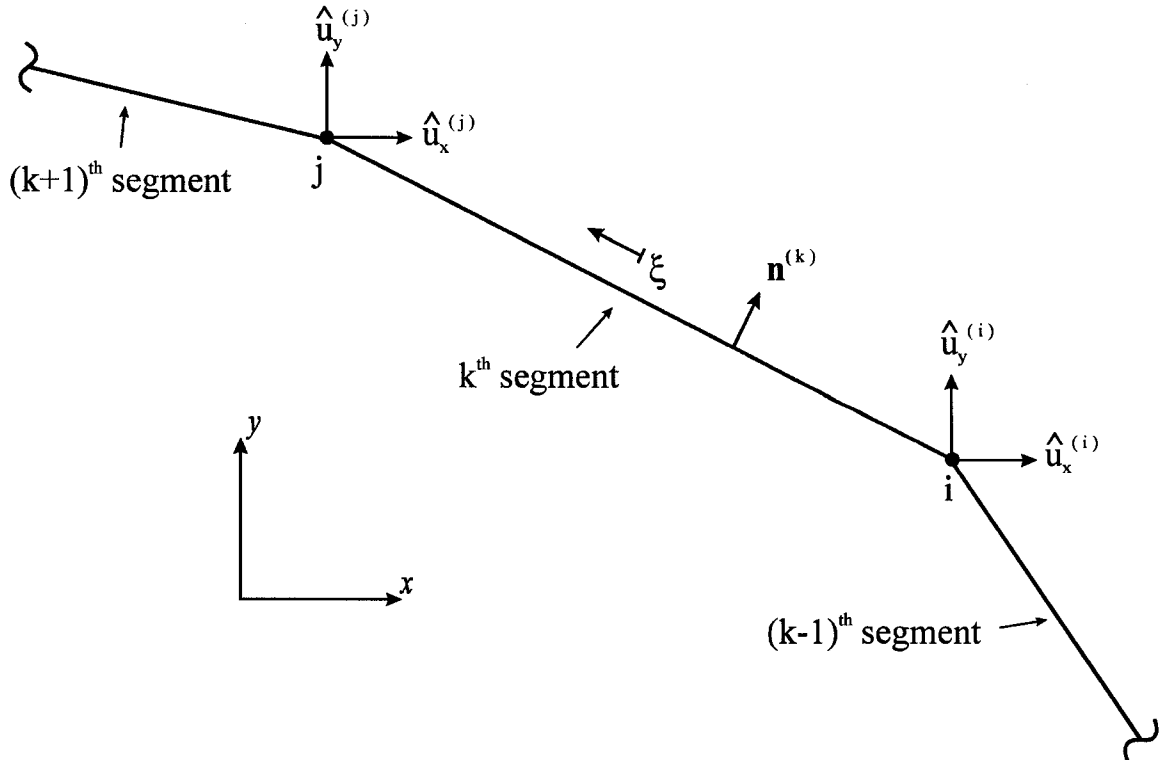


Figure A-1: Description of a boundary segment.

A typical boundary configuration near the k^{th} boundary segment, connecting the i^{th} and j^{th} collocation points (joints), is shown in Figure A-1. In order to approximate the displacement variations between these collocation points, a line coordinate ξ is introduced with the origin located at the midpoint of the k^{th} boundary segment. The positive direction of ξ follows the counter-clockwise ordering of the i^{th} and j^{th} joints as depicted in Figure A-1. Along the k^{th} boundary segment, the line coordinate ξ varies linearly such that it becomes -1 at the i^{th} joint and 1 at the j^{th} joint. In addition, the displacements in the Cartesian reference frame at the i^{th} and j^{th} collocation joints are represented by $(\hat{u}_x^{(i)}, \hat{u}_y^{(i)})$ and $(\hat{u}_x^{(j)}, \hat{u}_y^{(j)})$, respectively.

The variations of the displacements along the k^{th} boundary segment between the collocation points i and j are approximated globally in terms of the displacements of all the collocation points contained in the vector $\hat{\mathbf{v}}$ as

$$\hat{\mathbf{U}}^{(k)} = \mathbf{\Lambda}^{(k)} \hat{\mathbf{v}}$$

where

$$\hat{\mathbf{U}}^{(k)} = \left\{ \hat{u}_x^{(k)} \quad \hat{u}_y^{(k)} \right\}^T$$

and

$$\mathbf{\Lambda}^{(k)} = \begin{bmatrix} 0 & \cdots & 0 & N_i & 0 & 0 & \cdots & 0 & N_j & 0 & 0 & \cdots & 0 \\ 0 & \cdots & 0 & 0 & N_i & 0 & \cdots & 0 & 0 & N_j & 0 & \cdots & 0 \end{bmatrix}$$

$\underbrace{\hspace{10em}}_{i^{\text{th}} \text{ block}} \qquad \underbrace{\hspace{10em}}_{j^{\text{th}} \text{ block}}$

in which the linear interpolation functions, N_i and N_j , are defined in terms of the line coordinate, ξ , as

$$N_i = \frac{1}{2}(1-\xi), \quad N_j = \frac{1}{2}(1+\xi)$$

The matrix $\mathbf{\Lambda}^{(k)}$ is constructed such that only the displacements at the i^{th} and j^{th} collocation points in vector $\hat{\mathbf{v}}$ are effective in describing the linear variations of the boundary displacements along the k^{th} boundary segment.

APPENDIX B

node #	pos_x (pixels)	pos_y (pixels)	u_x (pixels)	u_y (pixels)	u (pixels)	rotation (rad)
8222	35.2	163.2	-1.3705E-03	-1.5434E-02	1.5495E-02	-4.016E-02
8223	38.4	163.2	-1.4255E-03	-1.5534E-02	1.5599E-02	-4.606E-02
8224	41.6	163.2	-1.5457E-03	-1.5684E-02	1.5760E-02	-5.774E-02
8225	44.8	163.2	-1.6146E-03	-1.5655E-02	1.5738E-02	-7.159E-02
8226	48.0	163.2	-1.6059E-03	-1.5439E-02	1.5522E-02	-9.056E-02
8227	51.2	163.2	-1.5187E-03	-1.5164E-02	1.5240E-02	-1.035E-01
8228	54.4	163.2	-1.3950E-03	-1.4877E-02	1.4942E-02	-9.622E-02
8229	57.6	163.2	-1.3898E-03	-1.4567E-02	1.4633E-02	-7.615E-02
8230	60.8	163.2	-1.4480E-03	-1.4260E-02	1.4333E-02	-6.054E-02
8231	64.0	163.2	-1.4678E-03	-1.3897E-02	1.3974E-02	-7.105E-02
8232	67.2	163.2	-1.4639E-03	-1.3377E-02	1.3457E-02	-1.118E-01
8233	70.4	163.2	-1.3710E-03	-1.2818E-02	1.2891E-02	-1.154E-01
8234	73.6	163.2	-1.1923E-03	-1.2406E-02	1.2464E-02	-5.818E-02
16181	259.2	320.0	-7.0806E-03	2.6124E-03	7.5472E-03	-4.418E-02

Table B-1: Sample of output data from digital image correlation program.

pos_x	X coordinate of node on reference image
pos_y	Y coordinate of node on reference image
u_x	X displacement of node from reference image position to object image position
u_y	Y displacement of node from reference image position to object image position
 u 	Magnitude of nodal displacement from reference image position to object image position
rotation	Angle of nodal rotation from reference image orientation to object image orientation

Table B-2: Definition of DIC result parameters.

A sample of the raw data returned from the digital image correlation software is show in Table B-1. The last row in Table B-1 corresponds to the results for the node closest to the crack tip. The table headings in Table B-1 are explained further in Table B-2.

node #	pos_x (microns)	pos_y (microns)	u_x (microns)	u_y (microns)	u (microns)
8222	22.53	104.45	-8.7709E-04	-9.8776E-03	9.9165E-03
8223	24.58	104.45	-9.1230E-04	-9.9418E-03	9.9836E-03
8224	26.62	104.45	-9.8926E-04	-1.0038E-02	1.0086E-02
8225	28.67	104.45	-1.0334E-03	-1.0019E-02	1.0073E-02
8226	30.72	104.45	-1.0278E-03	-9.8809E-03	9.9342E-03
8227	32.77	104.45	-9.7197E-04	-9.7050E-03	9.7535E-03
8228	34.82	104.45	-8.9282E-04	-9.5213E-03	9.5631E-03
8229	36.86	104.45	-8.8946E-04	-9.3230E-03	9.3653E-03
8230	38.91	104.45	-9.2673E-04	-9.1264E-03	9.1734E-03
8231	40.96	104.45	-9.3942E-04	-8.8941E-03	8.9436E-03
8232	43.01	104.45	-9.3691E-04	-8.5615E-03	8.6126E-03
8233	45.06	104.45	-8.7747E-04	-8.2035E-03	8.2502E-03
8234	47.10	104.45	-7.6308E-04	-7.9402E-03	7.9767E-03
16181	165.89	204.80	-4.5316E-03	1.6719E-03	4.8302E-03

Table B-3: Sample of output data converted to units of microns.

The imaging software used to capture the images from the SEM also records the length scale per pixel. In the case of the data shown, the conversion value is 0.64 microns per pixel. This allows the data to be presented in absolute length scales as given in Table B-3.

To determine the relative displacements, the position and displacement values of a selected node are subtracted from all nodal results. While any node would be a suitable candidate for the rescaling, the crack tip node is used. This aids the location of relative coordinates with respect to the crack tip and also makes visualization of crack behavior easier. The results after the relative coordinate and displacement transformation are shown in Table B-4.

node #	relative pos_x (microns)	relative pos_y (microns)	relative u_x (microns)	relative u_y (microns)
8222	-143.36	-100.35	3.6545E-03	-1.1550E-02
8223	-141.31	-100.35	3.6193E-03	-1.1614E-02
8224	-139.26	-100.35	3.5424E-03	-1.1710E-02
8225	-137.22	-100.35	3.4983E-03	-1.1691E-02
8226	-135.17	-100.35	3.5038E-03	-1.1553E-02
8227	-133.12	-100.35	3.5596E-03	-1.1377E-02
8228	-131.07	-100.35	3.6388E-03	-1.1193E-02
8229	-129.02	-100.35	3.6422E-03	-1.0995E-02
8230	-126.98	-100.35	3.6049E-03	-1.0798E-02
8231	-124.93	-100.35	3.5922E-03	-1.0566E-02
8232	-122.88	-100.35	3.5947E-03	-1.0233E-02
8233	-120.83	-100.35	3.6541E-03	-9.8754E-03
8234	-118.78	-100.35	3.7685E-03	-9.6121E-03
16181	0.00	0.00	0.0000E+00	0.0000E+00

Table B-4: *Sample of output data relative to the crack tip.*

REFERENCES

- Babu MV, Kumar RK, Prabhakar O, Shankar NG** (1996), "Fracture Mechanics Approaches to Coating Strength Evaluation," *Engineering Fracture Mechanics*, Vol.55, No.2, pp.235-248.
- Barut A, Guven I, Madenci E** (2001), "Analysis of Singular Stress Fields at Junctions of Multiple Dissimilar Materials under Mechanical and Thermal Loading," *International Journal of Solids and Structures*, Vol.38, No.50-51, pp.9077-9109.
- Bernard O, Amiri G, Haut C, Feltz B, Huntz AM, Andrieux M** (2002), "Mechanical and Microstructural Characterization of Oxide Films Damage," *Materials Science and Engineering A*, Vol.335, No.1-2, pp.32-42.
- Blanchard JP, Ghoniem NH** (1989), "Relaxation of Thermal Stress Singularities in Bonded Viscoelastic Quarter Planes," *ASME Journal of Applied Mechanics*, vol.56 (Dec), p.756.
- Bogy DB** (1968), "Edge-Bonded Dissimilar Orthogonal Elastic Wedges under Normal and Shear Loading," *ASME Journal of Applied Mechanics*, Vol. 35, pp.460-473.
- Bourne JP, Atkinson C** (1990A), "Stress Singularities in Viscoelastic Media –2. Plane-Strain Stress Singularities at Corners," *IMA Journal of Applied Mathematics*, vol.44, p.163.
- Bourne JP, Atkinson C** (1990B), "Stress Singularities in Angular Sectors of Viscoelastic Media," *International Journal of Engineering Science*, vol.28, no.7, p.615.
- Cao HC, Evans AG** (1989), "An Experimental Study of the Fracture Resistance of Bimaterial Interfaces," *Mechanics of Materials*, vol.7, no.4, pp.295-304.
- Charalambides PG, Lund J, Evans AG, McMeeking RM** (1989), "Development of a Test Method for Measuring the Mixed Mode Fracture Resistance of Bimaterial Interfaces," *Journal of Applied Mechanics*, vol.56, pp.77-82.
- Charalambides PG, Cao HC, Lund J, Evans AG** (1990), "Development of a Test Method for Measuring the Mixed Mode Fracture Resistance of Bimaterial Interfaces," *Mechanics of Materials*, vol.8, no.4, pp.269-283.
- Hein VL, Erdogan F** (1971), "Stress Singularities in a Two-Dimensional Wedge," *International Journal of Fracture*, Vol.7, pp.317-330.
- Hornet P, Eripret C** (1995), "Experimental J Evaluation from Load-Displacement Curve for Homogeneous and Overmatched SENB or CCT Specimens," *Fatigue and Fracture of Engineering Materials and Structures*, Vol.18, No.6, pp.679-692.

Howard SJ, Clyne TW (1991), "Interfacial Fracture Toughness of Vacuum-Plasma-Sprayed Coatings," *Surface and Coatings Technology*, Vol.45, pp.333-342.

Howard SJ, Phillipps AJ, Clyne TW (1993), "The Interpretation of Data from the Four-Point Bend Delamination Test to Measure Interfacial Fracture Toughness," *Composites*, Vol.24, No.2, pp.103-112.

Hutchinson JW, Suo Z (1991), "Mixed Mode Cracking in Layered Materials," *Advances in Applied Mechanics*, vol.29, p.63.

Irwin GR, de Wit R (1983), "A Summary of Fracture Mechanics Concepts," *Journal of Testing and Evaluation*, vol.11, No.1, pp.56-65.

Katipelli LR, Agarwal A, Dahotre NB (2000), "Singular Stresses in a Finite Region of Two Dissimilar Viscoelastic Materials with Traction-Free Edges," *Materials Science and Engineering A*, Vol.289, No.1-2, pp.34-40.

Kay N, Barut A, Madenci E (2002), "Singular Stresses in a Finite Region of Two Dissimilar Viscoelastic Materials with Traction-Free Edges," *Computer Methods in Applied Mechanics and Engineering*, Vol.191, pp.1221-1244.

Klingbeil NW, Beuth JL (1997), "Interfacial Fracture Testing of Deposited Metal Layers under Four-Point Bending," *Engineering Fracture Mechanics*, Vol.56, No.1, pp.113-126.

Lee SS (1997), "Free-edge stress singularity in a two-dimensional unidirectional viscoelastic laminate model," *ASME Journal of applied Mechanics*, Vol.64, pp.408-414.

Lee SS (1998), "Boundary Element Analysis of the Stress Singularity at the Interface Corner of Viscoelastic Adhesive Layers," *International Journal of Solids and Structures*, vol.35, no.13, p.1385.

Luo PF, Huang FC (2000), "Application of Stereo Vision to the Study of Mixed-Mode Crack-Tip Deformations," *Optics and Lasers in Engineering*, Vol.33, pp.349-368.

Mahajan R, Raiser G, Chandran B, Frutschy K, Mello M, Garner L (1999), "Modeling Reliability Failures: Status and Challenges," *Topical Research Conference on Reliability by SRC and SEMATECH*, University of Texas, Austin, November 1-3.

Malyshev BM, Salganik RL (1965), "The Strength of Adhesive Joints Using the Theory of Cracks," *International Journal of Fracture Mechanics*, vol.1, no.2, p.114.

Martin RH, Davidson BD (1999), "Mode II Fracture Toughness Evaluation using Four-Point Bend, End Notched Flexure Test," *Plastics Rubber and Composites Processing and Applications*, vol.28, no.8, pp.401-406.

Munz D, Yang YY (1992), "Stress Singularities at the Interface in Bonded Dissimilar Materials under Mechanical and Thermal Loading," *ASME Journal of Applied Mechanics*, Vol.35, pp.460-473.

Munz D, Yang YY (1993), "Stress Near the Edge of Bonded Dissimilar Materials Described by Two Stress Intensity Factors," *International Journal of Fracture*, Vol.60, pp.169-177.

Munz D, Fett T, Yang YY (1993), "The Regular Stress Term in Bonded Dissimilar Materials after a Change in Temperature," *Engineering Fracture Mechanics*, Vol.44, pp.185-194.

Rae PJ, Goldrein HT, Bourne NK, Proud WG, Forde LC, Liljekvist M (1999), "Measurement of Dynamic Large-Strain Deformation Maps using an Automated Fine Grid Technique," *Optics and Lasers in Engineering*, Vol.31, pp.113-122.

Rice JR (1968), "A Path Independent Integral and the Approximate Analysis of Strain Concentration by Notches and Cracks," *Journal of Applied Mechanics*, vol.35, No.2 (Jun), pp.379-386.

Rice JR (1988), "Elastic Fracture Mechanics Concepts for Interfacial Cracks," *Journal of Applied Mechanics*, vol.55 (Mar), p.98.

Read DT, Dally JW (1996), "Theory of Electron Beam Moiré," *Journal of Research of the National Institute of Standards and Technology*, Vol.101, No.1, pp.47-61.

Schapery RA (1961), "Approximate methods of transform inversion for viscoelastic stress analysis," In *Proceedings of the 4th U.S. National Congress of Applied Mechanics*, Vol.2, ASME, New York, pp.1075-1085.

Schapery RA (1965), "A Method of Viscoelastic Stress Analysis Using Elastic Solutions," *Journal of the Franklin Institute – Engineering and Applied Mathematics*, vol.279, no.4 (Apr), p.268.

Shih CF, Asaro RJ (1990), "Elastic-Plastic and Asymptotic Fields of Interface Cracks," *International Journal of Fracture*, Vol.42, pp.101-116.

Sun Z, Lyons JS, McNeill SR (1997), "Measuring Microscopic Deformations with Digital Image Correlation," *Optics and Lasers in Engineering*, Vol.27, pp.409-428.

Takeda N, Kiriya M (1999), "Matrix Crack Evolution in SiC Fiber/Glass Matrix Cross-Ply Laminates," *Composites: Part A*, Vol.30, pp.593-597.

ter Haar D (1951), "An Easy Approximate Method of Determination of the Relaxation Spectrum of a Viscoelastic Material," *Journal of Polymer Science*, vol.6, p.247.

Theocaris PS (1990), "The Elastic Field Around the Crack Tip Measured by Scanning Electromicroscopy," *Engineering Fracture Mechanics*, Vol. 37, pp. 739-751.

Theocaris PS, Stassinakis CA, Kytopoulos V (1988), "Stress Intensity Factors and CODs Defined by In-Plane Displacements Measured by Scanning Electron Microscopy," *Journal of Material Science*, Vol.23, pp.3992-3996.

Voevodin AA, Iarve EV, Ragland W, Zabinski JS, Donaldson S (2001), "Stress Analysis and In-Situ Failure Observation of Wear Protective Multilayer Coatings in Contact Loading," *Surface and Coatings Technology*, Vol.148, pp.38-45.

Vogel D, Grosser V, Schubert A, Michel B (2001), "MicroDAC Strain Measurements for Electronics Packaging Structures," *Optics and Lasers in Engineering*, Vol.36, pp.195-211.

Wiklund U, Bromark M, Larsson M, Hedenqvist P, Hogmark S (1997), "Cracking Resistance of Thin Hard Coatings Estimated by Four-Point Bending," *Surface and Coatings Technology*, Vol.91, No.1, pp.57-63.

Williams ML (1952), "Stress Singularities Resulting from Various Boundary Conditions in Angular Corners of Plates in Extension," *ASME Journal of Applied Mechanics*, vol.19, p.526.

Yan X, Agarwal RK (1998), "Two Test Specimens for Determining the Interfacial Fracture Toughness in Flip-Chip Assemblies," *ASME Journal of Electronic Packaging*, vol.120, No.2, pp.150-155.

Zhang N, Joseph PF, Kaya AC (1996), "A Finite Element Method for Separable HRR Solutions in Bi-Material Systems," *Proceedings of the ASME*, Vol. AD- 51/MD-73, pp. 3-21.